Collective and Microscopic Theories for Complex Deformed Nuclei

Michael Strecker

February 28, 2013

Dedicated to my father Helmut Strecker

Preface

First of all I would like to thank Prof. Horst Lenske for his readiness to be the supervisor of my doctoral thesis. He gave an overall guidance to the project and inspiration.

My special thank goes to Assoc. Prof. Nikolay Minkov with whom I was able to make endless discussions about all details of the work during his research visits in Giessen and my visits to Sofia.

Thirdly I would like to thank my parents for all their support.

Also I would like to thank the HGS-HIRe school for accepting me as a graduate student member and for arranging a HIC for FAIR scholarship.

Finally, I thank the institute co-workers for discussions and the secretaries for caring for administrative tasks.

Giessen, February 2013

Michael Strecker

Contents

1. Introduction

1.1. General introduction to nuclear structure physics

The working field of nuclear spectra delivers an important possibility to study the nuclear forces. As in every working field of physics one tries to obtain a unified theory which describes the origin and occurrence of experimental facts. Starting from fundamental nuclear forces such a theory should be able to describe the structure of nuclei, their conversion from one nuclide to another as well as all properties of the ground state and excited states.

Such a theory does not exist [1], because the complex system of the atomic nucleus is mainly governed by three types of interaction between the nucleons, namely the strong, electromagnetic and weak force. Even a simplification to only the strong force leads to the problem that the properties of this force are not known with enough detail and there are different approaches to describe the force between two nucleons. Additionally three- or many-body forces lead to further complications.

Therefore a typical nucleus with $A \lesssim 300$ represents a complex many-body problem. As known from classical mechanics [1], even the gravitational three-body problem cannot be solved exactly. The problem is also not comparable to the many-body problem of atomic physics because there is no charged center which allows one to neglect the interactions as in case of the electrons.

These difficulties lead to consequences for the nuclear research. The first one is that one must not confine oneself to only the nucleon-nucleon interactions which can be studied in scattering experiments with free nucleons. One has to describe the nucleus with specialized models which are suitable for nuclear decays or nuclear reactions. This work is only treating the so-called *nuclear structure models*.

One of the earliest nuclear structure models was the liquid drop model which assumes a strong interaction of all the nucleons and still plays an important role in the description of binding energies of nuclei.

Later approaches considered the findings of quantum mechanics and enriched the purely phenomenological models until a new step forward to a purely quantum mechanical description was made. Since the nucleon velocity inside the nucleus is not coming close

to the light speed, relativistic effects can be neglected. With a strong interaction V_{ij} between the nucleons i and j, the stationary states of the nucleus are described by a wave function $\Psi_n(1,\ldots,A)$, which is a solution of the Schrödinger equation [1]:

$$\left(\sum_{i=1}^{A} T_i + \sum_{i<j=1}^{A} V_{ij}\right) \Psi_n(1,\ldots,A) = E_n \Psi_n(1,\ldots,A)\,. \tag{1.1}$$

One of the first and very successful solutions of (1.1) was the single-particle shell model. In such a model it is assumed that the nucleons move in an average potential created by all the nucleons while residual interactions are neglected.

One important step was the inclusion of a spin-orbit interaction, analoguous to atomic physics. This idea was first published by Goeppert-Mayer, Jensen, Haxel and Suess in 1949 [2, 3] and allowed the explanation of the magic numbers as well as spins and parities of the ground states and a few excited states. This model could also be extended to the case of deformed nuclei. The used single-particle potentials are phenomenologically motivated, for example the well-known case of a Woods-Saxon potential. The parameters of such phenomenological potentials are then determined by adjustment to spectroscopic data.

Another type of models could be called hydrodynamical, because they treat the dynamic of a liquid drop. This can happen in two different ways. The drop can either expand and contract in a rhythmic way, leading to density fluctuations. This is the so-called "breathing mode".

In a first approximation the nuclear fluid is very incompressible [1]. Therefore the excitation energy for such types of oscillations should be very high. But it could also happen that the surface performs various kinds of oscillations while the volume stays constant. These deformations of the nuclear surface are then typically described by an expansion of the nuclear surface into spherical harmonics.

Such *geometrical collective models* are very successful in the description of excitation spectra in the energy region up to 2 MeV which show characteristic band structures. The first use of such models was proposed by Bohr and Mottelson in 1952 [4, 5, 6] and they were further developed and worked out by Faessler and Greiner [7, 8, 9, 10, 11, 12, 13]. Aage Bohr, Ben Mottelson and James Rainwater got the Nobel prize for their work on collective models in 1975.

The inner structure with the individual nucleons is neglected and replaced by the picture of a homogeneous and liquid-like nuclear matter. It is quite evident that the liquid drop model is only applicable in those cases where the size of the nucleon is very small compared to the total nuclear size. This restricts the model to heavier nuclei.

Another more microscopic approach to collective excitations is the method of *Random*

Phase Approximation (RPA) which goes beyond static independent particle models. The name originates from an approximation made in one of the original derivations, for example in [14] from 1964. Based on the shell model (or Hartree-Fock or Hartree-Fock-Bogolyubov model), a series of excited states can be very adequately described as particle-hole excitations [15]. The pure shell model fails to explain the high energy of the giant dipole resonance of ^{16}O for example.

The treatment is usually limited to 1 particle-1 hole excitations only which is indeed a good approximation for a certain kind of states. The picture of surface vibrations used in the collective models can be brought in connection to RPA solutions by means of certain sum rules.

More detailed introductions to the different model approaches will be given at the beginning of the corresponding chapters.

1.2. The topics of this thesis

The main purpose of this thesis is to describe energy levels and transition probabilities of complex deformed nuclei. We follow two different approaches, namely a collective quadrupole-octupole model and a microscopic random phase approximation based on phenomenological single-particle calculations.

The work in the collective model is a continuation of the fundamental paper by N. Minkov et al. [16] in which the model was first published. This work is extended in two directions.

Firstly, there is a purely analytical approach to the model which was developed further in several papers, especially in [17]. The description of energy levels is extended to non-yrast band sequences and transitions between them.

Secondly, the model is solved numerically in the most general case when all model parameters are allowed to vary freely. The analytical solution fails to describe this case and one has to impose certain restrictions, which lead to the case of equal oscillation frequencies, $\omega_2 = \omega_3$, the so-called case of *coherent interplay*.

The nuclei under consideration are mostly rare earths and actinides. These collective model calculations are of interest and such research is up to date. For example, Bizzeti and Bizzeti-Sona [18, 19] have done similar quadrupole-octupole calculations for energy levels and transitions of the nuclei ^{150}Nd, ^{152}Sm, ^{154}Gd and ^{156}Dy in 2010.

Exactly the same nuclei (and others) are also under consideration in this work. The similarity to this thesis goes even further because Bizzeti and Bizzeti-Sona solved the same problem – the numerical solution of their model Hamiltonian.

The realization of the calculations is different however. While in their case they use the finite differences method in combination with the Arnoldi-Lanczos method for diagonalization, we calculate matrix elements to obtain the eigensolutions.

Besides this, there is ongoing research in the area of *non-axial* deformations. As one can show, axial deformations usually minimize the energy. Therefore one would intuitively assume that deformed nuclei prefer to be in axial deformations, since it is a general principle of nature that a system goes in the direction where the energy is minimized.

However, S. Frauendorf has shown in calculations for ^{220}Ra [20] that the spin-parity sequence of the rotational ground band for this nucleus can be explained by assuming a rotating heart-shaped nucleus.

An even larger interest nowadays is spent to nuclei with a tetrahedral shape. This analysis is carried forward in the TetraNuc project with more than 100 collaborators. As a side project of this thesis I contributed to this project, but since this work was mainly a programming task and has not yet led to new results, it is omitted.

Furthermore, a study of the connection between collective shape characteristics and the intrinsic reflection-asymmetric shell structure of the nucleus is carried out. Concerning this topic I contributed to the papers [21, 22, 23, 24, 25] in which we examine the effect of parity-mixing in the single-particle states of odd-mass nuclei as well as the Coriolis decoupling factor as a function of the deformation.

Last but not least, deformed RPA calculations were carried out. As starting point for these calculations we again use the single-particle program from Cwiok et al. [26]. The matrix elements for the multipole operators have been worked out analytically and were found to be simple Kronecker-Delta expressions, which are very fastly evaluated by the computer.

Quite similar calculations were done by Yoshida [27] in 2007. In that work however the consideration was limited to the axial quadrupole deformation only, while in the present work the code is able to treat also axial octupole deformations.

2. Quadrupole-Octupole Model

2.1. Some general remarks about collective models

One can think of a nucleus as a compound of individual nucleons, protons and neutrons, each having a position, spin and isospin coordinates as degrees of freedom. This seems to be a very natural choice for the degrees of freedom. This leads to a many-particle Schrödinger equation with a huge number of degrees of freedom, increasing tremendously for heavier nuclei.

But sometimes we are more interested in the behaviour of the system as a whole, similar as one also treats a proton as a particle although it is a composed system of quarks and gluons. These models are called *collective models*. The starting point for them is always an expansion of the nuclear surface into spherical harmonics by means of [15, 28, 29]

$$R(\theta, \phi, t) = R_0 \left(1 + \sum_{\lambda\mu} \alpha_{\lambda\mu}(t)^* Y_{\lambda\mu}(\theta, \phi) \right) . \tag{2.1}$$

As mentioned in the general introduction, the high incompressibility of nuclear matter suppresses compressional excitations of volume character. The low energy modes are therefore surface excitations or rotations of the nucleus as a whole.

Equation (2.1) is a quite natural approach if one thinks of the nucleus being made of some liquid which behaves similar like a drop of water. A. Lauterwasser [30] has investigated the many different oscillation patterns appearing when a drop of water is exposed to sound of a given constant frequency. Ideally such experiments should take place in a zero gravity environment. At certain frequencies – the eigenfrequencies of the drop – characteristic patterns can be seen, similar to the Chladni sound patterns made of sand on plates [31].

This formula has indeed also other important applications besides from nuclear physics. For example one can use it for the problem of pattern recognition, e.g. the recognition of human faces in a crowd or at entrances. If a face is projected onto a sphere in a standardized way, the expansion coefficients carry information about the structure of the face [32].

The collective coordinates introduced by (2.1) are the laboratory coefficients. To be

more precise they are related to the intrinsic coordinates $a_{\lambda\mu}$ in the body-fixed frame of reference by means of a Wigner-function,

$$a_{\lambda\mu} = \sum_{\nu} D^{\lambda}_{\nu\mu}(\Omega)\alpha_{\lambda\nu}\,, \tag{2.2}$$

where $\Omega = \Omega(\vartheta_1, \vartheta_2, \vartheta_3)$ is a short notation for the three Euler angles. The spherical harmonics transform in the same way. Since $\lambda = 0$ leads to spherical compressional modes and $\lambda = 1$ corresponds to a center of mass movement, $\lambda = 2$ is the lowest order of interest. It is advantageous (and usually done) to use an intrinsic coordinate system whose axis coincides with the symmetry axis of the nucleus. This leads to the fact that we can choose

$$a_{2,-1} = a_{2,1} = 0 \qquad \text{and} \qquad a_{2,-2} = a_{2,2}\,. \tag{2.3}$$

In the present work we most often consider pear-like shaped nuclei as seen in Figure 2.1. The relevant degrees of freedom are then the axial quadrupole ($\beta_2 = a_{20}$) and octupole ($\beta_3 = a_{30}$) deformation parameters.

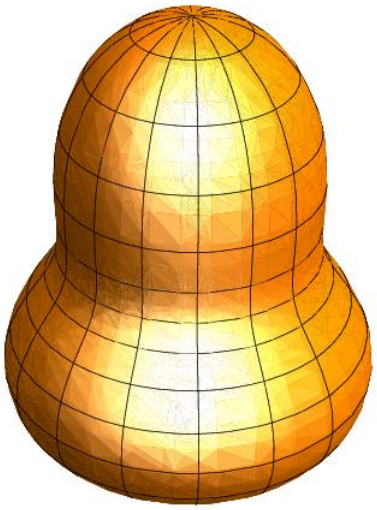

Figure 2.1.: Pear-shaped nucleus with quadrupole and octupole deformation.

2.2. The model Hamiltonian

2.2.1. The vibrational part

Classically the natural ansatz for the total vibrational energy in the body fixed frame is

$$T_{\text{vib}} + V_{\text{vib}} = \sum_{\nu=2}^{3} \left(\frac{1}{2} B_\nu \dot{\beta}_\nu(t)^2 + \frac{1}{2} C_\nu \beta_\nu(t)^2 \right) \tag{2.4}$$

with mass parameters B_ν and stiffness parameters C_ν. The term for the kinetic energy can be compared to the expression $p^2/2m$, where we have to replace the classical linear momentum by its quantum mechanical analogon,

$$p_\nu \longrightarrow \hat{p}_\nu = \frac{\hbar}{i}\frac{\partial}{\partial\beta_\nu}\,. \tag{2.5}$$

Adding together the quadrupole and octupole terms, we immediately obtain the vibrational Hamiltonian of the model,

$$\hat{H}_{\text{vib}} = -\frac{\hbar^2}{2B_2}\frac{\partial^2}{\partial\beta_2^2} - \frac{\hbar^2}{2B_3}\frac{\partial^2}{\partial\beta_3^2} + \frac{1}{2}C_2\beta_2^2 + \frac{1}{2}C_3\beta_3^2\,. \tag{2.6}$$

However, this is not a thorough derivation of the Hamiltonian, but only some argumentation to make it plausible. If one works on a deeper level, one can also obtain (2.6) as a certain approximation after applying the Pauli-Podolsky quantization procedure. An example of applying the Pauli prescription and calculating the Laplace operator in curvilinear coordinates can be found in [33].

2.2.2. The rotational part

The rotational part is somewhat more difficult to derive. Repeating the argumentation from [34], we start from the definition of the angular momentum operator $\hat{\vec{M}}'(\vartheta_j)$ of the nucleus along the intrinsic axes. The components are [29]

$$\hat{M}'_k(\vartheta_j) = \hbar\hat{L}'_k(\vartheta_j) \qquad k = 1,2,3\,, \tag{2.7}$$

with Euler angles ϑ_j connecting the intrinsic and the laboratory system. Explicitly written out we have

$$\hat{L}'_1 = -i\left(-\frac{\cos\vartheta_3}{\sin\vartheta_2}\frac{\partial}{\partial\vartheta_1} + \sin\vartheta_3\frac{\partial}{\partial\vartheta_2} + \cot\vartheta_2\cos\vartheta_3\frac{\partial}{\partial\vartheta_3}\right) \tag{2.8}$$

$$\hat{L}'_2 = -i\left(\frac{\sin\vartheta_3}{\sin\vartheta_2}\frac{\partial}{\partial\vartheta_1} + \cos\vartheta_3\frac{\partial}{\partial\vartheta_2} - \cot\vartheta_2\sin\vartheta_3\frac{\partial}{\partial\vartheta_3}\right) \tag{2.9}$$

$$\hat{L}'_3 = -i\left(\frac{\partial}{\partial\vartheta_3}\right) \tag{2.10}$$

The Hamiltonian includes the square of the angular momentum operator, given by

$$\begin{aligned}\hat{\vec{L}}^2 &= \hat{L}_1^2 + \hat{L}_2^2 + \hat{L}_3^2 = \hat{L}_1'^2 + \hat{L}_2'^2 + \hat{L}_3'^2 \\ &= \left(-\frac{\partial^2}{\partial\vartheta_2^2} - \cot\vartheta_2\frac{\partial}{\partial\vartheta_2} - \frac{1}{\sin^2\vartheta_2}\left(\frac{\partial^2}{\partial\vartheta_1^2} + \frac{\partial^2}{\partial\vartheta_3^2}\right) + 2\frac{\cos\vartheta_2}{\sin^2\vartheta_2}\frac{\partial^2}{\partial\vartheta_1\partial\vartheta_3}\right)\,.\end{aligned} \tag{2.11}$$

Classically the rotational kinetic energy of a rigid body is given by

$$T = \sum_{k=1}^{3} \frac{1}{2} \mathcal{J}_k \omega_k^2 \,. \tag{2.12}$$

This formula assumes that the origin of the coordinate system coincides with the center of mass. The angular velocities ω_k are relative to the x'-, y'- and z'-axis of the body-fixed coordinate system. Using

$$M'_k = \mathcal{J}_k \omega_k \,, \tag{2.13}$$

we arrive at

$$T = \sum_k \frac{M'^2_k}{2\mathcal{J}_k} \,. \tag{2.14}$$

In the special case of a *symmetric rigid rotator*, charakterized by $\mathcal{J}_1 = \mathcal{J}_2 \equiv \mathcal{J}_0$, the kinetic energy reads

$$T = \frac{M'^2_1 + M'^2_2}{2\mathcal{J}_0} + \frac{M'^2_3}{2\mathcal{J}_3} = \frac{\vec{M}^2 - M'^2_3}{2\mathcal{J}_0} + \frac{M'^2_3}{2\mathcal{J}_3} \,. \tag{2.15}$$

In the axial quadrupole-octupole case, which we want to consider, the last term has no contribution. The deformations $\beta_2 = a_{20}$ and $\beta_3 = a_{30}$ lead to spherical harmonics Y_{lm} with $m = 0$ which do *not* depend on the azimuthal angle. Therefore the rotational part of the Hamiltonian reads

$$\hat{H}_{\mathrm{rot}} = \frac{\hat{\vec{M}}^2 - \hat{M}'^2_3}{2\mathcal{J}_0} \,. \tag{2.16}$$

In case of odd-A nuclei, we have to add together the angular momentum of the core $\hat{\vec{M}}$ and that of the outer particle $\hat{\vec{j}}$ which is thought to orbit around the deformed core, see Figure 2.2. Thus we have

$$\hat{\vec{I}}\hbar = \hat{\vec{M}} + \hat{\vec{j}}\hbar \,, \tag{2.17}$$

keeping in mind that $\hbar$ is already included in the definition of $\hat{\vec{M}}$. Replacing $\hat{\vec{M}}$ in (2.16) by

$$\hat{\vec{M}} = \hat{\vec{I}}\hbar - \hat{\vec{j}}\hbar \,, \tag{2.18}$$

one gets to

$$\hat{H}_{\mathrm{rot}} = \frac{\hbar^2}{2\mathcal{J}_0} \left[(\vec{I} - \vec{j})^2 - (I_3 - j_3)^2 \right] \,. \tag{2.19}$$

Since it is clear that we work with operators and that the Hamiltonian is written for intrinsic coordinates, the primes can be left away as well as the operator hats. Making use of

$$2\vec{I} \cdot \vec{j} = I_+ j_- + I_- j_+ + 2 I_3 j_3 \tag{2.20}$$

with the definitions

$$I_\pm = I_1 \pm i I_2 \tag{2.21}$$

$$j_\pm = j_1 \pm i j_2 \tag{2.22}$$

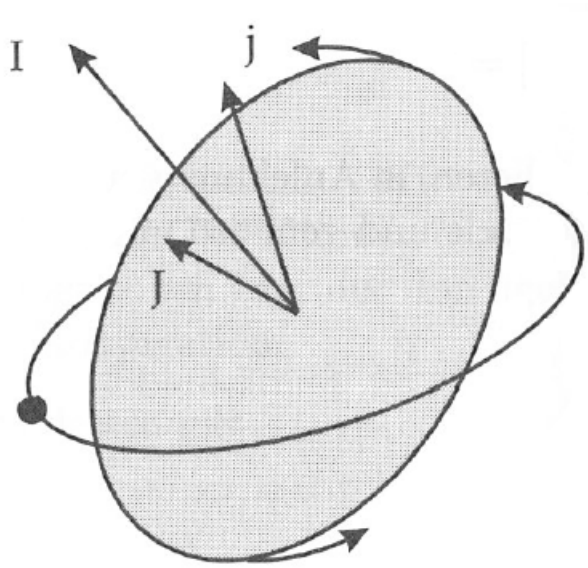

Figure 2.2.: Schematic illustration of the core-plus-particle model. The angular momentum of the core (denoted here by J) is coupled with the odd particle angular momentum j to the to the resulting total angular momentum I. Figure taken from [37].

we can write out the bracket term in (2.19) as

$$\begin{aligned}(\vec{I}-\vec{j})^2-(I_3-j_3)^2 &= (\vec{I}^2-2\vec{I}\cdot\vec{j}+\vec{j}^2)-(I_3^2-2I_3j_3+j_3^2)\\ &= \vec{I}^2-(I_+j_-+I_-j_+ +2I_3j_3)+\vec{j}^2-I_3^2+2I_3j_3-j_3^2 \\ &= \vec{I}^2-I_3^2-j_3^2-(I_+j_-+I_-j_+)+\vec{j}^2\,.\end{aligned} \tag{2.23}$$

The term $(I_+j_-+I_-j_+)$ classically corresponds to the Coriolis and centrifugal forces. The $\vec{j}^2$-term is often neglected in the derivation of the rotational Hamiltonian, see [29] and [35] for example. Writing out $\vec{j}^2$ in components, the collective energy for rotation of an axially symmetric nucleus around a perpendicular axis, the z-axis being the symmetry axis, is given by

$$\hat{H}_{\mathrm{rot}}=\frac{\hbar^2}{2\mathcal{J}_0}\left[\vec{I}^2-I_3^2+(j_1^2+j_2^2)-(I_+j_-+I_-j_+)\right]. \tag{2.24}$$

The same expression can be found in [36].

In the following we consider a strong coupling limit (see Figure 2.3). This limit is also called the adiabatic approximation and assumes that the influence of the rotational motion on the intrinsic structure of the nucleus can be neglected.

The projection of the total angular momentum on the nuclear symmetry axis is a preserved quantum number, which is given by K (see Figure 2.3). With no collective

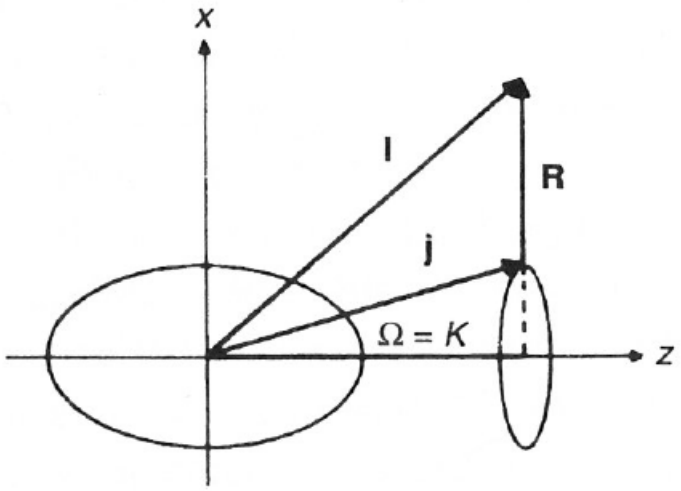

Figure 2.3.: Schematic illustration of the strong coupling limit, also called deformation alignment. Figure taken from [36].

component along this axis, we have $\Omega = K$ in the strong coupling limit. As $I \geq K$, the spins

$$I = K, K+1, K+2, \ldots \tag{2.25}$$

are observed.

The single-particle wave functions are obtained from the deformed shell model. The only exact quantum number is the projection Ω of the angular momentum $\vec{j}$ on the symmetry axis. If one introduces a counting index κ for the states with the same Ω, then the states obey

$$\hat{H}_{\mathrm{sp}} \chi_{\kappa\Omega} = \epsilon_{\kappa\Omega} \chi_{\kappa\Omega} \,. \tag{2.26}$$

The exact definition of $\hat{H}_{\mathrm{sp}}$ is given further down.

Then we can write the result for the energies with respect to eigenvalues as

$$E_{IK} = \epsilon_{\kappa K} + \frac{\hbar^2}{2\mathcal{J}_0} \left[I(I+1) - K^2 + \delta_{K,\frac{1}{2}} a (-1)^{I+\frac{1}{2}} \left(I + \frac{1}{2} \right) \right] . \tag{2.27}$$

This expression is based on the structure of the strong-coupling wave functions. More details can be found for example in [36].

The moment of inertia can be calculated explicitly by matrix elements. In [38] it is shown that for the quadrupole-octupole case we have

$$\mathcal{J}_0 = 3B_2\beta_2^2 + 6B_3\beta_3^2 \,. \tag{2.28}$$

However, we prefer to only use the functional form. The ansatz then reads

$$\mathcal{J}_0 = d_2\beta_2^2 + d_3\beta_3^2 \tag{2.29}$$

with moment of inertia parameters d_2 and d_3 which describe the strength of the quadrupole and octupole contributions to the total moment of inertia.

These results clearly motivate the following choice for the rotational Hamiltonian in the quadrupole-octupole model:

$$\hat{H}_{\text{rot}} = \frac{X}{d_2\beta_2^2 + d_3\beta_3^2}\,, \tag{2.30}$$

with X as a function of angular momentum,

$$X(I) = \frac{1}{2}\left[d_0 + I(I+1)\right]\,, \tag{2.31}$$

in the *even-even* case, where d_0 is a fitting parameter which determines the shape of the potential in the ground state. For *odd-mass* nuclei the above expression is generalized to

$$X(I,K,\pi a) = \frac{1}{2}\left[d_0 + I(I+1) - K^2 + \pi a \delta_{K,\frac{1}{2}}(-)^{I+1/2}\left(I+\frac{1}{2}\right)\right]\,, \tag{2.32}$$

where a is the so-called decoupling parameter. a can in principle be calculated from the single-particle wave function χ_K (for the exact definition see the chapter about the single-particle program) in the case of $K = 1/2$. K is the third projection of the ground state angular momentum and the parity π is defined as the product

$$\pi = \pi_\varphi \cdot \pi_\chi \tag{2.33}$$

of the parity of the even-even core oscillation function (defined below) and π_χ, the parity of the unpaired particle function.

2.2.3. Plots of the model potential

The potential

$$V(\beta_2,\beta_3) = \frac{1}{2}C_2\beta_2^2 + \frac{1}{2}C_3\beta_3^2 + \frac{X(I)}{d_2\beta_2^2 + d_3\beta_3^2} \tag{2.34}$$

is plotted in Figures 2.4 and 2.5. As one can see the shape is similar to the Mexican hat potential well known from chiral symmetry and the Higgs mechanism, see for example chapter 11 in [39]. A major difference however is that there is a singularity at the origin, preventing the nucleus from becoming completely spherical. In addition, the bottom of the potential is an ellipse only in the case of *coherent interplay* (defined below by equation 2.39). In the most general case there are two minima lying symmetrically to each other.

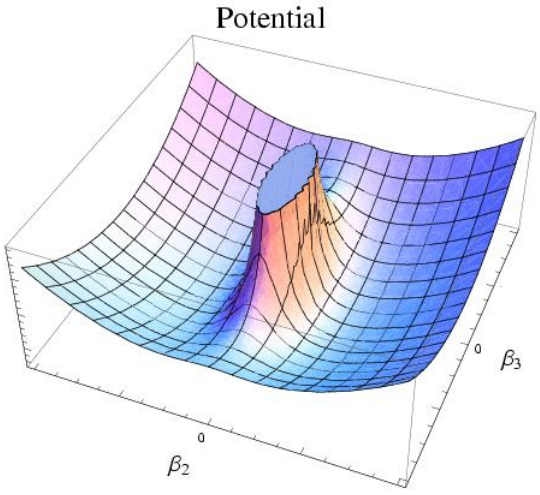

Figure 2.4.: Typical overall "Mexican hat" shape of the potential (2.34).

2.3. Analytical coherent solution

The collective Hamiltonian fully written out reads [16]

$$\hat{H} = -\frac{\hbar^2}{2B_2}\frac{\partial^2}{\partial\beta_2^2} - \frac{\hbar^2}{2B_3}\frac{\partial^2}{\partial\beta_3^2} + \frac{1}{2}C_2\beta_2^2 + \frac{1}{2}C_3\beta_3^2 + \frac{X}{d_2\beta_2^2 + d_3\beta_3^2}\,. \tag{2.35}$$

In a first step a coordinate transformation from the Cartesian β_2 and β_3 coordinates to ellipsoidal coordinates η (radial coordinate) and ϕ (angle coordinate), given by

$$\eta = \left[\frac{2(d_2\beta_2^2 + d_3\beta_3^2)}{d_2 + d_3}\right]^{\frac{1}{2}} \qquad \text{and} \qquad \phi = \arctan\left(\frac{\beta_3}{\beta_2}\sqrt{\frac{d_3}{d_2}}\right)\,, \tag{2.36}$$

is performed. The inverse transformation is worked out to be

$$\beta_2 = p\eta\cos\phi, \qquad \beta_3 = q\eta\sin\phi\,, \tag{2.37}$$

with

$$p = \sqrt{\frac{d}{d_2}}, \qquad q = \sqrt{\frac{d}{d_3}} \qquad \text{and} \qquad d = \frac{1}{2}(d_2 + d_3)\,. \tag{2.38}$$

It turned out that in order to obtain an analytical solution one can assume that the oscillation frequencies are the same,

$$\omega \equiv \omega_2 = \sqrt{\frac{C_2}{B_2}} \stackrel{!}{=} \omega_3 = \sqrt{\frac{C_3}{B_3}} \equiv \sqrt{\frac{C}{B}}\,. \tag{2.39}$$

In case of this *coherent interplay* the Hamiltonian in ellipsoidal coordinates is obtained in the simple form

$$H_{\text{qo}} = -\frac{\hbar^2}{2B}\left[\frac{\partial^2}{\partial\eta^2} + \frac{1}{\eta}\frac{\partial}{\partial\eta} + \frac{1}{\eta^2}\frac{\partial^2}{\partial\phi^2}\right] + U_I(\eta)\,, \tag{2.40}$$

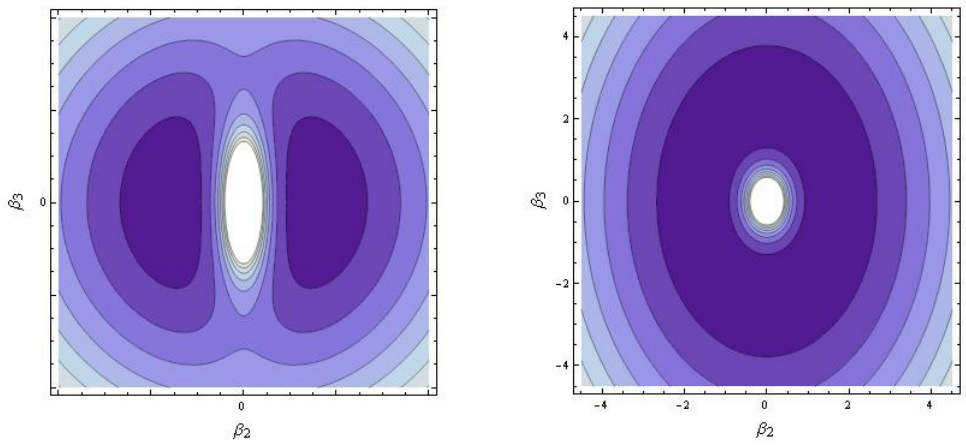

Figure 2.5.: Contour plots of the potential (2.34). As one can see there are either two minima or an ellipsoidal bottom of the potential in the special case of coherent interplay.

with

$$U_I(\eta) = \frac{1}{2}C\eta^2 + \frac{X(I)}{d\eta^2}\,. \tag{2.41}$$

A separation ansatz

$$\Phi(\eta,\phi) = \psi(\eta)\varphi(\phi) \tag{2.42}$$

leads to two independent differential equations for the Schrödinger equation of the Hamiltonian, the one belonging to the η coordinate being of the Davidson potential [73, 74] type

$$\frac{\partial^2}{\partial\eta^2}\psi(\eta) + \frac{1}{\eta}\frac{\partial}{\partial\eta}\psi(\eta) + \frac{2B}{\hbar^2}\left[E - \frac{\hbar^2}{2B}\frac{k^2}{\eta^2} - U_I(\eta)\right]\psi(\eta) = 0\,, \tag{2.43}$$

and a simple harmonic oscillator differential equation for $\varphi(\phi)$,

$$\frac{\partial^2}{\partial\phi^2}\varphi(\phi) + k^2\varphi(\phi) = 0\,. \tag{2.44}$$

The last equation is solved under the boundary condition

$$\varphi\left(-\frac{\pi}{2}\right) = \varphi\left(\frac{\pi}{2}\right) = 0\,, \tag{2.45}$$

which provides two different solutions with positive and negative parity, respectively:

$$\varphi^+(\phi) = \sqrt{\frac{2}{\pi}}\cos(k\phi), \qquad k = 1,3,5,\ldots\,, \tag{2.46}$$

$$\varphi^-(\phi) = \sqrt{\frac{2}{\pi}}\sin(k\phi), \qquad k = 2,4,6,\ldots\,. \tag{2.47}$$

The reader might notice the similarity to the solutions for the quantum mechanical problem of a particle in an infinitely deep box potential. The boundary condition is

equivalent to an infinitely high and infinitely thin wall (δ-function like) which separates the deformation plane in prolate ($\beta_2 > 0$) and oblate ($\beta_2 < 0$) shapes.

For the Davidson potential we can write down the eigenvalues as

$$E_{n,k}(I, K, \pi a) = \hbar\omega \left[2n + 1 + \sqrt{k^2 + bX(I, K, \pi a)}\right] , \tag{2.48}$$

where ω and $b = 2B/(\hbar^2 d)$ are taken as fitting parameters. n and k are quantum numbers. $n = 0, 1, 2, \ldots$ can be considered as main quantum number and generates $n + 1$ peaks of the wave function in radial direction. $k = 1, 2, 3, \ldots$ is the angular quantum number and generates k peaks in angular direction from $-\pi/2$ to $\pi/2$.

The respective eigenfunctions $\psi(\eta)$ are obtained in terms of generalized Laguerre polynomials

$$\psi_n^I(\eta) = \sqrt{\frac{2c\Gamma(n+1)}{\Gamma(n+2s+1)}} e^{-c\eta^2/2} (c\eta^2)^s L_n^{2s}(c\eta^2) , \tag{2.49}$$

where

$$c = \frac{\sqrt{BC}}{\hbar} \tag{2.50}$$

is another fitting parameter playing the role of an oscillator length $1/\sqrt{c}$. The quantity

$$s = \frac{1}{2}\sqrt{k^2 + bX(I, K, \pi a)} \tag{2.51}$$

corresponds to a generalized angular momentum variable. It was checked[1] that with the given normalizations the product (2.42) provides a complete set of orthonormal functions, if the integration is carried out over the right half-plane only (with the limits $0 \leq \eta < \infty$ and $-\pi/2 \leq \phi \leq \pi/2$).

2.4. Theory of transition operators

In the following sections about coherent and non-coherent model extensions the calculations include reduced B(E1), B(E2) and B(E3) transition probabilities. The basic theory about electromagnetic transitions can be found in [16].

Since the consideration is restricted to axial deformations only, the projection K of the collective angular momentum on the principal symmetry axis is taken as zero. Then the total wave function of the coherent quadrupole-octupole vibration and collective rotation of an even-even nucleus has the form

$$\Psi^{\pi}_{nkIM0}(\eta, \phi) = \sqrt{\frac{2I+1}{8\pi^2}} D^I_{M0}(\theta) \Phi^{\pi}_{nkI}(\eta, \phi) , \tag{2.52}$$

[1] I found that in [16] the normalization was given wrong by a misprint.

where

$$\Phi^{\pi}_{nkI}(\eta,\phi) = \psi^{I}_{nk}(\eta)\varphi^{\pi}_{k}(\phi) \tag{2.53}$$

is the quadrupole-octupole vibration part.

For a given model state $\Psi^{\pi}_{nkIM0}(\eta,\phi)$, a given multipolarity λ as well as initial quantum numbers $n = n_i$, $k = k_i$, $I = I_i$, and final quantum numbers $n = n_f$, $k = k_f$, $I = I_f$, we have

$$B(E\lambda; n_i k_i I_i \to n_f k_f I_f) = \frac{1}{2I_i+1} \sum_{M_i M_f \mu} \left| \left\langle \Psi^{\pi_f}_{n_f k_f I_f M_f 0}(\eta,\phi) | \mathcal{M}_{\mu}(E\lambda) | \Psi^{\pi_i}_{n_i k_i I_i M_i 0}(\eta,\phi) \right\rangle \right|^2 \tag{2.54}$$

The operators for the electric E1, E2 and E3 transitions are given in terms of the collective coordinates as [16]

$$\mathcal{M}_{\mu}(E\lambda) = \sqrt{\frac{2\lambda+1}{4\pi(4-3\delta_{\lambda,1})}} \hat{Q}_{\lambda 0} D^{\lambda}_{\mu 0}, \quad \lambda = 1,2,3, \quad \mu = 0, \pm 1, \ldots, \pm\lambda\,, \tag{2.55}$$

where

$$\hat{Q}_{10} = M_1 \beta_2 \beta_3 \qquad \hat{Q}_{\lambda 0} = M_\lambda \beta_\lambda, \qquad \lambda = 2,3\,. \tag{2.56}$$

For the $\hat{Q}$-operators we use first order expressions in β_2 and β_3 for the E2 and E3 case while for E1 we use the second order expression.

The M_λ factors are electric charge factors which we take as [61]

$$M_\lambda = \frac{3}{\sqrt{(2\lambda+1)\pi}} Z e R_0^{\lambda}, \qquad \lambda = 2,3\,, \tag{2.57}$$

where the nuclear radius $R_0 = r_0 A^{1/3}$ is determined by the reduced radius $r_0 \approx 1.2$ fm, Z is the proton number and e is the electric charge of the proton. The charge factor M_1 is taken according to the droplet model concept [62, 63, 64] in the form [66]

$$M_1 = \frac{9AZe^3}{56\sqrt{35}\pi} \left(\frac{1}{J} + \frac{15}{8QA^{\frac{1}{3}}} \right). \tag{2.58}$$

A reasonable choice for the quantities J and Q should lie in the regions [65, 66]

$$25 \le J \le 44 \text{ MeV} \qquad 17 \le Q \le 70 \text{ MeV}\,. \tag{2.59}$$

For practical calculations we choose fixed average values $J = 35$ MeV and $Q = 45$ MeV. We also replace the proton charge e by an effective charge e^1_{eff}, which can have a value different from one and which enters in the fitting procedure as an adjustable parameter.

3. Extension of the coherent case to non-yrast bands

The Coherent Quadrupole-Octupole Motion (CQOM) model is extended to non-yrast alternating-parity structures in addition to the yrast band. This study provides not only a test of the model in the higher energy parts of the spectra, but also gives an interpretation of a large number of data that may guide the experimental search for similar level structures in other nuclear regions. Since this work was published in [60] and [17], only the essentials are summarized here.

3.1. Construction of alternating parity spectra

In case of only axial deformations we take the projection K of the collective angular momentum on the symmetry axis as zero. For even-even nuclei the total wave function of the coherent quadrupole-octupole vibration and collective rotation is given by (2.52). For these functions different phase conventions exist which are summarized in Table 4.2 of reference [47]. In our case we use the phase convention of Bohr and Mottelson, see [28].

The $\mathcal{RP}$-symmetry has to be conserved. The $\mathcal{R}$-operator is defined as a rotation by an angle π about an axis perpendicular to the intrinsic z-axis, acting on the Wigner-function and giving a factor $(-1)^I$. The $\mathcal{P}$-operator is the parity operator, which acts on $\Phi^{\pi}_{nkI}(\eta,\phi)$, and simply gives a factor of $+1$ or -1.

Thus, the product of these two numbers, the so-called *simplex* quantum number $\pi \cdot (-1)^I = 1$, has to be conserved. This also leads to the fact that the total wave function (2.52) is a D_∞-invariant function.

The conservation of the simplex quantum number imposes a positive or negative parity depending on the angular momentum for the states (2.52), namely positive parity for even angular momentum and negative parity for odd angular momentum,

$$\Phi^{+}_{nkI} = \psi^{I}_{nk}(\eta)\varphi^{+}_{k}(\phi) \quad \text{for even } I \tag{3.1}$$

$$\Phi^{-}_{nkI} = \psi^{I}_{nk}(\eta)\varphi^{-}_{k}(\phi) \quad \text{for odd } I\,. \tag{3.2}$$

This has direct consequences for the possible choice of the k quantum number. $\varphi_k^\pi(\phi)$ has a positive parity for odd k numbers and negative parity for even k numbers. In [16] the yrast band is described with the lowest possible quantum numbers. Therefore the choice for the main quantum number is $n = 0$. The positive-parity ground state band and the lowest lying negative-parity band are described with the quantum numbers $k = k^{(+)} = 1$ (ground state band) and $k = k^{(-)} = 2$ (negative-parity band).

This scheme was extended to higher lying non-yrast bands by means of three postulates:

1. The sequences in each couple of level sequences are characterized by the same value of the quantum number $n = 0, 1, 2, \ldots$ and by different values of k, chosen as $k = k_n^{(+)}$ being odd for the even angular momentum sequence and $k = k_n^{(-)}$ being even for the odd angular momentum sequence. A couple of k-values does not necessarily have to consist of two neighbouring quantum numbers.

2. The lowest possible choices for the quantum number n correspond to the lowest alternating-parity bands: $n = 0$ for the yrast band, $n = 1$ for the next couple of non-yrast alternating parity bands and so on. The values of $k_n^{(+)}$ and $k_n^{(-)}$ are not restricted except from the parity condition.

3. The excited β-bands in even-even nuclei can be interpreted as the positive-parity counterparts of higher negative-parity sequences, or in other words, as the members of non-yrast alternating-parity bands.

On the basis of these postulates the extended alternating-parity spectrum of an even-even nucleus has the following form:

- The yrast alternating-parity set has the quantum number $n = 0$ and consists of the g-band (ground state band) with the quantum number $k = k_0^{(+)}$ and the angular momenta and parities $I_\nu^\pi = 0_1^+, 2_1^+, 4_1^+, 6_1^+, \ldots$ together with the first negative-parity band denoted as $n1$ with $k = k_0^{(-)}$ and $I_\nu^\pi = 1_1^-, 3_1^-, 5_1^-, \ldots$

- The first non-yrast set has the quantum number $n = 1$ and consists of the first β-band with the quantum number $k = k_1^{(+)}$ and the angular momenta and parities $I_\nu^\pi = 0_2^+, 2_2^+, 4_2^+, 6_2^+, \ldots$ together with the second negative-parity band denoted as $n2$ with $k = k_1^{(-)}$ and $I_\nu^\pi = 1_2^-, 3_2^-, 5_2^-, \ldots$

- The second non-yrast set has the quantum number $n = 2$ and consists of the second β-band with the quantum number $k = k_2^{(+)}$ and the angular momenta and parities $I_\nu^\pi = 0_3^+, 2_3^+, 4_3^+, 6_3^+, \ldots$ together with the third negative-parity band denoted as $n3$ with $k = k_2^{(-)}$ and $I_\nu^\pi = 1_3^-, 3_3^-, 5_3^-, \ldots$

3.2. Theory of transition operators for non-yrast bands

The basic CQOM concept for the calculation of electromagnetic transition probabilities can be found in [16]. We extend this formalism to describe reduced B(E1), B(E2) and B(E3) transition probabilities also in the higher lying alternating-parity bands. This extension takes place with two modifications. One of them is very straightforward: one simply uses higher quantum numbers.

The other modification is a generalization of the transition operators. Because of the complicated possible shapes of the quadrupole-octupole wave functions it was necessary to generalize the angular parts of the operators.

In continuation to the above mentioned transition theory, we can write the $\hat{Q}$-operators (2.56) as

$$\hat{Q}_{10} = M_1 pq\eta^2 \cos\phi \sin\phi \tag{3.3}$$
$$\hat{Q}_{20} = M_2 p\eta \cos\phi \tag{3.4}$$
$$\hat{Q}_{30} = M_3 q\eta \sin\phi\,. \tag{3.5}$$

The operators (3.3)-(3.5) correspond to a fixed nuclear shape situation with fixed values of β_2 and β_3. In case of the CQOM the density distribution can have many maxima. Some example plots are given for illustration in Figures 3.1 and 3.2.

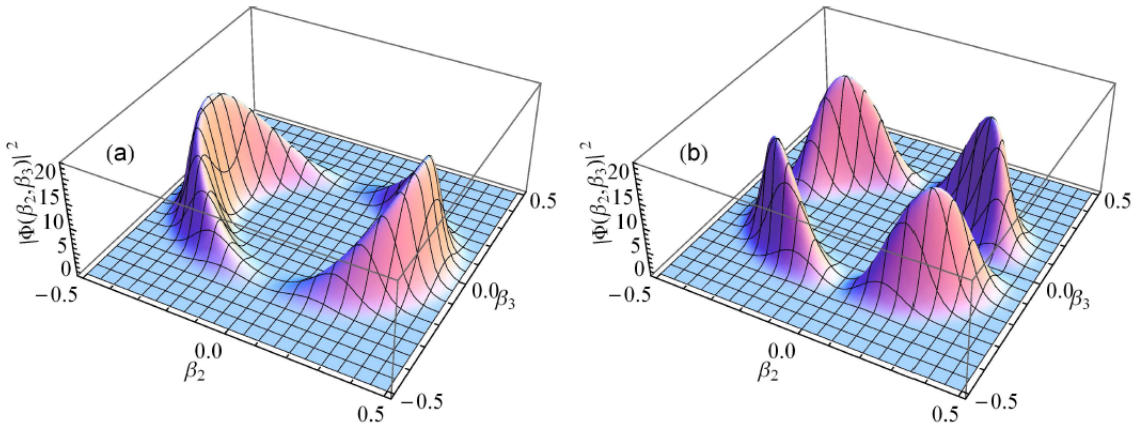

Figure 3.1.: Density distribution $\rho_{nkI}(\beta_2,\beta_3) = |\Phi^{\pi}_{nkI}(\beta_2,\beta_3)|^2$ for $k=2$, $I=1$ (left) and $k=1$, $I=2$ (right) at $n=0$ with schematic parameters. The model space corresponds to the $\beta_2 > 0$ half-plane.

This phenomenon can be interpreted as a kind of "overtones" related to the coherent collective oscillations of the system.

The original operators (3.3)-(3.5) cannot take into account multiple maxima in the collective states. As a consequence it was found that using these original operators the

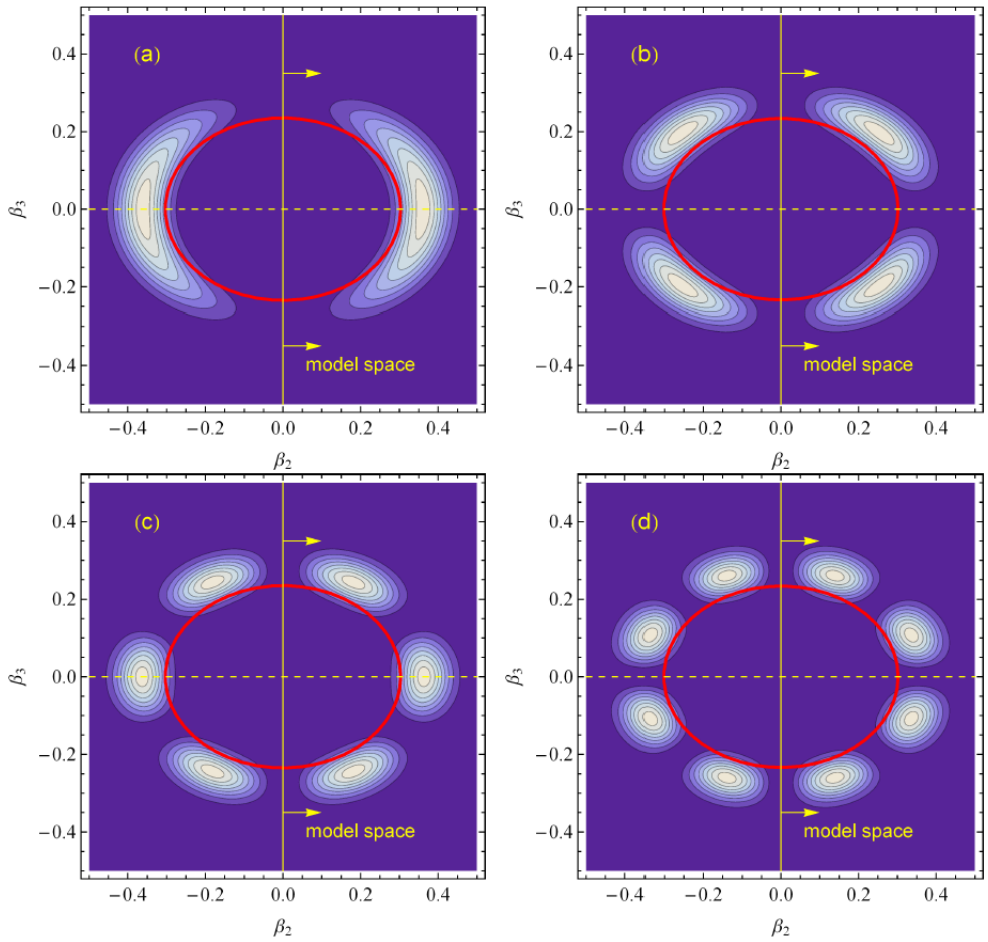

Figure 3.2.: Contour plots of the density distribution $\rho_{nkI}(\beta_2, \beta_3)$ for $k = 2$, $I = 1$ (up left) and $k = 1$, $I = 2$ (up right), $k = 3$, $I = 2$ (down left) and $k = 4$, $I = 1$ (down right) at $n = 0$ with schematic parameters. The ellipsoidal curves outline the potential bottom. The model space corresponds to the $\beta_2 > 0$ half-plane.

B(E3) transition probabilities are vanishing if the difference in the k numbers of the initial and final state wave functions is larger than one.

As explained in [17], this limitation is removed by the introduction of the following replacements:

$$\cos\phi \quad \longrightarrow \quad A_{20}(\phi) \equiv \sum_{k=1}^{\infty} a_{20}^{(k)} \cos(k\phi) \tag{3.6}$$

$$\sin\phi \quad \longrightarrow \quad A_{30}(\phi) \equiv \sum_{k=1}^{\infty} a_{30}^{(k)} \sin(k\phi)\,, \tag{3.7}$$

corresponding to a parity-conserving expansion into Fourier-series. If one choses $a^{(k)} =$

$1/k$ then the sums are convergent and the limit is known in analytical form.

$$A_{20}(\phi) = \sum_{k=1}^{\infty} \frac{\cos(k\phi)}{k} = -\frac{1}{2}\left[\ln 2 + \ln(1-\cos\phi)\right] \tag{3.8}$$

$$A_{30}(\phi) = \sum_{k=1}^{\infty} \frac{\sin(k\phi)}{k} = \frac{\pi-\phi}{2} + \pi \mathrm{Floor}\left(\frac{\phi}{2\pi}\right), \tag{3.9}$$

where $\mathrm{Floor}(x)$ is the next smaller integer to x. The angular part of the second order operator can then be generalized by replacing the factors of the product with their generalizations,

$$\cos\phi\sin\phi \longrightarrow A_{10}(\phi) \equiv A_{20}(\phi)A_{30}(\phi) = \sum_{m=1}^{\infty}\sum_{n=1}^{\infty} \frac{\cos(m\phi)}{m}\frac{\sin(n\phi)}{n}. \tag{3.10}$$

If one reduces the sums to only the first summand, the original operators are reobtained. We now redefine the transition operators (3.3)-(3.5) as

$$\hat{Q}_{10}(\eta,\phi) = M_1 pq\eta^2 A_{10}(\phi) \tag{3.11}$$

$$\hat{Q}_{20}(\eta,\phi) = M_2 p\eta A_{20}(\phi) \tag{3.12}$$

$$\hat{Q}_{30}(\eta,\phi) = M_3 q\eta A_{30}(\phi). \tag{3.13}$$

If one carries out the integration over the rotational part involving the Wigner-functions, one is left with

$$B(E\lambda; n_i k_i I_i \to n_f k_f I_f) = \frac{2\lambda+1}{4\pi(4-3\delta_{\lambda,1})}\langle I_i 0\lambda 0|I_f 0\rangle^2 R_\lambda^2(n_i k_i I_i \to n_f k_f I_f), \tag{3.14}$$

where the square of a Clebsch-Gordan coefficient appears and R_λ is given by

$$R_\lambda(n_i k_i I_i \to n_f k_f I_f) = \left\langle \Phi^{\pi_f}_{n_f k_f I_f}(\eta,\phi)|\hat{Q}_{\lambda 0}|\Phi^{\pi_i}_{n_i k_i I_i}(\eta,\phi)\right\rangle. \tag{3.15}$$

Due to the separation ansatz we can also separate the integrations, leading to

$$R_1(n_i k_i I_i \to n_f k_f I_f) = M_1 pq S_2(n_i, I_i; n_f, I_f) I_1^{\pi_i,\pi_f}(k_i, k_f) \tag{3.16}$$

$$R_2(n_i k_i I_i \to n_f k_f I_f) = M_2 p S_1(n_i, I_i; n_f, I_f) I_2^{\pi_i,\pi_f}(k_i, k_f) \tag{3.17}$$

$$R_3(n_i k_i I_i \to n_f k_f I_f) = M_3 q S_1(n_i, I_i; n_f, I_f) I_3^{\pi_i,\pi_f}(k_i, k_f), \tag{3.18}$$

where

$$S_1(n_i, I_i; n_f, I_f) = \int_0^\infty d\eta \psi^{I_f}_{n_f}(\eta)\eta^2\psi^{I_i}_{n_i}(\eta) \tag{3.19}$$

$$S_2(n_i, I_i; n_f, I_f) = \int_0^\infty d\eta \psi^{I_f}_{n_f}(\eta)\eta^3\psi^{I_i}_{n_i}(\eta) \tag{3.20}$$

and

$$I_\lambda^{\pi_i,\pi_f}(k_i,k_f) = \frac{2}{\pi}\int_{-\frac{\pi}{2}}^{\frac{\pi}{2}} A_{\lambda 0}(\phi)\varphi^{\pi_f}_{k_f}(\phi)\varphi^{\pi_i}_{k_i}(\phi)d\phi, \quad \lambda = 1,2,3. \tag{3.21}$$

Analytical expressions for these integrals are worked out and are presented in appendix A.4.

3.3. Relations between ellipsoidal and Hamiltonian parameters

There are a number of very easy relations between the ellipsoidal parameters ω, b, d_0, c, p and those parameters initially appearing in the Hamiltonian, i.e. B_2, B_3, C_2, C_3, d_2, d_3 and d_0. This makes it possible to calculate the unknown set of parameters if one parameter set is known. If the ellipsoidal parameters are given for example, then we immediately have the "Cartesian" parameters by means of

$$d_2 = \frac{2c}{\omega b p^2} \tag{3.22}$$

$$d_3 = (2p^2 - 1) \cdot d_2 \tag{3.23}$$

$$B_2 = \frac{b}{2} \cdot d_2 \tag{3.24}$$

$$B_3 = \frac{b}{2} \cdot d_3 \tag{3.25}$$

$$C_2 = \frac{\omega^2 b}{2} \cdot d_2 \tag{3.26}$$

$$C_3 = \frac{\omega^2 b}{2} \cdot d_3 \,. \tag{3.27}$$

3.4. Numerical results and discussion

The presented formalism was applied to the nuclei ^{152,154}Sm, ^{154,156,158}Gd, ^{236}U and ^{100}Mo. The experimental data is taken from the ENSDF database [72] and the theoretical energy levels are obtained by taking

$$\tilde{E}_{n,k}(I) = E_{n,k}(I) - E_{0,k_0^{(+)}}(0) \,. \tag{3.28}$$

The model parameters ω, b, d_0, c, p and the effective charge e^1_{eff} are adjusted to the experimental energy levels and transitions. This is done individually for each considered nucleus. Additionally the calculations are performed for different possible k quantum numbers within the limit $1 \leq k \leq 20$ and those providing the best model description are chosen. The resulting parameters are shown in Table 3.1. The corresponding parameters of the original Hamiltonian formulated with β_2 and β_3 are given in Table 3.2.

As the reader might notice the parameters do not vary very smoothly, even for the quite neighbouring nuclei from the rare-earth region. This phenomenon repeats for the case of non-coherent quadrupole-octupole motion, as we will see further down. One possible explanation for this could be the following.

The parameters determine the shape of the potential and therefore also the shape of the wave functions. The ground state wave function at angular momentum $I = 0$ can be

used to calculate the quadrupole deformation expectation values of the nuclei. In case of smoothly varying parameters these deformation expectation values would lie very closely together. Instead, as we will see below, the wave functions have individual shapes for the different nuclei and the deformation expectation values calculated from them follow the experimentally known deformation parameters.

To further conclude, I can repeat a statement from [17]: "The results show that the model scheme correctly reproduces the structure of the alternating-parity spectra in the considered nuclei with a reasonable good agreement between the theoretical and experimental energy levels. (...) Further, the formalism takes into account the complex-shape effects in the motion of the system and in addition provides estimations about the shape of the quadrupole-octupole potential which governs the collective properties of the considered nuclei."

For a detailed discussion of the properties of the individual nuclei the interested reader is referred to the before cited paper.

Table 3.1.: Parameters of the model fits.

Nucl	ω [MeV/$\hbar$]	b [$\hbar^{-2}$]	d_0 [$\hbar^2$]	c	p	e^1_{eff} [e]
^{152}Sm	0.295	2.450	78.8	113.2	0.854	1.01
^{154}Sm	0.205	4.625	108.5	132.6	0.808	1.017
^{154}Gd	0.306	2.948	114.7	113.4	0.777	1.048
^{156}Gd	0.439	1.642	197.6	141.5	0.849	0.723
^{158}Gd	0.168	3.626	42.6	39.7	0.864	0.435
^{236}U	0.402	1.404	539.3	343.4	0.949	0.134
^{100}Mo	0.318	2.674	1.366	54.6	0.715	0.282

Table 3.2.: Resulting mass parameters B_2 and B_3 (in $\hbar^2$/MeV) and parameters of the model potential C_2 and C_3 (in MeV), d_2 and d_3 (in $\hbar^2$/MeV).

Nucl	B_2	B_3	C_2	C_3	d_2	d_3
^{152}Sm	525	241	45.8	21.0	429	197
^{154}Sm	987	303	41.7	12.8	427	131
^{154}Gd	613	127	57.6	11.9	416	86
^{156}Gd	447	197	86.2	38.0	545	240
^{158}Gd	317	156	8.9	4.4	175	86
^{236}U	948	760	153	123	1351	1083
^{100}Mo	337	7	34.0	0.7	252	6

Table 3.3.: Theoretical and experimental values of B(E1), B(E2) and B(E3) transition probabilities in Weisskopf units (W.u.) for alternating-parity spectra of several even-even nuclei. Notations: g (ground-state band), $b1$ (first β-band), $b2$ (second β-band), $n1$ (first negative-parity band), $n2$ (second negative-parity band), $n3$ (third negative-parity band). The data are taken from [79] except for those for B($E3; 3^-_{n1} \to 0^+_g$) transitions, which are taken from [43]. The parity signs (+) for the even and (−) for the odd angular momenta, respectively are omitted in the labels of the states to avoid overloading of notations. The uncertainties (in parentheses) refer to the last significant digits in the experimental data.

Mult	Transition	Th [W.u.]	Exp [W.u.]	Mult	Transition	Th [W.u.]	Exp [W.u.]
			^{152}Sm				
$E2$	$2_g \to 0_g$	141	144 (3)	$E2$	$3_{n2} \to 1_{n2}$	52	
$E2$	$4_g \to 2_g$	210	209 (3)	$E2$	$5_{n2} \to 3_{n2}$	63	
$E2$	$6_g \to 4_g$	248	245 (5)	$E3$	$3_{n1} \to 0_g$	14	14 (2)
$E2$	$8_g \to 6_g$	284	285 (14)	$E3$	$3_{n2} \to 0_{b1}$	10	
$E2$	$10_g \to 8_g$	322	320 (3)	$E3$	$1_{n1} \to 4_g$	69	
$E2$	$12_g \to 10_g$	363		$E3$	$1_{n2} \to 4_{b1}$	70	
$E1$	$1_{n1} \to 0_g$	0.0041	0.0042 (4)	$E2$	$2_{b1} \to 0_g$	1.26	0.92 (8)
$E1$	$1_{n1} \to 2_g$	0.0088	0.0077 (7)	$E2$	$4_{b1} \to 2_g$	0.2	0.7 (2)
$E1$	$3_{n1} \to 2_g$	0.0056	0.0081 (16)	$E2$	$2_{b1} \to 2_g$	4.6	5.5 (5)
$E1$	$3_{n1} \to 4_g$	0.0087	0.0082 (16)	$E2$	$4_{b1} \to 4_g$	4.2	5.4 (13)
$E1$	$1_{n2} \to 0_{b1}$	0.0041		$E2$	$2_{b1} \to 4_g$	27.4	19.2 (18)

continues on next page

Table 3, *continued*

Mult	Transition	Th [W.u.]	Exp [W.u.]	Mult	Transition	Th [W.u.]	Exp [W.u.]
$E1$	$1_{n2} \to 2_{b1}$	0.0095		$E2$	$4_{b1} \to 6_g$	35	4 (2)
$E2$	$2_{b1} \to 0_{b1}$	160	107 (27)	$E2$	$0_{b1} \to 2_g$	30	
$E2$	$4_{b1} \to 2_{b1}$	232	204 (38)	$E1$	$1_{n1} \to 2_{b1}$	0.00402	0.00013 (4)
$E2$	$3_{n1} \to 1_{n1}$	47		$E1$	$1_{n1} \to 0_{b1}$	0.0023	
$E2$	$5_{n1} \to 3_{n1}$	58		$E1$	$1_{n2} \to 0_g$	0.00006	
			^{154}Sm				
$E2$	$2_g \to 0_g$	168	176 (1)	$E2$	$5_{n2} \to 3_{n2}$	82	
$E2$	$4_g \to 2_g$	247	245 (6)	$E2$	$3_{n3} \to 1_{n3}$	72	
$E2$	$6_g \to 4_g$	287	289 (8)	$E3$	$3_{n1} \to 0_g$	10	10 (2)
$E2$	$8_g \to 6_g$	322	319 (17)	$E3$	$1_{n1} \to 4_g$	50	
$E2$	$10_g \to 8_g$	358	314 (16)	$E3$	$3_{n2} \to 0_{b1}$	77	
$E2$	$12_g \to 10_g$	398	282 (19)	$E3$	$1_{n2} \to 4_{b1}$	381	
$E1$	$1_{n1} \to 0_g$	0.0051	0.0058 (4)	$E3$	$3_{n3} \to 0_{b2}$	6	
$E1$	$1_{n1} \to 2_g$	0.0110	0.0113 (7)	$E3$	$1_{n3} \to 4_{b2}$	62	
$E1$	$3_{n1} \to 2_g$	0.0069	0.0080 (11)	$E2$	$0_{b1} \to 2_g$	1	12 (3)
$E1$	$3_{n1} \to 4_g$	0.0106	0.0092 (13)	$E2$	$2_{b1} \to 0_g$	0.36	<0.58
$E1$	$1_{n2} \to 0_{b1}$	0.0109		$E2$	$2_{b1} \to 2_g$	0.39	<1.3
$E1$	$1_{n2} \to 2_{b1}$	0.0231		$E2$	$2_{b1} \to 4_g$	0.27	<2.4
$E1$	$1_{n3} \to 0_{b2}$	0.0044		$E2$	$0_{b2} \to 2_g$	5×10^{-6}	
$E1$	$1_{n3} \to 2_{b2}$	0.0109		$E2$	$0_{b2} \to 2_{b1}$	16	
$E2$	$2_{b1} \to 0_{b1}$	65		$E1$	$0_{b1} \to 1_{n1}$	0.0005	
$E2$	$4_{b1} \to 2_{b1}$	93		$E1$	$1_{n2} \to 0_g$	0.0005	
$E2$	$2_{b2} \to 0_{b2}$	68		$E1$	$1_{n2} \to 0_{b2}$	0.0058	
$E2$	$4_{b2} \to 2_{b2}$	97		$E1$	$1_{n3} \to 0_{b1}$	3×10^{-7}	
$E2$	$3_{n1} \to 1_{n1}$	60		$E1$	$1_{n3} \to 0_g$	8×10^{-5}	
$E2$	$5_{n1} \to 3_{n1}$	72		$E3$	$3_{n2} \to 0_g$	1.7	
$E2$	$3_{n2} \to 1_{n2}$	69		$E3$	$3_{n3} \to 0_g$	0.4	
			^{154}Gd				
$E2$	$2_g \to 0_g$	160	157 (1)	$E2$	$5_{n2} \to 3_{n2}$	64	
$E2$	$4_g \to 2_g$	235	245 (9)	$E2$	$3_{n3} \to 1_{n3}$	51	
$E2$	$6_g \to 4_g$	273	285 (15)	$E3$	$3_{n1} \to 0_g$	21	21 (5)
$E2$	$8_g \to 6_g$	306	312 (17)	$E3$	$3_{n2} \to 0_{b1}$	32	
$E2$	$10_g \to 8_g$	340	360 (4)	$E3$	$3_{n3} \to 0_{b2}$	144	
$E2$	$12_g \to 10_g$	377		$E3$	$1_{n1} \to 4_g$	102	
$E1$	$1_{n1} \to 0_g$	0.0102	0.0436	$E3$	$1_{n2} \to 4_{b1}$	179	
$E1$	$1_{n1} \to 2_g$	0.0216	0.0485	$E3$	$1_{n3} \to 4_{b2}$	708	
$E1$	$3_{n1} \to 2_g$	0.0137		$E2$	$0_{b1} \to 2_g$	25	52 (8)

continues on next page

Table 3, *continued*

Mult	Transition	Th [W.u.]	Exp [W.u.]	Mult	Transition	Th [W.u.]	Exp [W.u.]
$E1$	$3_{n1} \to 4_g$	0.0207		$E2$	$2_{b1} \to 0_g$	1.23	0.86 (7)
$E1$	$1_{n2} \to 0_{b1}$	0.0152		$E2$	$2_{b1} \to 4_g$	22.6	19.6 (16)
$E1$	$1_{n2} \to 2_{b1}$	0.0333		$E2$	$0_{b2} \to 2_g$	0.0553	
$E1$	$1_{n3} \to 0_{b2}$	0.0333		$E2$	$0_{b2} \to 2_{b1}$	14	
$E1$	$1_{n3} \to 2_{b2}$	0.0706		$E1$	$1_{n1} \to 0_{b1}$	0.0054	0.0057
$E2$	$2_{b1} \to 0_{b1}$	177	97 (10)	$E1$	$1_{n1} \to 2_{b1}$	0.0099	0.0064
$E2$	$4_{b1} \to 2_{b1}$	256		$E1$	$1_{n2} \to 0_g$	2×10^{-5}	
$E2$	$2_{b2} \to 0_{b2}$	85		$E1$	$1_{n2} \to 0_{b2}$	0.0094	
$E2$	$4_{b2} \to 2_{b2}$	122		$E1$	$1_{n3} \to 0_{b1}$	0.00023	
$E2$	$3_{n1} \to 1_{n1}$	55		$E1$	$1_{n3} \to 0_g$	2×10^{-6}	
$E2$	$5_{n1} \to 3_{n1}$	67		$E3$	$3_{n2} \to 0_g$	1.8	
$E2$	$3_{n2} \to 1_{n2}$	54		$E3$	$3_{n3} \to 0_g$	0.05	
			^{156}Gd				
$E2$	$2_g \to 0_g$	150	187 (5)	$E2$	$3_{n2} \to 1_{n2}$	44	
$E2$	$4_g \to 2_g$	219	263 (5)	$E2$	$5_{n2} \to 3_{n2}$	53	
$E2$	$6_g \to 4_g$	249	295 (8)	$E3$	$3_{n1} \to 0_g$	16.9	16.9 (7)
$E2$	$8_g \to 6_g$	273	320 (14)	$E3$	$3_{n2} \to 0_{b1}$	64	
$E2$	$10_g \to 8_g$	296	314 (14)	$E3$	$1_{n1} \to 4_g$	73	
$E2$	$12_g \to 10_g$	321	300 (3)	$E3$	$1_{n2} \to 4_{b1}$	282	
$E1$	$1_{n1} \to 0_g$	0.0006	0.0019 (14)	$E2$	$0_{b1} \to 2_g$	5	8 (4)
$E1$	$1_{n1} \to 2_g$	0.0013	0.0025 (18)	$E2$	$2_{b1} \to 0_g$	0.32	0.63 (6)
$E1$	$3_{n1} \to 2_g$	0.00083	0.00098 (21)	$E2$	$4_{b1} \to 2_g$	0.1	1.3 (7)
$E1$	$3_{n1} \to 4_g$	0.0012	0.00077 (16)	$E2$	$4_{b1} \to 6_g$	5.6	2.1 (11)
$E1$	$1_{n2} \to 0_{b1}$	0.0013		$E2$	$2_{b1} \to 4_g$	4.3	4.1 (4)
$E1$	$1_{n2} \to 2_{b1}$	0.0026	0.0005 (3)	$E1$	$1_{n1} \to 0_{b1}$	0.0002	0.0004 (3)
$E1$	$3_{n2} \to 2_{b1}$	0.0016		$E1$	$1_{n2} \to 0_g$	6×10^{-6}	0.0019 (7)
$E2$	$2_{b1} \to 0_{b1}$	74	52 (23)	$E1$	$1_{n2} \to 2_g$	2×10^{-5}	0.0043 (15)
$E2$	$4_{b1} \to 2_{b1}$	107	280 (15)	$E1$	$3_{n2} \to 2_g$	5×10^{-6}	0.0019 (14)
$E2$	$6_{b1} \to 4_{b1}$	120		$E1$	$3_{n2} \to 4_g$	2×10^{-5}	0.0031 (4)
$E2$	$3_{n1} \to 1_{n1}$	46		$E3$	$3_{n2} \to 0_g$	0.21	
$E2$	$5_{n1} \to 3_{n1}$	56					
			^{158}Gd				
$E2$	$2_g \to 0_g$	181	198 (6)	$E2$	$0_{b1} \to 2_g$	8.7619	1.1652
$E2$	$4_g \to 2_g$	274	289 (5)	$E2$	$2_{b1} \to 0_g$	2.36	0.31 (4)
$E2$	$6_g \to 4_g$	332		$E2$	$2_{b1} \to 2_g$	2.913	0.079 (14)
$E2$	$8_g \to 6_g$	393	330 (3)	$E2$	$4_{b1} \to 4_g$	2.40	0.37
$E2$	$10_g \to 8_g$	460	340 (3)	$E2$	$2_{b1} \to 4_g$	2.96	1.39 (15)

continues on next page

Table 3, *continued*

Mult	Transition	Th [W.u.]	Exp [W.u.]	Mult	Transition	Th [W.u.]	Exp [W.u.]
$E2$	$12_g \to 10_g$	532	310 (3)	$E2$	$0_{b2} \to 2_g$	1.86	2.09
$E1$	$1_{n1} \to 0_g$	0.0001	$9.8443\times10^{-5}(4)$	$E2$	$2_{b2} \to 0_g$	0.68	0.37 (4)
$E1$	$1_{n1} \to 2_g$	2.5×10^{-4}	$9.6515\times10^{-5}(6)$	$E2$	$2_{b2} \to 4_g$	0.43	0.38 (6)
$E1$	$3_{n1} \to 2_g$	0.00015	0.00033 (10)	$E2$	$4_{b1} \to 2_g$	3.75	1.32
$E1$	$3_{n1} \to 4_g$	0.00028	0.00029 (8)	$E2$	$4_{b1} \to 6_g$	1.30	3.16
$E1$	$5_{n1} \to 4_g$	2.02×10^{-4}	$7.4324\times10^{-4}(13)$	$E2$	$0_{b2} \to 2_{b1}$	57	
$E1$	$5_{n1} \to 6_g$	3.62×10^{-4}	$5.8691\times10^{-4}(8)$	$E1$	$0_{b1} \to 1_{n1}$	2.7×10^{-5}	3.314×10^{-6}
$E1$	$3_{n2} \to 2_{b1}$	0.00011	> 0.00035	$E1$	$2_{b1} \to 1_{n1}$	8.3×10^{-6}	$6.4\times10^{-5}(8)$
$E1$	$1_{n2} \to 0_{b1}$	8.02×10^{-5}		$E1$	$2_{b1} \to 3_{n1}$	2×10^{-5}	$1.89\times10^{-4}(24)$
$E1$	$1_{n2} \to 2_{b1}$	0.0002		$E1$	$1_{n2} \to 2_g$	4×10^{-5}	0.0064
$E1$	$1_{n3} \to 0_{b2}$	0.0004		$E1$	$1_{n2} \to 0_g$	2×10^{-5}	0.0035 (12)
$E1$	$1_{n3} \to 2_{b2}$	0.0009		$E1$	$3_{n2} \to 2_g$	3×10^{-5}	>0.0011
$E1$	$3_{n3} \to 2_{b2}$	0.0005		$E1$	$3_{n2} \to 4_g$	3×10^{-5}	>0.0015
$E2$	$2_{b1} \to 0_{b1}$	200		$E1$	$0_{b2} \to 1_{n1}$	2×10^{-7}	5.7831×10^{-5}
$E2$	$4_{b1} \to 2_{b1}$	288	455	$E1$	$2_{b2} \to 1_{n1}$	2×10^{-8}	$2.7\times10^{-6}(19)$
$E2$	$2_{b2} \to 0_{b2}$	217		$E1$	$2_{b2} \to 3_{n1}$	2×10^{-7}	$3.7\times10^{-5}(5)$
$E2$	$4_{b2} \to 2_{b2}$	308		$E1$	$0_{b2} \to 1_{n2}$	6×10^{-5}	6.02×10^{-4}
$E2$	$3_{n1} \to 1_{n1}$	185		$E1$	$2_{b2} \to 1_{n2}$	1.8×10^{-5}	$1.50\times10^{-4}(21)$
$E2$	$5_{n1} \to 3_{n1}$	227	369 (6)	$E1$	$2_{b2} \to 3_{n2}$	4.2×10^{-5}	$2.40\times10^{-4}(5)$
$E2$	$3_{n2} \to 1_{n2}$	200	> 1600	$E1$	$4_{b1} \to 3_{n1}$	7.7×10^{-6}	4.63×10^{-4}
$E2$	$5_{n2} \to 3_{n2}$	240		$E1$	$4_{b1} \to 5_{n1}$	2.1×10^{-5}	6.12×10^{-4}
$E2$	$3_{n3} \to 1_{n3}$	241		$E1$	$1_{n2} \to 0_{b2}$	2×10^{-5}	
$E3$	$3_{n1} \to 0_g$	11.9	11.9 (7)	$E1$	$1_{n3} \to 0_{b1}$	3×10^{-6}	
$E3$	$1_{n1} \to 4_g$	81		$E1$	$1_{n3} \to 0_g$	0.00001	
$E3$	$3_{n2} \to 0_{b1}$	519		$E3$	$3_{n2} \to 0_g$	5	
$E3$	$3_{n3} \to 0_{b2}$	102		$E3$	$3_{n3} \to 0_g$	2	
			^{236}U				
$E2$	$2_g \to 0_g$	237	250 (10)	$E2$	$2_{b1} \to 0_{b1}$	112	
$E2$	$4_g \to 2_g$	342	357 (23)	$E2$	$4_{b1} \to 2_{b1}$	160	
$E2$	$6_g \to 4_g$	382	385 (22)	$E2$	$3_{n1} \to 1_{n1}$	68	
$E2$	$8_g \to 6_g$	408	390 (4)	$E2$	$5_{n1} \to 3_{n1}$	80	
$E2$	$10_g \to 8_g$	429	360 (4)	$E2$	$7_{n1} \to 5_{n1}$	87	
$E2$	$12_g \to 10_g$	450	410 (7)	$E2$	$3_{n2} \to 1_{n2}$	54	
$E2$	$14_g \to 12_g$	471	450 (5)	$E2$	$5_{n2} \to 3_{n2}$	64	
$E2$	$16_g \to 14_g$	493	380 (4)	$E3$	$1_{n1} \to 4_g$	62	62 (9)
$E2$	$18_g \to 16_g$	516	490 (5)	$E3$	$3_{n1} \to 0_g$	15	23 (3)
$E2$	$20_g \to 18_g$	539	510 (8)	$E3$	$1_{n2} \to 4_{b1}$	695	
$E2$	$22_g \to 20_g$	564	520 (12)	$E3$	$3_{n2} \to 0_{b1}$	172	
$E2$	$24_g \to 22_g$	590	670 (13)	$E2$	$0_{b1} \to 2_g$	6	

continues on next page

Table 3, *continued*

Mult	Transition	Th [W.u.]	Exp [W.u.]	Mult	Transition	Th [W.u.]	Exp [W.u.]
$E2$	$26_g \to 24_g$	617	670 (19)	$E2$	$2_{b1} \to 0_g$	0.66	
$E2$	$28_g \to 26_g$	645	1100 (5)	$E2$	$4_{b1} \to 2_g$	0.59	
$E1$	$1_{n1} \to 0_g$	2.7×10^{-8}	$2.7\times10^{-8}(4)$	$E2$	$2_{b1} \to 4_g$	4	
$E1$	$1_{n1} \to 2_g$	5.5×10^{-8}		$E1$	$0_{b1} \to 1_{n1}$	1.2×10^{-8}	
$E1$	$3_{n1} \to 2_g$	3.5×10^{-8}		$E1$	$2_{b1} \to 1_{n1}$	4.6×10^{-9}	
$E1$	$3_{n1} \to 4_g$	4.8×10^{-8}		$E1$	$1_{n2} \to 0_g$	1.6×10^{-9}	
$E1$	$1_{n2} \to 0_{b1}$	2.0×10^{-8}		$E3$	$3_{b2} \to 0_g$	0.14	
$E1$	$1_{n2} \to 2_{b1}$	4.0×10^{-8}					
			^{100}Mo				
$E2$	$2_g \to 0_g$	22.7	37.0 (7)	$E2$	$3_{n1} \to 1_{n1}$	16	
$E2$	$4_g \to 2_g$	50	69 (4)	$E2$	$5_{n1} \to 3_{n1}$	21	
$E2$	$6_g \to 4_g$	84	94 (14)	$E2$	$7_{n1} \to 5_{n1}$	26	
$E2$	$8_g \to 6_g$	120	123 (18)	$E2$	$3_{n2} \to 1_{n2}$	18	
$E2$	$10_g \to 8_g$	156		$E2$	$5_{n2} \to 3_{n2}$	22	
$E1$	$1_{n1} \to 0_g$	2×10^{-6}		$E3$	$3_{n1} \to 0_g$	34	34 (3)
$E1$	$1_{n1} \to 2_g$	1×10^{-5}		$E3$	$3_{n2} \to 0_{b1}$	5	
$E1$	$3_{n1} \to 2_g$	7×10^{-6}	$2.7\times10^{-6}(9)$	$E3$	$1_{n1} \to 4_g$	899	
$E1$	$3_{n1} \to 4_g$	2×10^{-5}		$E2$	$0_{b1} \to 2_g$	72	92 (4)
$E1$	$1_{n2} \to 0_{b1}$	2×10^{-7}		$E2$	$2_{b1} \to 0_g$	0.5	0.62 (5)
$E1$	$1_{n2} \to 2_{b1}$	1×10^{-5}		$E2$	$4_{b1} \to 2_g$	3	
$E1$	$3_{n2} \to 2_{b1}$	3×10^{-6}		$E1$	$1_{n1} \to 0_{b1}$	8×10^{-6}	
$E1$	$3_{n2} \to 4_{b1}$	3×10^{-5}		$E1$	$1_{n1} \to 2_{b1}$	2×10^{-5}	
$E2$	$2_{b1} \to 0_{b1}$	25.4	5.5 (8)	$E1$	$3_{n1} \to 2_{b1}$	1.4×10^{-5}	$2.5\times10^{-5}(8)$
$E2$	$4_{b1} \to 2_{b1}$	45		$E1$	$1_{n2} \to 0_g$	5×10^{-7}	
$E2$	$6_{b1} \to 4_{b1}$	75		$E3$	$3_{n2} \to 0_g$	22	

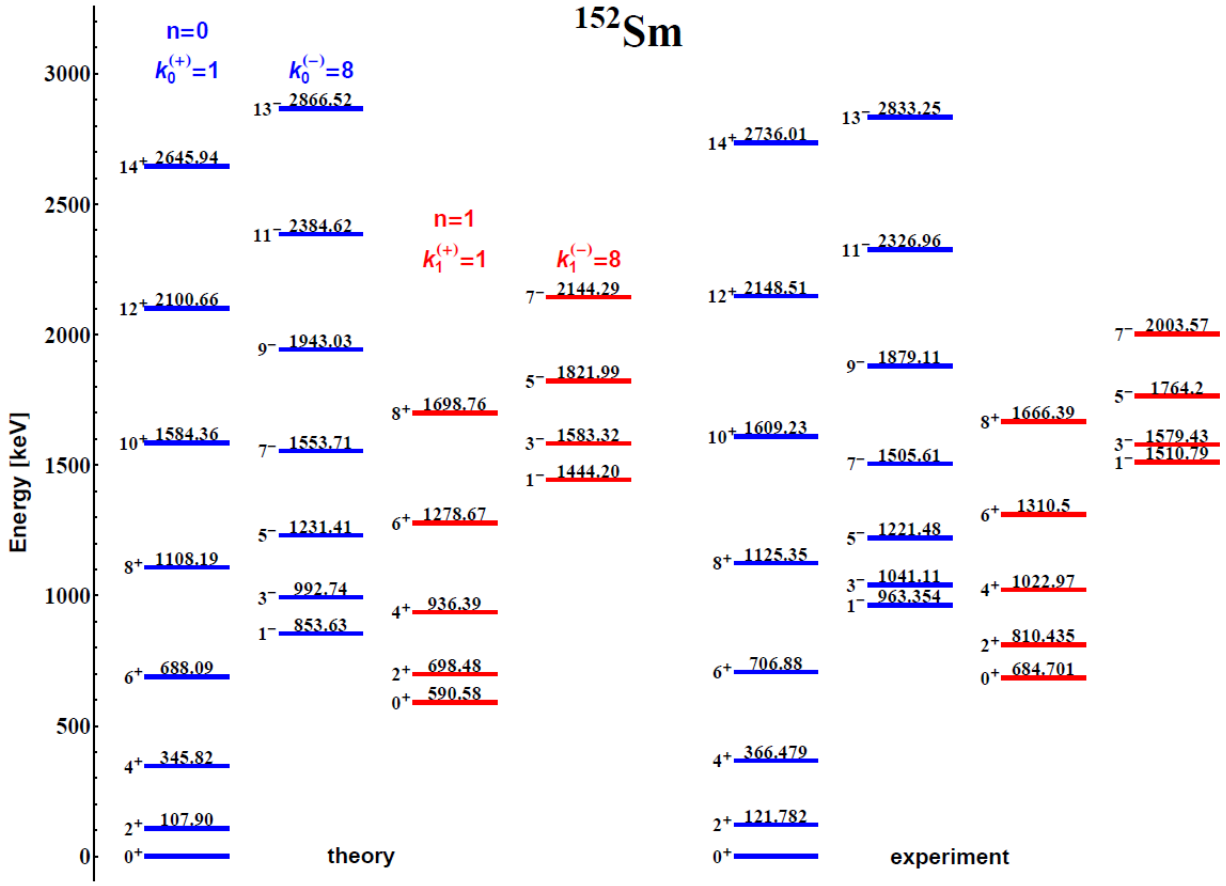

Figure 3.3.: Theoretical and experimental alternating-parity bands in ^{152}Sm. Data from [72]. The oscillation quantum numbers n, $k_n^{(+)}$ and $k_n^{(-)}$ are given above the theoretical bands.

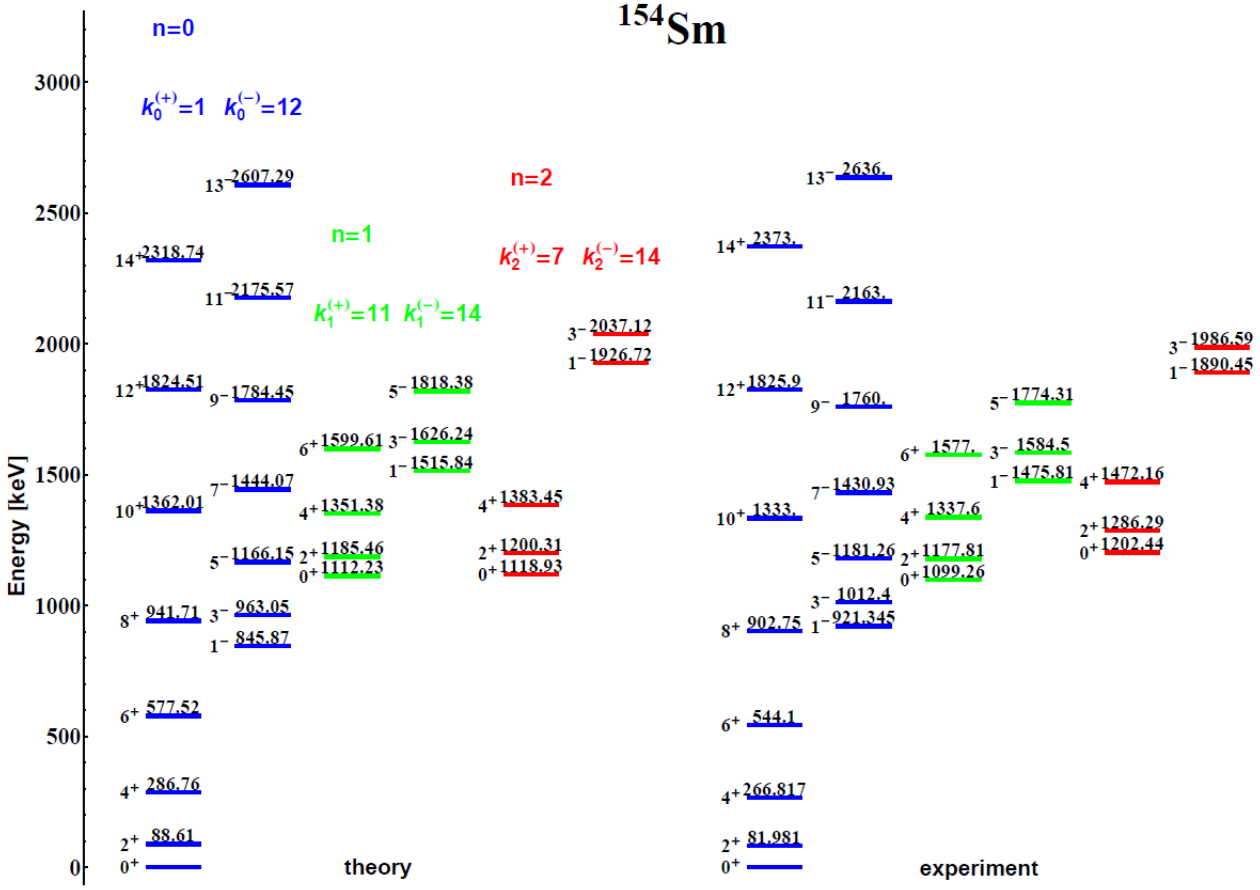

Figure 3.4.: The same as in Fig. 3.3, but for ^{154}Sm.

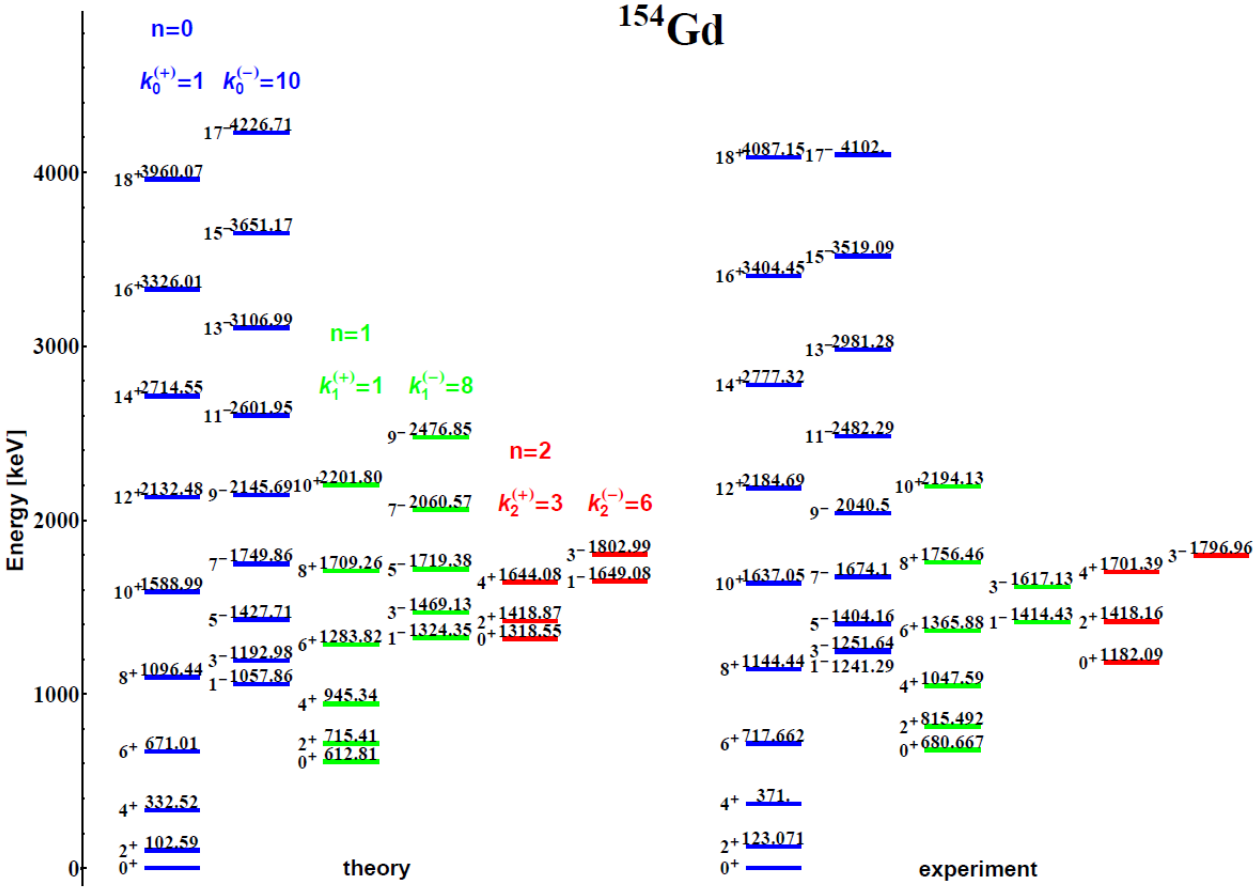

Figure 3.5.: The same as in Fig. 3.3, but for ^{154}Gd.

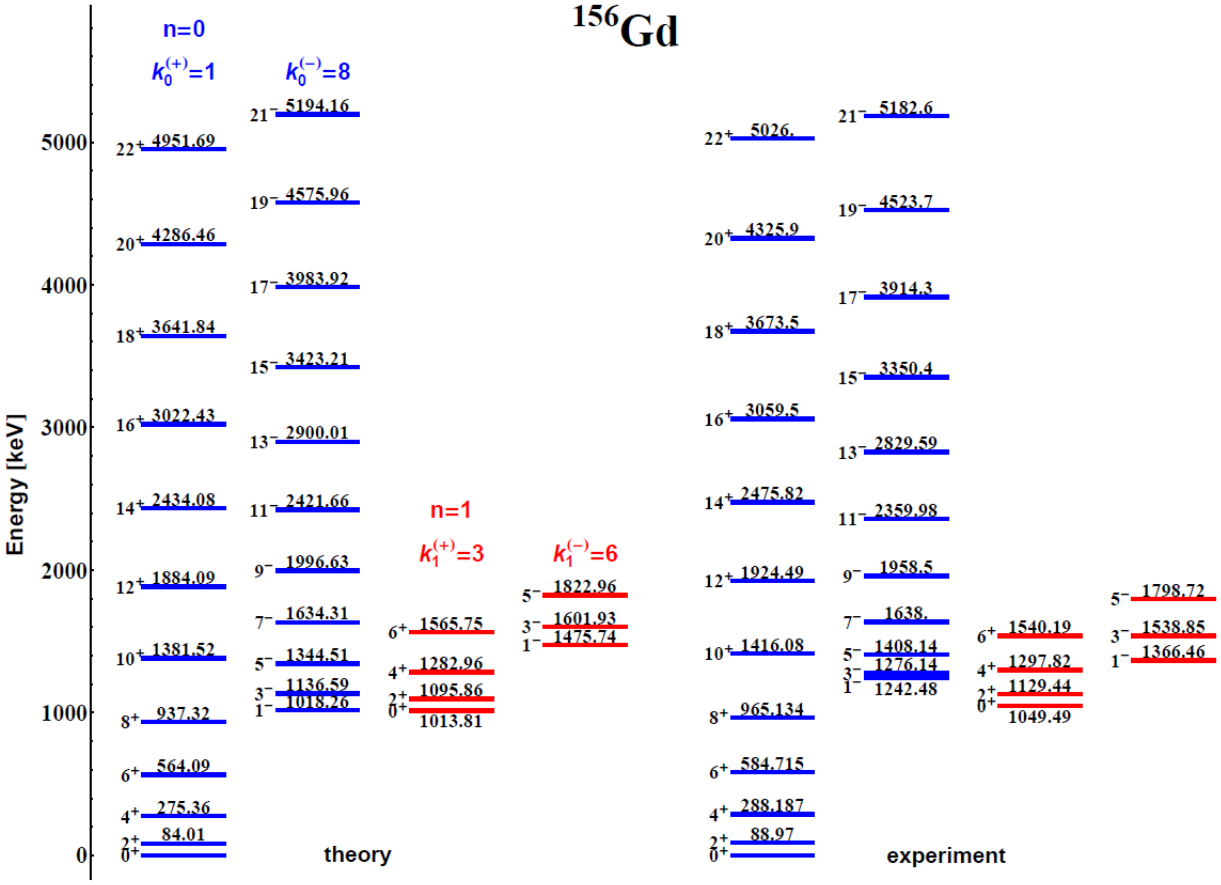

Figure 3.6.: The same as in Fig. 3.3, but for ^{156}Gd.

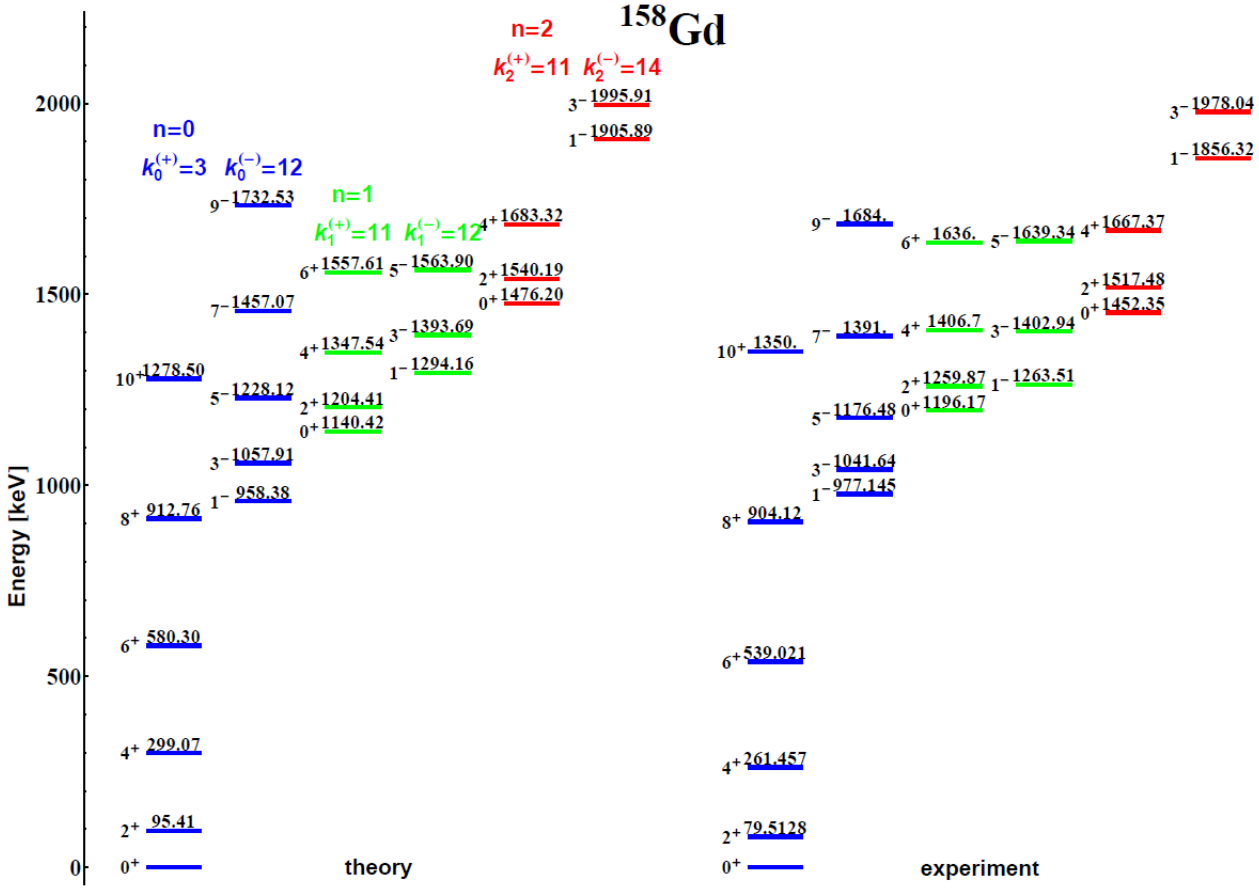

Figure 3.7.: The same as in Fig. 3.3, but for ^{158}Gd.

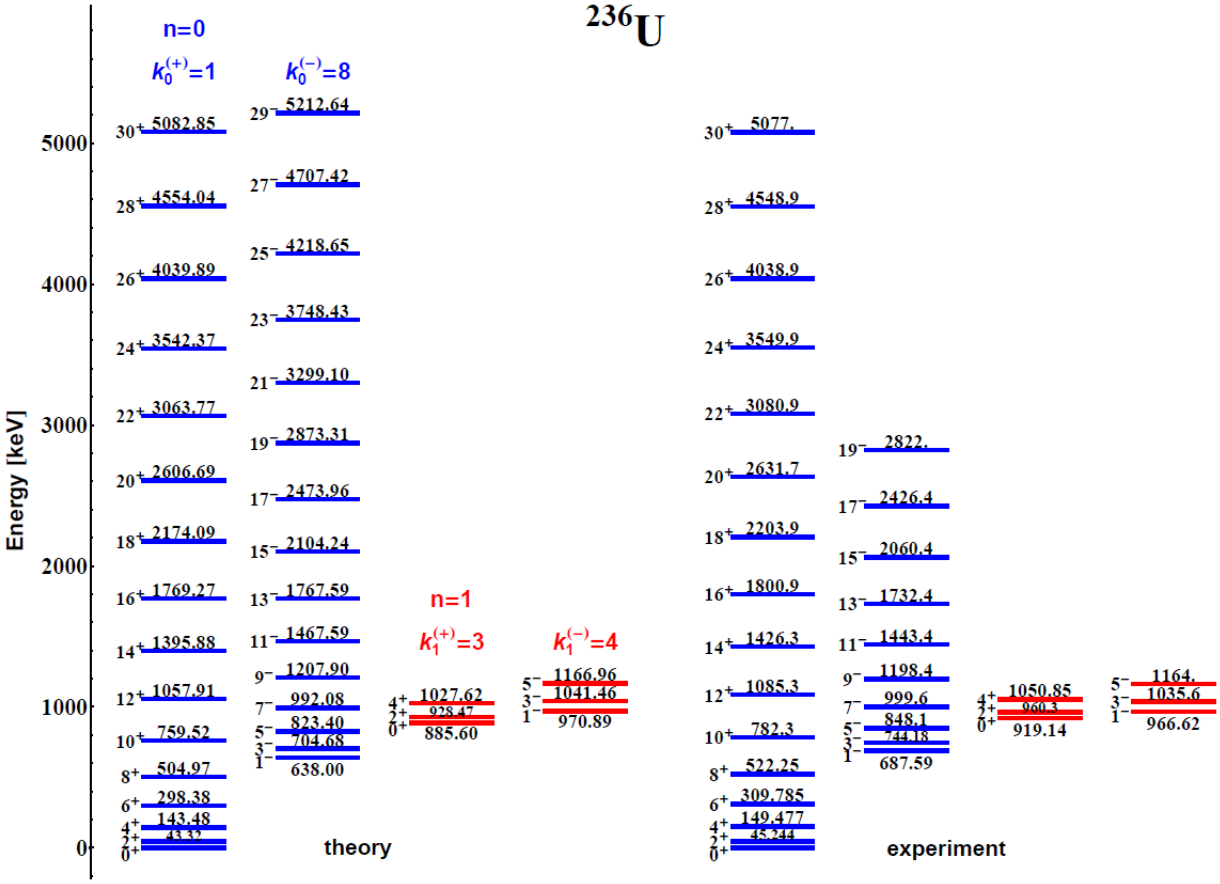

Figure 3.8.: The same as in Fig. 3.3, but for ^{236}U.

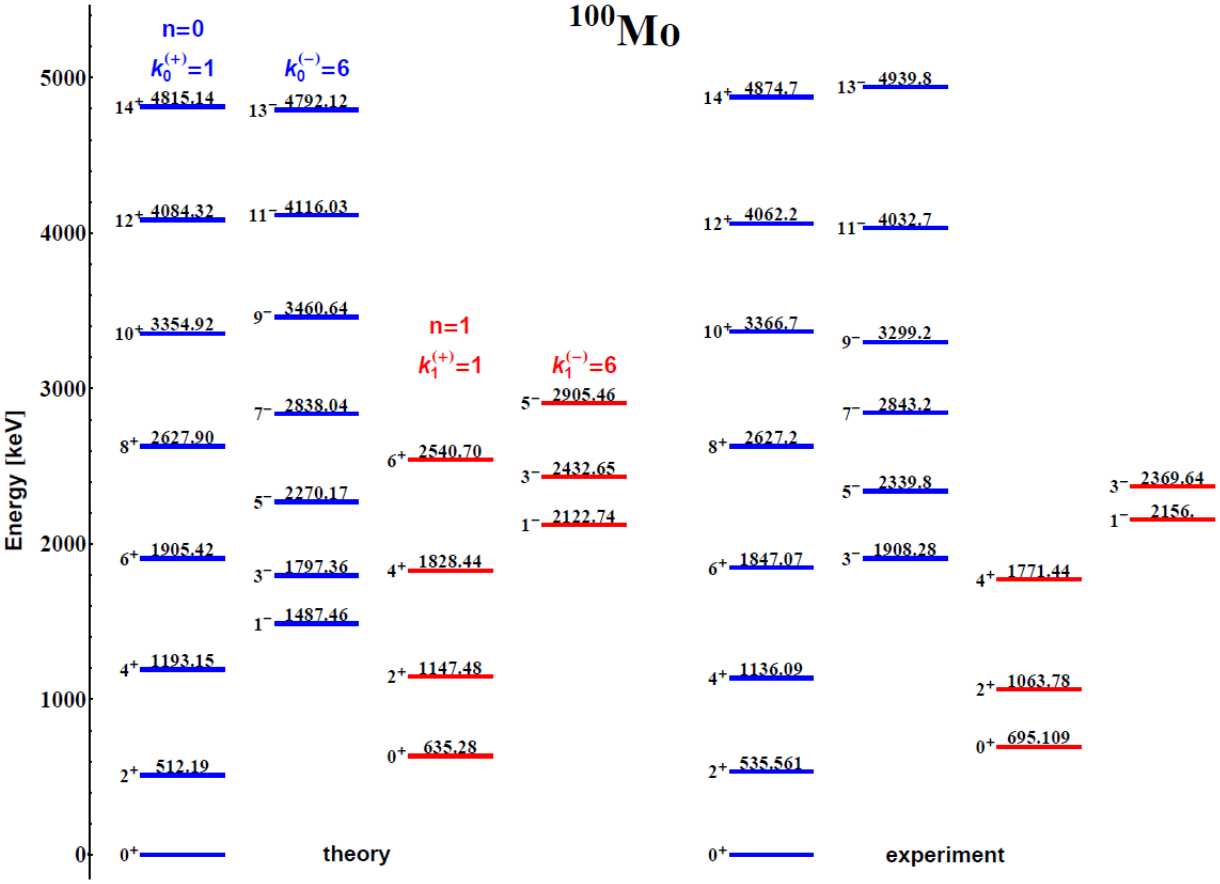

Figure 3.9.: The same as in Fig. 3.3, but for ^{100}Mo.

4. Full non-coherent numerical solution with diagonalization

It is a very natural idea to extend the coherent quadrupole-octupole model beyond the limit of coherency. In the coherent case the model is restricted to a certain class of exact analytic solutions. These can only be obtained if certain relations among the parameters are imposed (see Eq. (2.39)). In order to go beyond this restriction, more sophisticated mathematical and numerical techniques have to be sought to solve the problem. Diagonalization can provide a powerful tool to achieve this task.

4.1. The diagonalization method

Following [34], the crucial idea is to treat the Schrödinger equation as a matrix equation and to calculate the eigenvalues and eigenvectors in its matrix representation. Under the assumption that the basis states $|\varphi_n\rangle$ make up a complete orthonormal system (CONS), an arbitrary state $|\psi\rangle$ of the Hilbert space can be written as a superposition of the basis states. Suppose we want to solve the eigenvalue problem

$$\hat{H}|\psi\rangle = E|\psi\rangle\,. \tag{4.1}$$

Then, by inserting an indentity $\mathbf{1}$ at the right place

$$\mathbf{1}\hat{H}\mathbf{1}|\psi\rangle = E\mathbf{1}|\psi\rangle\,, \tag{4.2}$$

we have

$$\sum_{n,n'} |\varphi_n\rangle\langle\varphi_n|\hat{H}|\varphi_{n'}\rangle\langle\varphi_{n'}|\psi\rangle = E\sum_{n} |\varphi_n\rangle\langle\varphi_n|\psi\rangle\,. \tag{4.3}$$

Because of the linear independence of the $|\varphi_n\rangle$, for each n the equation

$$\sum_{n'} \Big(\langle\varphi_n|\hat{H}|\varphi_{n'}\rangle - E\delta_{nn'}\Big)\,\langle\varphi_{n'}|\psi\rangle = 0 \tag{4.4}$$

must hold. This leads to a homogeneous and finite linear equation system. As usual the condition that there is a non-trivial solution is given by a vanishing determinant of the coefficient matrix,

$$\det\Big(\langle\varphi_n|\hat{H}|\varphi_{n'}\rangle - E\delta_{nn'}\Big) \stackrel{!}{=} 0\,. \tag{4.5}$$

From the matrix elements

$$\langle\varphi_n|\hat{H}|\varphi_{n'}\rangle = \int \varphi_n^* \hat{H} \varphi_{n'} dV \tag{4.6}$$

one can calculate the eigenvalues E_i from (4.5) and for each E_i one can use (4.4) to calculate the components $\langle\varphi_{n'}|\psi_i\rangle$ and therefore the corresponding eigenstate $|\psi_i\rangle$.

In the ideal case of $n' \to \infty$ the method is exact. In real calculations one has to study the dependence for a finite n' in order to answer convergence questions. A criterion for the choice for the basis states is given by symmetries of the problem which the basis does take into account. It is also desirable to have a fast convergence and only little numerical effort in solving the matrix elements.

4.2. Approach with coherent quadrupole-octupole basis functions

A very good approach is to take the coherent quadrupole-octupole wave functions as basis. It was checked that they are a complete orthonormal set. This basis has the nice property that one can interpret the quantum numbers and that in case of coherence ($\omega_2 = \omega_3$) the matrix representation of the Hamiltonian is already diagonal and only becomes non-diagonal as one goes away from the case of coherence.

Moreover this basis has the nice property that the Hamiltonian matrix elements can be obtained in an analytic form. Although the diagonalization is performed numerically, the problem remains analytic in the mentioned sense. This guarantees a quite fast solution.

Last but not least the wave functions of the CQOM model provide a natural choice for the basis because they automatically take into account the boundary condition (2.45) of the model.

4.3. Details of the numerical algorithm

As a first step a basis truncation is performed since the basis space is infinite-dimensional. The quantum numbers n and k, at which the basis is truncated, are determined by imposing a certain limit on the energy in the CQOM expression eq. (2.48) for a given set of model parameters.

The basis functions are completely determined if the CQOM parameters b, c and d_0 are given. The values of these parameters should be chosen in an appropriate way. A

suitable choice of them can reduce the number of basis states necessary for a certain precision to a minimum, i.e. the basis can be optimized. Since the parameters B_2, B_3, C_2, C_3, d_2, d_3 and d_0 can vary independently in the non-coherent case, there are in principle two choices, namely a quadrupole and an octupole one for b and c. For the parameter b one has for example

$$b_{\text{quad}} = \frac{2B_2}{\hbar^2 d_2} \quad \text{or} \quad b_{\text{oct}} = \frac{2B_3}{\hbar^2 d_3}\,. \tag{4.7}$$

We have then chosen the arithmetic mean $b = (b_{\text{quad}} + b_{\text{oct}})/2$ which means that no degree of freedom is preferred and in case of coherence ($b_{\text{quad}} = b_{\text{oct}}$) the parameter is chosen as in the CQOM model. A similar choice was done for the parameter c. The parameter d_0 can simply be taken over from the CQOM solution.

Then the integrals of the Hamiltonian matrix are calculated. As a first step, the Hamiltonian (2.35) has to be transformed to the ellipsoidal coordinates, equation (2.36), see also equation (11) in [16] for the kinetic part. The matrix elements depend on the parameters B_2, B_3, C_2, C_3, d_2, d_3 and d_0 of this Hamiltonian. The integration is over the right half-plane only. The matrix elements for a fixed angular momentum are given by

$$\begin{aligned} &\langle n'\,k'|H|n\,k\rangle_I = \\ &\frac{d}{\sqrt{d_2 d_3}} \int_{-\pi/2}^{\pi/2} \int_0^{\infty} \psi^I_{n',k'}(\eta)\varphi_{k'}(\phi) H(\eta,\phi) \psi^I_{n,k}(\eta)\varphi_k(\phi)\eta d\eta d\phi\,, \end{aligned} \tag{4.8}$$

where the parity of the angular functions $\varphi_k^{\pm}$ is fixed by the quantum number k (odd or even). Since the integration is performed in the coordinates η and ϕ, the Jacobian from the transformation (2.36), $J(\eta) = \frac{d}{\sqrt{d_2 d_3}}\eta$, appears in the matrix elements (4.8). Then the integrations over the "radial" coordinate η are always reduced to the following known analytic expression [76]

$$\begin{aligned} \int_0^{\infty} t^{\alpha-1} e^{-pt} L_m^{\lambda}(pt) L_n^{\beta}(pt) dt = &\frac{p^{-\alpha}\Gamma(\alpha)\Gamma(n-\alpha+\beta+1)\Gamma(m+\lambda+1)}{m!n!\Gamma(1-\alpha+\beta)\Gamma(\lambda+1)} \\ &\times {}_3F_2(-m,\alpha,\alpha-\beta;-n+\alpha-\beta,\lambda+1;1)\,, \end{aligned} \tag{4.9}$$

which is fastly evaluated. The ϕ-integrations only involve trigonometric functions and are easily performed.

In order to obtain a two-dimensional matrix instead of the four component tensor, equation (4.8), the basis functions are relabeled into a list with only one index. For a fixed angular momentum I the resulting matrix is diagonalized and we obtain the eigenvalues and eigenvectors. The corresponding physical state from the yrast band is determined by the lowest eigenvalue whose eigenvector possesses the correct parity $(-1)^I$. In this way the model spectrum is constructed.

In the CQOM the yrast states are characterized by the quantum numbers $(n,k) = (0,1)$ for even I and $(0,2)$ for odd I. In the non-coherent case n and k are no longer good

quantum numbers. Then the model eigenfunctions are characterized by their decomposition coefficients in the basis states. It was found that for a given eigenfunction the main decomposition component still corresponds to the quantum numbers of the respective state in the CQOM model. Other higher lying basis states are also mixed into the final eigenstate to a certain amount.

We can advantageously use the CQOM theory for transitions shown above to calculate the transition probabilities in the non-coherent case. Since the wave function is expanded with respect to the basis functions and for them the transition theory is known, we obtain for the non-coherent matrix elements the following double sum including known expansion coefficients:

$$\tilde{R}_\lambda(I_i \to I_f) = \sum_{n'k'} \sum_{n''k''} c^{I_f}_{n''k''} c^{I_i}_{n'k'} R_\lambda(n'\, k'\, I_i \to n''\, k''\, I_f)\,. \tag{4.10}$$

In order to calculate the non-coherent transitions one simply has to replace R_λ with $\tilde{R}_\lambda$ in the above expression (3.14).

We only take into account transition probabilities related to the yrast band. It has been found that the consideration of transitions is very important and necessary in order to obtain a set of model parameters which is uniquely determined. The reason for this is that one of the fitting parameters, c, only appears in the wave functions. Its value could be arbitrarily chosen in an approach without transition probabilities.

4.4. Application to selected nuclei

Once the diagonalizations have been performed for all angular momenta, one obtains an yrast spectrum and is able to define a function σ_{RMS} which gives the root mean square deviation from the experimental levels. The transition probabilities are calculated from the above theory and we construct an overall root mean square deviation function including both energies and transitions. The transitions are included with weight factors providing the same order of magnitude for the fitting procedure.

Then the model parameters B_2, B_3, C_2, C_3, d_2, d_3, d_0 and e^1_{eff} can be adjusted so as to provide the best description of experimental data. As a first guess for the minimization we take the parameter values obtained from the CQOM model.

The model approach was applied to describe the yrast alternating parity spectra and yrast transitions of the nuclei ^{152,154}Sm, ^{154,156}Gd, ^{100}Mo and ^{236}U. The resulting optimal parameters are given in Table 4.1. It should be kept in mind that the fitting algorithm finds a local minimum and it eventually could be that there is another minimum which provides an even better description.

Table 4.1.: Parameters of the fits obtained for ^{152,154}Sm, ^{154,156}Gd, ^{100}Mo and ^{236}U. The parameters B_2, B_3 are given in units of $\hbar^2$/MeV, C_2 and C_3 are given in units of MeV, d_2 and d_3 are given in $\hbar^2 \cdot \mathrm{MeV}^{-1}$, d_0 is given in $\hbar^2$ and e^1_{eff} is in units of elementary charge.

Nucleus	B_2	B_3	C_2	C_3	d_2	d_3	d_0	e^1_{eff}
^{152}Sm	26.0	334.9	68.8	368.5	836.9	3886.7	24.3	1.43
^{154}Sm	2.9	339.0	111.2	2443.0	330.4	12264.9	325.8	1.64
^{154}Gd	7.5	172.5	85.8	482.7	486.7	4190.8	70.8	1.88
^{156}Gd	6.2	337.9	193.3	1257.6	954.7	7395.0	153.9	0.95
^{100}Mo	0.437	16.9	11379.9	87.6	682.2	577.5	18.9	0.56
^{236}U	186.7	185.6	44.9	619.5	549.8	11475.9	258.2	0.27

Table 4.2.: Quadrupole deformations obtained from the wave functions for ^{152,154}Sm, ^{154,156}Gd, ^{100}Mo and ^{236}U. The experimental values are taken from RIPL-2 [80].

Nucleus	β_2^{exp}	β_2^{theo}
^{152}Sm	0.3064	0.191
^{154}Sm	0.3410	0.318
^{154}Gd	0.3120	0.250
^{156}Gd	0.3378	0.217
^{100}Mo	0.2309	0.135
^{236}U	0.2821	0.272

We also calculate the corresponding wave functions for zero angular momentum and the resulting quadrupole deformation expectation values given by

$$\langle \beta_2 \rangle = \int_{-\infty}^{\infty} \int_{0}^{\infty} \beta_2 \Phi(\beta_2, \beta_3)^2 d\beta_2 d\beta_3 \,. \tag{4.11}$$

The wave functions are plotted in Figures 4.1-4.6 and the obtained quadrupole deformations are given in Table 4.2.

4.5. Discussion of the results

Compared to the CQOM case, the non-coherent approach leads to a better description of the yrast spectra of all nuclei under consideration. Roughly speaking the root mean square deviation from theory to experiment is improved by a factor of 2.

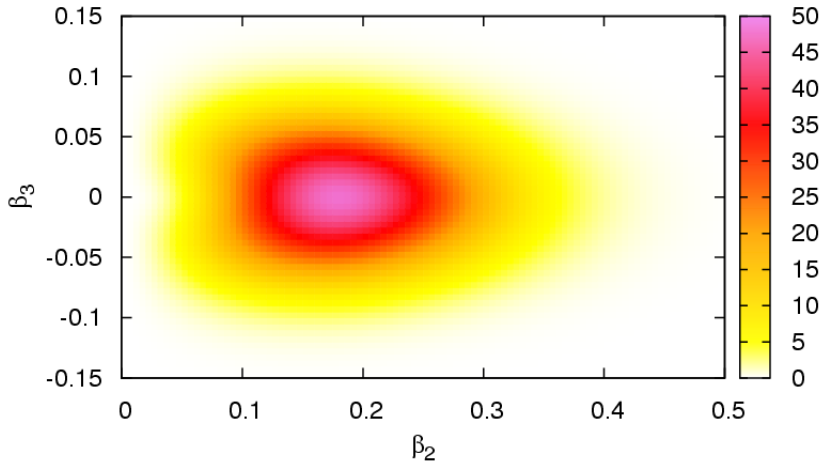

Figure 4.1.: Wave function for ^{152}Sm at angular momentum $I = 0$.

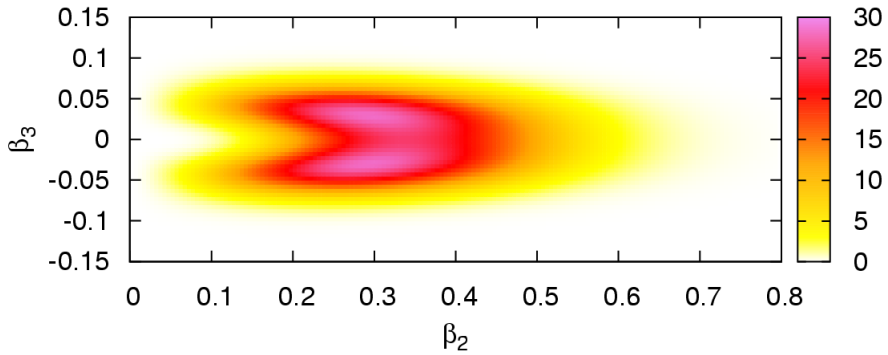

Figure 4.2.: Wave function for ^{154}Sm at angular momentum $I = 0$.

This is in agreement with our expectation since the numerical solution is a generalization and contains the analytical solution as a special case. The restriction to equal frequencies ω_2 and ω_3 is equivalent to certain relations between the model parameters (mass-, stiffness- and inertia parameters) which must hold. The non-coherent approach does not have these limitations and therefore consists of model parameters which are all allowed to vary freely. This is further discussed in [81] where the reader can also find detailed tables with energy level numbers.

Instead of discussing this obvious result, I would like to focus on a non-obvious result. What can be seen from Table 4.2 is that – without fitting these quantities(!) – the quadrupole deformation expectation values calculated from the wave functions are obtained reasonably and they even seem to reproduce the behaviour given by the experiment for the different nuclei, especially the least deformed nucleus in the experiment is also least deformed in the theory and the same holds for the most deformed nucleus. Since these numbers are not fitted, they can be seen as a true model prediction.

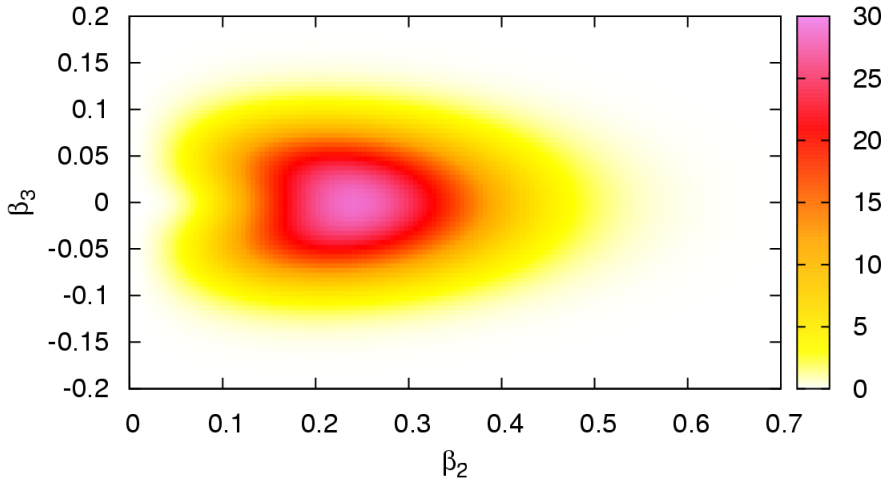

Figure 4.3.: Wave function for ^{154}Gd at angular momentum $I = 0$.

4.6. Outlook: non-axial deformations

The aim to generalize the Schrödinger equation to the case of arbitrary quadrupole and octupole deformations, which means non-zero a_{22}, a_{31} and a_{32} values for example, is of large interest. For example the TetraNuc (short for Tetrahedral Nuclei) project aims to get more insight about possible tetrahedral deformations of nuclei, associated with the a_{32} deformation variable, and the resulting implications. Possible candidates for such deformations are for example the nuclei ^{156}Gd and ^{156}Dy. The dimensionality of the problem grows with each deformation, making it a difficult multi-dimensional problem.

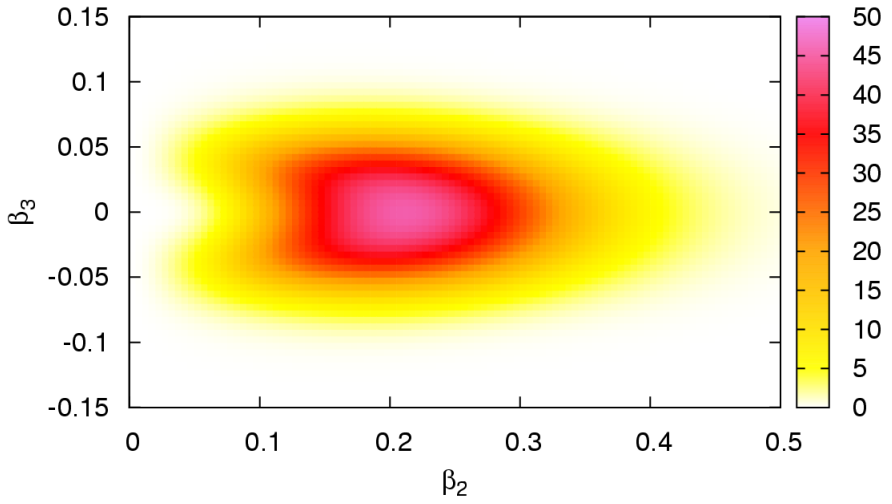

Figure 4.4.: Wave function for ^{156}Gd at angular momentum $I = 0$.

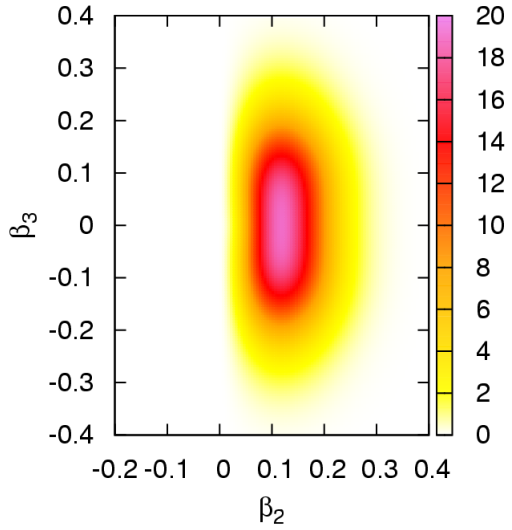

Figure 4.5.: Wave function for ^{100}Mo at angular momentum $I = 0$.

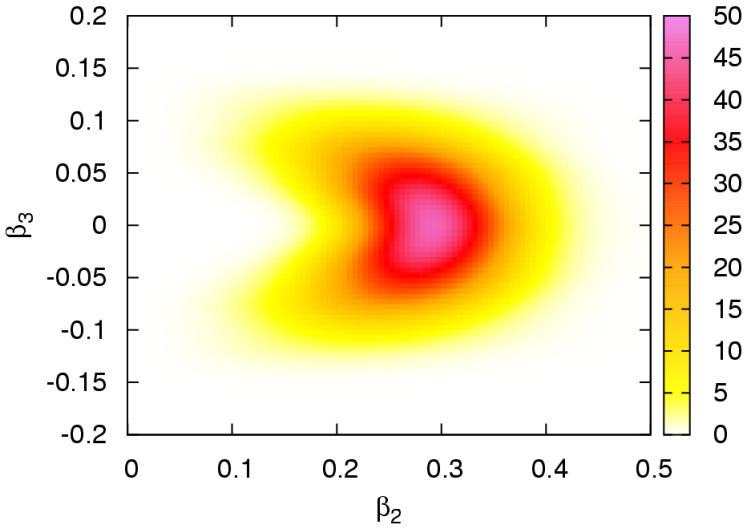

Figure 4.6.: Wave function for ^{236}U at angular momentum $I = 0$.

5. The used single-particle model

5.1. Introduction

So far we were only concerned with collective calculations. This chapter is about the deformed shell model which is used for further calculations. There should of course be a self-consistency between nucleonic degrees of freedom and collective properties.

For example, the Coriolis decoupling factor a appeared from the rotational Hamiltonian and entered the energy formula (2.48) only phenomenologically in the sense of an adjustable parameter. In chapter 6 we will put the calculation of this parameter on a microscopic basis, calculating matrix elements with single-particle wave functions according to the definition of the Coriolis decoupling factor.

In chapter 7 we use the single-particle states also as the starting point for deformed RPA calculations.

Details about the corresponding single-particle Fortran program published in Computer Physics Communications are given in [26]. The program solves the Schrödinger equation for the single-particle Hamiltonian

$$\hat{H}_{\text{sp}} = \hat{T}_{\text{kin}} + V_{\text{Woods-Saxon}} + V_{\text{Coul}} \tag{5.1}$$

numerically with an axially-deformed Woods-Saxon potential. The different parts of this Hamiltonian are explained in the following sections.

5.2. Average nuclear potential

5.2.1. Nuclear shape parameterization

The nuclear shape is assumed to be only axially deformed. Then, using the most general ansatz with an expansion into spherical harmonics, the expansion can be reduced to

spherical harmonics of the type $Y_{\lambda 0}(\cos\theta)$ and yields

$$R(\cos\theta, \hat{\beta}) = c(\hat{\beta}) R_0 \left[1 + \sum_{\lambda \geq 2} \beta_\lambda Y_{\lambda 0}(\cos\theta) \right] \tag{5.2}$$

for the radius. $\hat{\beta}$ is a short notation for a set of β_λ which determines the nuclear shape. The factor $c(\hat{\beta})$ is responsible for an overall scaling in such a way that the *constant volume condition* is fulfilled.

Moreover, a center of mass transformation is performed in such a way that the center lies in the coordinate origin. In case of axial deformations this obviously corresponds to a shift along the z-axis which should be chosen in such a way that it aligns with the symmetry axis of the nucleus.

5.2.2. Deformed Woods-Saxon potential

The deformed Woods-Saxon potential is defined as

$$V(\mathbf{r}, \hat{\beta}) = \frac{V_0}{1 + \exp\left[\mathrm{dist}_\Sigma(\mathbf{r}, \hat{\beta})/a \right]}, \tag{5.3}$$

where dist_Σ is the distance function between the point $\mathbf{r}$ and the nuclear surface as defined by (5.2). The parameter V_0 gives the depth of the potential and a is the diffuseness parameters which characterizes how much the potential is smeared out. The calculation of the distance can only be done numerically in a minimization procedure.

5.2.3. Spin-orbit potential

For the definition of the spin-orbit potential usually the most general scalar expression which can be constructed from the gradient of the potential, the spin and the linear momentum and which is only containing the first power of $\mathbf{p}$ is used.

This means

$$V_{\mathrm{so}} = \lambda \left(\frac{\hbar}{2Mc} \right) \left\{ \nabla \frac{V_0}{1 + \exp\left[\mathrm{dist}_\Sigma(\mathbf{r}, \hat{\beta})/a \right]} \right\} (\boldsymbol{\sigma} \times \mathbf{p}), \tag{5.4}$$

where λ is a strength parameter and M is the mass of a nucleon. The last bracket contains the cross product of the operator $\boldsymbol{\sigma}$ which is composed of Pauli matrices, and $\mathbf{p}$ is the linear momentum operator.

5.2.4. Coulomb potential

For the Coulomb potential a uniform charge distribution of the $Z-1$ protons in the core is assumed. For cylindrical coordinates it can be computed using the expression [40]

$$V_{\text{coul}} = \rho_e \int_{z_1}^{z_2} \left\{ \left[\rho_\Sigma^2 - \rho^2 - (z'-z)^2 - (z'-z)\frac{\partial \rho_\Sigma^2}{\partial z'} \right] F(a,b) + E(a,b) \right\} , \tag{5.5}$$

where $\rho_\Sigma(z)$ denotes a value of ρ for a point on the surface with coordinate z, ρ_e as a constant charge density, as well as

$$F(a,b) = a^{-1} \int_0^{\pi/2} d\phi \left(1 - \frac{a^2-b^2}{a^2} \sin^2\phi \right)^{-1/2} \tag{5.6}$$

$$E(a,b) = a \int_0^{\pi/2} d\phi \left(1 - \frac{a^2-b^2}{a^2} \sin^2\phi \right)^{1/2} \tag{5.7}$$

with $a^2 = (z'-z)^2 + (\rho'+\rho)^2$ and $b^2 = (z'-z)^2 + (\rho'-\rho)^2$.

5.3. Method of solution

5.3.1. Axially deformed harmonic oscillator basis

The eigenfunctions of the axially symmetric harmonic oscillator in cylindrical coordinates are

$$|n_\rho\, n_z\, \Lambda\, \Sigma\rangle = \psi_{n_\rho}^{\Lambda}(\rho)\psi_{n_z}(z)\psi_\Lambda(\phi)\chi(\Sigma) , \tag{5.8}$$

where $\Sigma = \pm\frac{1}{2}$ and Λ is the projection of the orbital angular momentum on the symmetry axis. Further written out we have

$$\psi_\Lambda(\phi) = \frac{1}{\sqrt{2\pi}} e^{i\Lambda\phi} \tag{5.9}$$

$$\psi_{n_z}(z) = \frac{1}{\sqrt{\sqrt{\pi} 2^{n_z} n_z!}} \left(\frac{M\omega_z}{\hbar} \right)^{1/4} e^{-\xi^2/2} H_{n_z}(\xi) \tag{5.10}$$

$$\psi_{n_\rho}^{\Lambda}(\rho) = \frac{\sqrt{n_\rho!}}{\sqrt{(n_\rho+|\Lambda|)!}} \left(\frac{M\omega_\perp}{\hbar} \right)^{|\Lambda|/2} \eta^{\frac{1}{2}|\Lambda|} e^{-\frac{1}{2}\eta} L_{n_\rho}^{|\Lambda|}(\eta) \tag{5.11}$$

$$\chi\left(\frac{1}{2}\right) = \begin{pmatrix} 1 \\ 0 \end{pmatrix} , \qquad \chi\left(-\frac{1}{2}\right) = \begin{pmatrix} 0 \\ 1 \end{pmatrix} , \tag{5.12}$$

using Hermite polynomials $H_n(\xi)$ and generalized Laguerre polynomials $L_n^\Lambda(\eta)$ in the dimensionless coordinates

$$\eta = \frac{M\omega_\perp}{\hbar}\rho^2 , \qquad \xi = \sqrt{\frac{M\omega_z}{\hbar}} z , \qquad \rho^2 \equiv x^2 + y^2 . \tag{5.13}$$

The energies are known to be

$$E_{n_\rho,n_z,\Lambda} = \left(n_z + \frac{1}{2}\right)\hbar\omega_z + (n_\perp + 1)\hbar\omega_\perp \tag{5.14}$$

with the main quantum number

$$N = n_z + n_\perp \tag{5.15}$$

and

$$n_\perp = 2n_\rho + |\Lambda| \,. \tag{5.16}$$

This allows an easy transition between the notation of (5.8) and $|N\, n_z\, \Lambda\, \Sigma\rangle$.

5.3.2. Basis optimization

The program uses some techniques to optimize the basis. The most important point is to have good approximations for the oscillator frequencies ω_z and $\omega_\perp$. In case of a spherical oscillator

$$\hbar\omega_0 \approx 1.2\left(\frac{41}{A^{1/3}}\right)\ \text{MeV} \tag{5.17}$$

is a good approximation for its frequency ω_0. The program uses this together with the "volume conservation" condition

$$\omega_\perp^2\omega_z = \omega_0^3 \tag{5.18}$$

and another deformation of the potential "match condition".

Secondly, it is possible to give an energy limit $E_{\max}$ which leads to an exclusion of those basis states lying very high in energy. In this way only the more important states with

$$E_{n_\rho,n_z,\Lambda} < E_{\max} \tag{5.19}$$

are contributing.

5.3.3. Matrix elements of the Hamiltonian

The total Woods-Saxon single-particle Hamiltonian reads

$$H_{\text{WS}} = T + V + V_{\text{so}} + \frac{1}{2}(1 + \tau_3)V_{\text{c}} \,. \tag{5.20}$$

The corresponding matrix elements can be found in appendix A.3. In order to reduce the necessary calculation costs one can make use of the symmetries of this Hamiltonian,

namely time reversal symmetry and axial symmetry. The first leads to two-fold degenerate levels, the so-called *Kramer's degeneracy*, while the latter implies that the projection of the single-particle angular momentum on the symmetry axis

$$\Omega \equiv \Lambda + \Sigma \tag{5.21}$$

is a constant of the motion. This leads to the fact that the eigenstates do not depend on the sign of Ω and it is enough to consider only positive Ω values for the calculation of matrix elements.

Further, as can be shown by using the relation

$$H_{n+1}(\xi) = 2\xi H_n(\xi) - 2nH_{n-1}(\xi) \tag{5.22}$$

for the Hermite polynomials, the matrix elements of the potential term satisfy the recurrence relation

$$\langle n_z'|V|n_z\rangle = \sqrt{\frac{n_z'+1}{n_z}}\langle n_z'+1|V|n_z-1\rangle + \sqrt{\frac{n_z'}{n_z}}\langle n_z'-1|V|n_z-1\rangle - \sqrt{\frac{n_z-1}{n_z}}\langle n_z'|V|n_z-2\rangle\,. \tag{5.23}$$

5.4. Test of the program

Since the calculations based on this single-particle program rely on its correctness, extended checks have been performed.

This considers first and foremost the calculation of matrix elements of the different parts of the single-particle Hamiltonian. It was checked that numerical results obtained with Mathematica's `NIntegrate` command were identical to the matrix elements extracted from the deformed-shell model Fortran program.

The analytical formulas for the matrix elements were checked additionally. They are given in detail in [67]. As a result it was found that the matrix elements for the kinetic energy were given correctly while those for the Woods-Saxon potential were wrong by a factor of 1/2 which was easily detected. The most difficult derivation has to be done for matrix elements of the spin-orbit part of the Hamiltonian. Due to an inconsistency which could not be resolved, I have rederived these matrix elements and found that in [67] a pair of parenthesis is missing.

For reasons of completeness and as a helpful reference to repeat numerical checks or as a starting point for programming all matrix elements are given in appendix A.3.

Furthermore the single-particle spectrum of ^{208}Pb was calculated with a spherical shell model using the same Woods-Saxon parameters. The levels have been compared to the

deformed shell model in case of zero deformation, i.e. $\beta_\lambda = 0$. ^{208}Pb is a good test nucleus since the level scheme of it can also be found in various textbooks, e.g. in [48]. Because of its double magicity the nucleus can be considered to be more or less spherical.

Calculations for spherical nuclei were furthermore compared to results obtained independently [41]. The agreement is quite good but not perfect, which should be due to slightly different parameter values used in the calculations.

In conclusion it can be said that the single-particle program is thoroughly tested and that we can rely on its results for the further calculations.

6. Connection of intrinsic and collective motion

6.1. Introduction

This chapter treats odd-mass nuclei which are quadrupole-octupole deformed and in which the coupling of the collective rotations and vibrations to the single-particle motion of the unpaired nucleon provides a split parity-doublet structure of the spectrum [28, 54]. There exist various model approaches to explain this structure [55, 56, 57, 58, 59, 61, 65]. In the case of angular momentum projection $K = 1/2$ one also observes the Coriolis interaction between the odd particle and the rotating even-even core.

We assume a strong coupling between the core and the odd nucleon. In case of a weak coupling the odd nucleon does not "feel" the reflection-asymmetric shape of the nucleus and thus the single-particle motion is characterized with a fixed good parity. In case of a strong coupling the shape of the nucleus is much more imprinted on the single-particle potential [56]. Although the single-particle states are now without a good parity the coupling to the core is such that the total state of the nucleus remains with a good parity.

We examine the effects of the parity-mixing in the single-particle state on the total behaviour of the system. The parity mixing makes it necessary to modify the standard definition for the Coriolis decoupling factor, given by the matrix element of the single-particle angular momentum operator $\hat{j}_+$ in the single-particle states with $K = \pm 1/2$ [28].

The behaviour of the parity mixing and its effect on the Coriolis interaction is studied in dependence of the quadrupole and octupole deformations β_2 and β_3.

6.2. Core plus particle Hamiltonian

We consider a Hamiltonian for a vibrating and rotating nuclear system with quadrupole-octupole degrees of freedom. It can be written in the form

$$H = H_{\rm qoc}^{\rm coll} + H_{\rm sp} + H_{\rm coriol}\,, \tag{6.1}$$

where $H_{\rm qoc}^{\rm coll}$ corresponds to the collective quadrupole-octupole vibration and rotation of the system, $H_{\rm sp}$ describes the motion of the odd particle (neutron or proton) in the field of the even-even core, while $H_{\rm coriol}$ represents the Coriolis interaction between the core and the particle. The collective plus centrifugal Hamiltonian can be written in the form [58]

$$H_{\rm qoc}^{\rm coll} + H_{\rm coriol} = -\frac{\hbar^2}{2B_2}\frac{\partial^2}{\partial\beta_2^2} - \frac{\hbar^2}{2B_3}\frac{\partial^2}{\partial\beta_3^2} + \frac{1}{2}C_2\beta_2^2 + \frac{1}{2}C_3\beta_3^2 + \frac{\hat{I}^2 - \hat{I}_z^2 + \hat{I}_+\hat{j}_- - \hat{I}_-\hat{j}_+}{2(d_2\beta_2^2 + d_3\beta_3^2)}\,, \tag{6.2}$$

with mass, stiffness and inertial parameters B_2, B_3, C_2, C_3 and d_2, d_3, total angular momentum operators $\hat{I}_\pm = \hat{I}_x \pm i\hat{I}_y$ and spherical components $\hat{j}_\pm = \hat{j}_x \pm i\hat{j}_y$ of the total intrinsic particle angular momentum $\hat{j}$, respectively. The resulting quadrupole-octupole vibrational wave function which we denote by $\Phi_{\rm core}^{\pm}$ has a well defined parity $\pi_c = (\pm)$.

The single-particle Hamiltonian is considered in the form as presented in chapter 5 of this work. The solution of this Hamiltonian is obtained by diagonalization using of the axially deformed harmonic oscillator (ADHO) basis. This implies that the wave function of the odd particle is obtained as an expansion in the ADHO basis functions

$$\mathcal{F}_\Omega = \sum_{N n_z \Lambda} C^{\Omega}_{N n_z \Lambda} |N\, n_z\, \Lambda\, \Omega\rangle\,. \tag{6.3}$$

In the special case of quadrupole deformation only ($\beta_3 = 0$), the reflection-symmetric case, the single-particle wave function $\mathcal{F}_\Omega$ corresponds to a single-particle state with good parity, either $\pi_{\rm sp} = (+)$ or $(-)$. The reflection-asymmetric case with $\beta_3 \neq 0$ belongs to a mixed-parity state without determined parity.

The parity of the basis states $|N\, n_z\, \Lambda\, \Omega\rangle$ is given by $(-1)^N$. This makes it possible to separate the expansion in terms of the basis functions in two sums, containing only terms with positive or negative parity. Hence we can write

$$\mathcal{F}_\Omega = \sum_{\pi_{\rm sp}=\pm 1} \mathcal{F}_\Omega^{(\pi_{\rm sp})} = \mathcal{F}_\Omega^{(+)} + \mathcal{F}_\Omega^{(-)}\,, \tag{6.4}$$

where $\mathcal{F}_\Omega^{(+)}$ contains only the positive parity components, while $\mathcal{F}_\Omega^{(-)}$ contains the negative ones with

$$\hat{\pi}_{\rm sp}\mathcal{F}_\Omega^{(\pm)} = \pm\mathcal{F}_\Omega^{(\pm)}\,. \tag{6.5}$$

The action of the parity operator $\hat{\pi}_{\rm sp}$ on the function $\mathcal{F}_\Omega$ gives

$$\hat{\pi}_{\rm sp}\mathcal{F}_\Omega = \mathcal{F}_\Omega^{(+)} - \mathcal{F}_\Omega^{(-)} \tag{6.6}$$

and we can characterize the parity mixing of a given single-particle state by the expectation value of the parity operator in this state

$$\begin{aligned}\langle\hat{\pi}_{\rm sp}\rangle &= \langle\mathcal{F}_\Omega|\hat{\pi}_{\rm sp}|\mathcal{F}_\Omega\rangle \\ &= \sum_{Nn_z\Lambda}\sum_{N'n'_z\Lambda'} C^{\Omega *}_{N'n'_z\Lambda'} C^{\Omega}_{Nn_z\Lambda}\langle N\, n_z\, \Lambda\, \Omega|\hat{\pi}_{\rm sp}|N'\, n'_z\, \Lambda'\, \Omega\rangle \\ &= \sum_{Nn_z\Lambda}(-1)^N |C^{\Omega}_{Nn_z\Lambda}|^2\,.\end{aligned} \tag{6.7}$$

6.3. Total particle-core wave function

With the choices (6.2) and (5.1) for the collective and single-particle parts of the Hamiltonian (6.1), the total wave function can be given in a symmetrized form providing a good total parity π and $\mathcal{R}_1$ invariance of the system. We write for the total wave function

$$\Psi^\pi_{IMK} = \frac{1}{2}\mathcal{N}(1+\mathcal{R}_1)D^I_{MK}(\theta)(1+\pi\hat{P})\Phi^{\pi_c}_{\rm core}\mathcal{F}_K\,, \tag{6.8}$$

with a rotation function $D^I_{MK}(\theta)$ depending on the Euler angles and with a normalization factor $\mathcal{N}$.

The operator $\hat{P}$ is the operator of the total parity of the system and gives π as eigenvalue. It can be written as product

$$\hat{P} = \hat{\pi}_c \cdot \hat{\pi}_{\rm sp} \tag{6.9}$$

of the core and single-particle operators $\hat{\pi}_c$ and $\hat{\pi}_{\rm sp}$, respectively.

The operator $\hat{R}_1$ acts as a rotation by an angle π about an axis perpendicular to the intrinsic z-axis and acts of the different parts of (6.8) as follows

$$\mathcal{R}_1 D^I_{MK} = (-1)^{I-K} D^I_{M-K} \tag{6.10}$$

$$\mathcal{R}_1 \Phi^{\pi_c}_{\rm core} = \hat{\pi}_c \Phi^{\pi_c}_{\rm core} = \pi_c \Phi^{\pi_c}_{\rm core} \tag{6.11}$$

$$\mathcal{R}_1 \mathcal{F}_K = \mathcal{F}_{-K}\,. \tag{6.12}$$

The core wave function $\Phi^{\pi_c}_{\rm core}$ is characterized by a good core parity π_c which we fix so as to obtain $\pi_c = (+)$ for the split doublet counterparts containing the ground state (states shifted down), and $\pi_c = (-)$ for the states shifted up.

The single-particle wave function $\mathcal{F}_K$ is a mixture of two parts $\mathcal{F}^{(\pm)}_K$ with opposite parities. Then the operators $1 - \pi\hat{P}$ projects out the positive or negative component,

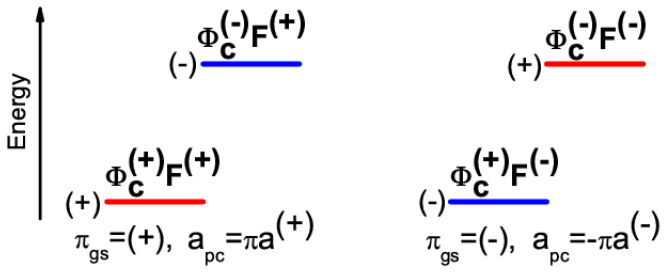

Figure 6.1.: Particle-core states coupling for split parity-doublets with positive (left part) and negative (right side) ground-state parity. The respective expressions for the decoupling factor $a_{\mathrm{pc}} = \pm\pi a^{(\pm)}$ are also given.

$\mathcal{F}_K^{(+)}$ or $\mathcal{F}_K^{(-)}$, from $\mathcal{F}_K$ and thus provides a good total parity of the states in the split parity-doublet spectrum.

Assuming that the gound state (the lowest state of the doublet) has a positive parity, the projected component is $\mathcal{F}_K^{(+)}$. If the ground state has negative parity then the projected component is $\mathcal{F}_K^{(-)}$. These two possible situations are illustrated in Figure 6.1.

As explained in more detail in [24], this projection does not represent the exact solution of the single-particle Schrödinger equation, but can be seen as an approximation which is valid in certain physical limits. The mechanism corresponds to an effective restoration of the parity invariance of the total Hamiltonian (6.1) which is originally broken because of the presence of the reflection asymmetric single-particle Hamiltonian (5.1). It is clear that this procedure is justified more and more as the missing part of the wave function becomes smaller. The criterion should be that the expectation value of the single-particle parity should be closer to the favoured parity rather than to the unfavoured one. This is also very important for determining the physically reasonable regions of quadrupole-octupole deformations in a given nucleus.

6.4. Decoupling factor for parity-mixed single-particle states

In case of $K = 1/2$ the standard definition for the Coriolis decoupling factor is

$$a = \langle \mathcal{F}_{1/2} | \hat{j}_+ | \mathcal{F}_{-1/2} \rangle \,. \tag{6.13}$$

In the case of reflection asymmetry we need to modify this definition. The particle-core decoupling factor a_{pc} is determined through the matrix element

$$-\langle \Psi^{\pi}_{IM\frac{1}{2}} | \hat{I}_- \hat{j}_+ | \Psi^{\pi}_{IM\frac{1}{2}} \rangle = \mathcal{N}^2 (-1)^{I+\frac{1}{2}} \left(I + \frac{1}{2} \right) \cdot a_{\mathrm{pc}} \,. \tag{6.14}$$

Table 6.1.: Particular forms of the decoupling factor a_{pc} in dependence on the ground-state parity π_{gs} and the parity π of a given state in the split parity-doublet spectrum.

	$\pi = (+)$	$\pi = (-)$
$\pi_{\mathrm{gs}} = (+)$	$a_{\mathrm{pc}} = a^{(+)}$	$a_{\mathrm{pc}} = -a^{(+)}$
$\pi_{\mathrm{gs}} = (-)$	$a_{\mathrm{pc}} = -a^{(-)}$	$a_{\mathrm{pc}} = a^{(-)}$

From this we can obtain a_{pc} by means of the total wave function (6.8) and the transformation properties (6.10)-(6.12) and (6.6) in the form

$$\begin{aligned} a_{\mathrm{pc}} &= \frac{1}{2}\pi_c \left(\left\langle \mathcal{F}_{\frac{1}{2}} | \hat{j}_+ | \mathcal{F}_{-\frac{1}{2}} \right\rangle + \pi\pi_c \left\langle \hat{\pi}_{\mathrm{sp}} \mathcal{F}_{\frac{1}{2}} | \hat{j}_+ | \mathcal{F}_{-\frac{1}{2}} \right\rangle \right) \\ &= \frac{1}{2}\pi_c \left[(1 + \pi\pi_c) a^{(+)} + (1 - \pi\pi_c) a^{(-)} \right] , \end{aligned} \tag{6.15}$$

where

$$a^{(+)} = \langle \mathcal{F}^{(+)}_{1/2} | \hat{j}_+ | \mathcal{F}^{(+)}_{-1/2} \rangle \tag{6.16}$$

$$a^{(-)} = \langle \mathcal{F}^{(-)}_{1/2} | \hat{j}_+ | \mathcal{F}^{(-)}_{-1/2} \rangle , \tag{6.17}$$

with

$$\langle \mathcal{F}^{(+)}_{1/2} | \hat{j}_+ | \mathcal{F}^{(-)}_{-1/2} \rangle = \langle \mathcal{F}^{(-)}_{1/2} | \hat{j}_+ | \mathcal{F}^{(+)}_{-1/2} \rangle = 0 . \tag{6.18}$$

The factors $a^{(+)}$ and $a^{(-)}$ are projected matrix elements of the operator $\hat{j}_+$ in the subspaces of positive and negative parity components of the single-particle wave function, respectively. We can write this out further with expansion coefficients as

$$a^{(\pm)} = \sum_{N n_z \Lambda} \sum_{N' n'_z \Lambda'} C^{\frac{1}{2}*}_{N' n'_z \Lambda'} C^{\frac{1}{2}}_{N n_z \Lambda} \left\langle N'\, n'_z\, \Lambda' \frac{1}{2} | \hat{j}_+ | N\, n_z\, -\Lambda\, -\frac{1}{2} \right\rangle , \tag{6.19}$$

with N and N' being even or odd. This expression requires the calculation of matrix elements of $\hat{j}_+$ between ADHO basis states. This topic is treated in appendix A.5.

From equation (6.15) it is easy to derive that in a given state I^π of the split parity-doublet spectrum the decoupling factor a_{pc} is reduced to $\pi a^{(+)} = \pm a^{(+)}$ when the parity of the ground state π_{gs} is positive, $\pi_{\mathrm{gs}} = (+)$, and to $-\pi a^{(-)} = \mp a^{(-)}$ when the ground state parity is negative, $\pi_{\mathrm{gs}} = (-)$. Table 6.1 illustrates this fact.

In short this means that for a given state I^π in the parity-doublet

$$a_{\mathrm{pc}} = \pi\pi_{\mathrm{gs}} a^{(\pi_{\mathrm{gs}})} = \pm\pi a^{(\pm)} \tag{6.20}$$

holds. This makes it possible to obtain a correspondence between the values of the decoupling factor a_{qoc} fitted in the model of coherent quadrupole-octupole motion [58] and the values of the projected decoupling factors $a^{(\pm)}$ in the present scheme. From

$$a_{\mathrm{coll}} = \pi a_{\mathrm{qoc}} \leftrightarrow \pi\pi_{\mathrm{gs}} a^{(\pi_{\mathrm{gs}})} = \pm\pi a^{(\pm)} = a_{\mathrm{pc}} \tag{6.21}$$

it follows

$$a_{\mathrm{qoc}} \leftrightarrow \pi_{\mathrm{gs}} a^{(\pi_{\mathrm{gs}})} = \pm a^{(\pm)} \,. \tag{6.22}$$

As it should be, we reobtain the standard Coriolis decoupling factor in the limiting case $\beta_3 = 0$, namely $a^{(+)}$ when the downwards shifted sequence (containing the ground state) is with positive parity and $a^{(-)}$ when this is the negative parity sequence.

6.5. Numerical results and discussion

Here the results from [24] are presented and the following is cited from this paper.

The numerical behaviour of the average s.p. model parity $\langle\hat{\pi}_{\mathrm{sp}}\rangle$, Eq. (6.7), and of the parity-projected decoupling factor a_{pc}, Eq. (6.20), was examined as a function of the quadrupole and octupole deformations in several odd-mass nuclei. Numerical calculations were performed on a net in the two-dimensional space of the parameters β_2 and β_3. The physical relevance of the decoupling factor in the various regions in the (β_2, β_3)-plane was estimated by requiring that the dominant average parity in the given region has the sign of the parity established in the experimentally measured ground state of the nucleus.

In Fig. 6.2 the behaviour of the average s.p. model parity in the nuclei ^{237}U, and ^{249}Cm is shown (upper plots) as a function of the octupole deformation β_3 at β_2 corresponding to the experimentally estimated quadrupole deformations of the respective even-even core nuclei and (lower plots) as a two-dimensional function (contour plot) in the plane (β_2, β_3). From the upper plots it is seen that $\langle\hat{\pi}_{\mathrm{sp}}\rangle$ smoothly changes with the increasing of β_3. In ^{237}U the average parity starting by -1 at $\beta_3 = 0$ goes through the zero value at $\beta_3 \sim 0.15$ and further increases to $\langle\hat{\pi}_{\mathrm{sp}}\rangle = 0.3 - 0.4$. This is an important observation showing that a presence of a dominant parity is possible at large β_3 deformations. The same result is well seen in the contour plot for the average parity in ^{237}U in the lower left part of Fig. 6.2. It follows that the presently considered parity-projection coupling scheme should be applicable in wide ranges in the (β_2, β_3)-plane.

In ^{249}Cm $\langle\hat{\pi}_{\mathrm{sp}}\rangle$ smoothly approaches the zero value for $\beta_3 \sim 0.2$ indicating the presence of a deformation region with strong parity mixing. Nevertheless, similarly to ^{237}U, the two-dimensional contour plot (the lower right part of Fig. 6.2) shows that in the most regions in the (β_2, β_3)-plane the s.p. state is characterized with some dominant parity instead of becoming totally mixed ($\langle\hat{\pi}_{\mathrm{sp}}\rangle \sim 0$). Another important result is that in

the considered nuclei the s.p. wave functions appear strongly fragmented into various Nilsson orbitals with different parities. This is indicated in Fig. 6.2 (upper plots) where the contributions (in %) of the largest $[N, n_z, \Lambda]$ components of the wave function are given for certain β_3 deformations.

The behaviour of the quantity $a^{(+)}$ (which determines the decoupling factor $a_{\rm pc}$ in the cases of a ground state with $K = 1/2^+$) as a function of β_2 and β_3 in the nucleus ^{239}Pu is illustrated in Fig. 6.3. The left plot shows a two-dimensional surface containing the values of $a^{(+)}$ in the (β_2, β_3)-regions with $K = 1/2$. The right plot contains a contour which corresponds to the intersection of the two-dimensional surface with the plane determined by the decoupling parameter value $a_{\rm qoc} = -0.34$ fitted in the collective model [58]. This contour outlines deformation regions for which the microscopically calculated decoupling factor $a_{\rm pc}$ provides a reasonable description of the split parity-doublet structure, perturbed by the Coriolis interaction, of the experimental spectrum in ^{239}Pu. Two experimental guesses for the quadrupole deformation, $\beta_2 = 0.227$ (from a data base [80] for ^{239}Pu) and 0.286 (from the core nucleus ^{238}Pu [42]) and one for the octupole deformation, $\beta_3 = 0.091$ (also from ^{238}Pu [43]), are given in the right plot of Fig. 6.3. It is seen that the couple of ^{238}Pu core-deformations ($\beta_2 = 0.286, \beta_3 = 0.091$) lies exactly on the contour, while the value $\beta_2 = 0.227$ suggests a slightly larger octupole deformation $\beta_3 = 0.117$ for the odd-mass nucleus ^{239}Pu.

This result shows that various (β_2, β_3)-deformation sets provide consistency of the decoupling factor $a_{\rm pc}$ with the collective model factor $a_{\rm qoc} = -0.34$ outlining physically reasonable regions of quadrupole and octupole deformations in the considered nucleus. These regions can be further limited through the requirement for the dominant parity corresponding to the experimental ground-state parity. In Fig. 6.4 (left part) the (β_2, β_3)-contour corresponding to $a^{(+)} = a_{\rm qoc} = -0.34$ is mapped on the contour-plot for the average s.p. parity $\langle\hat{\pi}_{\rm sp}\rangle$, allowing one to see the dominant parity at a given set of deformations. In the right part of Fig. 6.4 the quantity $\langle\hat{\pi}_{\rm sp}\rangle$ is plotted as a function of β_2 at several fixed β_3- values in the deformation region of interest. Indeed, it is immediately seen that the couple of deformations $(\beta_2 = 0.227, \beta_3 = 0.117)$ lies in a region with positive dominant parity. More precisely one has $\langle\hat{\pi}_{\rm sp}\rangle \sim 0.58$ in that point, which is consistent with the experimentally established positive parity of the ground state of ^{239}Pu [72]. On the other hand the couple $(\beta_2 = 0.286, \beta_3 = 0.091)$ appears in a region with negative average parity ($\langle\hat{\pi}_{\rm sp}\rangle \sim -0.38$) which is inconsistent with the known ground state parity in ^{239}Pu. Thus the implemented analysis suggests that among the both considered deformation sets only the one $(\beta_2 = 0.227, \beta_3 = 0.117)$ has a reasonable physical meaning related to the Coriolis decoupling strength and the s.p. parity in the ground state. In the above aspect, from Fig. 6.4 it is seen that the part of the contour closed in the region from $(\beta_2 = 0.22, \beta_3 = 0.11)$ to $(\beta_2 = 0.27, \beta_3 = 0.14)$ with $\langle\hat{\pi}_{\rm sp}\rangle > 0$ provides physically reasonable quadrupole-octupole deformations for the nucleus ^{239}Pu.

Similar analysis can be done for other nuclei. In Fig. 6.5 plots for the average parity with contours for the decoupling factors are given for the nuclei ^{251}Cf and ^{219}Ac. In ^{251}Cf

two regions of consistency with the collective model [58] are obtained for the decoupling factor, but only one of them placed in the right down corner of the plot provides a positive dominant parity in correspondence to the experimental ground state parity. It is seen that this region suggests quite a large quadrupole deformation $\beta_2 \sim 0.42 - 0.45$ with reasonable values for the octupole deformation up to $\beta_3 = 0.1$. In ^{219}Ac the ground state is with negative parity. Therefore, here the considered decoupling factor is $-a^{(-)}$ with a negative dominant parity. The suggested region for the quadrupole-octupole deformations appears in the left down corner of the plot.

The so far presented considerations allow one to discuss a more complicated problem related to the estimation of the K-quantum number value on which the split parity-doublet in a given nucleus is built. As shown in Ref. [58] the collective model fit of the decoupling factor for the experimental spectrum of ^{223}Ra suggests a considerable manifestation of the Coriolis interaction and, therefore, a presence of a $K = 1/2$ value in the ground state of this nucleus. On the other hand the estimates given in the experimental databases suggest $K = 3/2$ [72]. The present deformed shell model calculations in the (β_2, β_3)-plane allow one to examine this problem in detail.

In Fig. 6.6 (left) a "map" of the ground-state K-values appearing in the various regions of the (β_2, β_3)-plane is given for ^{223}Ra. Indeed, it is seen that the regions with $K = 1/2$ are few, which explains why it is difficult to identify them if calculations are performed for a limited number of β_2 and β_3 values. On the other hand, the right plot in Fig. 6.6 shows that in the obtained $K = 1/2$-regions contours of consistency between the values of the decoupling factor $a^{(+)}$ and the collective decoupling parameter $a_{\rm qoc} = 0.12$ are well determined. This result strongly supports the suggestion about the presence of $K = 1/2$ with a considerable Coriolis interaction in the spectrum of ^{223}Ra [58]. Further, the examination of the dominant parity in the (β_2, β_3)-plane allows one to specify the physically reasonable deformation regions within the obtained contours of consistency with the collective model [58]. The average-parity plot for ^{223}Ra is shown in Fig. 6.7. It is immediately seen that the region with $\beta_2 \sim 0.2$ and $\beta_3 \sim 0.05$ has to be excluded from consideration since there the dominant parity $\langle \hat{\pi}_{\rm sp} \rangle$ is negative, while the experimental ground state parity for ^{223}Ra [72] is obtained positive. Then, one finds two other regions in the upper right part of the plot where the dominant parity is already positive, $\langle \hat{\pi}_{\rm sp} \rangle > 0$. Based on this result one can suggest that the physically reasonable quadrupole-octupole deformations of ^{223}Ra are located in the region of $\beta_2 \sim 0.3$ and $\beta_3 \sim 0.15 - 0.2$. The above result provides an argument for a revision of the value $K = 3/2$ assigned to the ground state of ^{223}Ra in experimental data bases. Also, the presently obtained result suggests a revision of the deformation values proposed for the same nucleus in a previous work [22], where the region $(\beta_2 \sim 0.2, \beta_3 \sim 0.05)$ was misconsidered due to the lack of a dominant-parity analysis. Also, one should recognize that the presently obtained (β_2, β_3)-deformation region for ^{223}Ra is still rather wide. Further detailed analysis, especially through a consistent application of the deformed shell model and the collective model, could provide a more precise result.

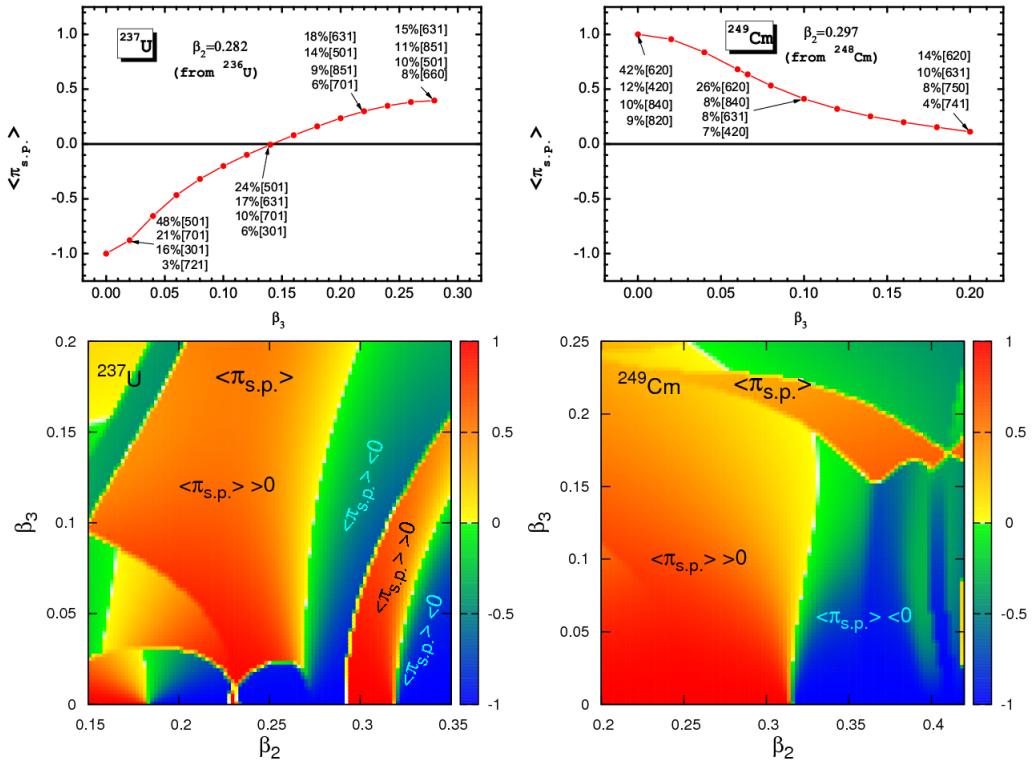

Figure 6.2.: Average s.p. model parity in ^{237}U and ^{249}Cm as a function of β_3 at fixed β_2-values (upper plots) and as a two-dimensional function (lower plots) in the plane (β_2, β_3). The light contours in the two-dimensional plots correspond to a strong s.p. parity mixing, $\langle\hat{\pi}_{\mathrm{sp}}\rangle \sim 0$, while the others correspond to some $(+)$ or $(-)$ dominant parity.

6.6. Outlook: Averaging the single-particle Woods-Saxon potential

The assumption that the collective potential influences the behaviour of the single-particle wave function while the opposite is much less the case seems to be reasonable if a single nucleon is attached in addition to a deformed core nucleus. As suggested by P. Yotov, using this approximation, one could reduce the five-dimensional problem of the Hamiltonian $\hat{H}_{\mathrm{coll}} + \hat{H}_{\mathrm{s.p.}}$ (two deformations from the collective part and three coordinates for the single-particle part) to a three-dimensional one.

In order to do this, one could calculate the expectation value of the single-particle Woods-Saxon potential with respect to the already obtained collective states $\Phi(\beta_2, \beta_3)$ which are then so to say weighting factors in the calculation of the following average value:

$$V(\mathbf{r}) = \int_0^\infty \int_{-\infty}^\infty \Phi^*(\beta_2, \beta_3) V_{\mathrm{WS}}(\beta_2, \beta_3, \mathbf{r}) \Phi(\beta_2, \beta_3) d\beta_2 d\beta_3 \tag{6.23}$$

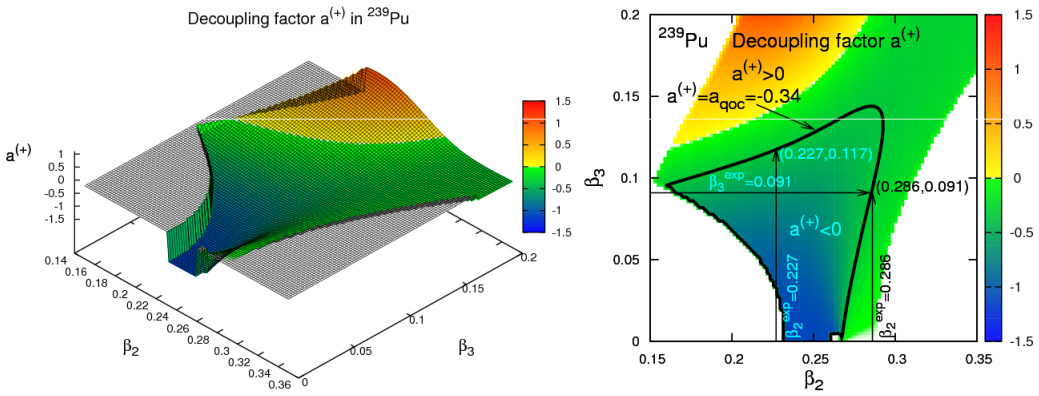

Figure 6.3.: The projected decoupling factor $a^{(+)}$ in ^{239}Pu as a function of β_2 and β_3. The flat areas at $a^{(+)} = 0$ in the left plot and the white areas in the contour plot (right) correspond to $K \neq 1/2$.

The total Hamiltonian to treat is $\hat{H}_{\text{tot}} = \hat{H}_{\text{coll}} + \hat{H}_{\text{sp}}$ and we can make a separation ansatz for the solution wave function of $\hat{H}_{\text{tot}}$.

The idea is now to use the potential $V(\mathbf{r})$ obtained in (6.23) for the treatment of the single-particle problem. The remaining task is therefore the solution of the three-dimensional Schrödinger equation. In order to compare the results to the output of the single-particle program by Cwiok et al. [26], it is a good idea to solve the Schrödinger equation by means of diagonalization with a $|n_\rho\, n_z\, \Lambda\, \Sigma\rangle$-basis in cylindrical coordinates.

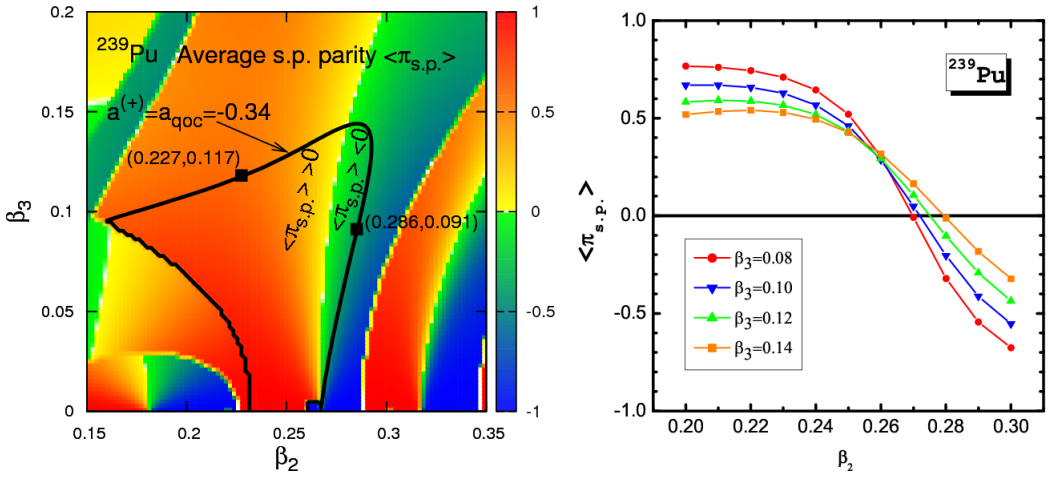

Figure 6.4.: Average s.p. model parity in ^{239}Pu: (left plot) as a two-dimensional function in the plane (β_2, β_3) together with the contour $a^{(+)} = a_{\rm qoc} = -0.34$ from Fig 6.3; (right plot) as a function of β_2 at several fixed β_3-values.

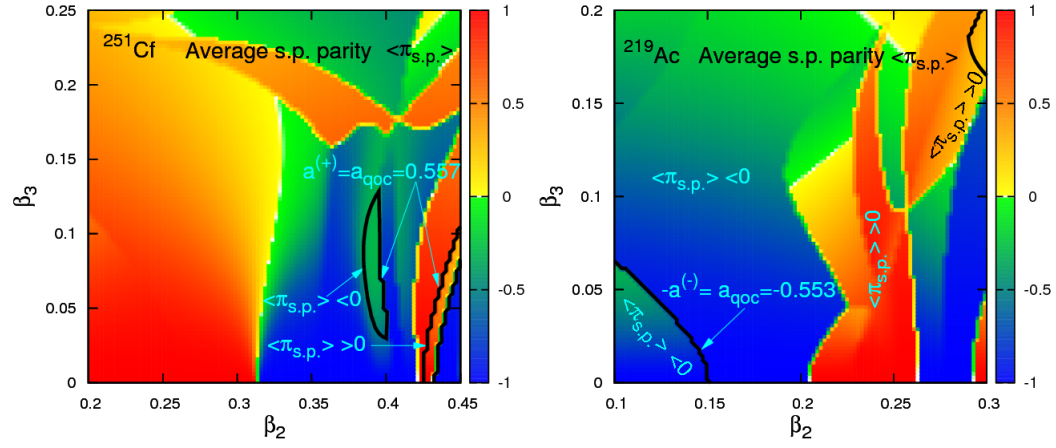

Figure 6.5.: The same as in Fig. 6.4 (left), but for the nuclei ^{251}Cf and ^{219}Ac.

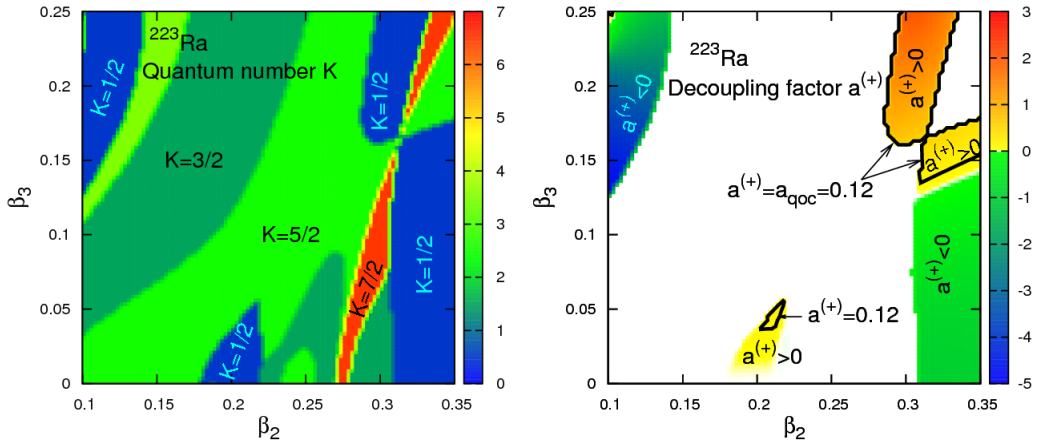

Figure 6.6.: Contour plot showing the different K-regions (left) and the projected decoupling factor $a^{(+)}$ (right) as a function of β_2 and β_3 in ^{223}Ra. The black contour at $a^{(+)} = 0.12$ (right) corresponds to a decoupling parameter value fitted in the collective model [58].

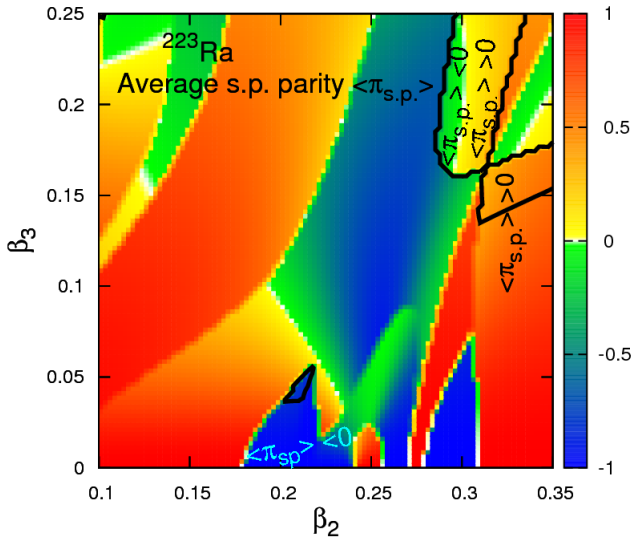

Figure 6.7.: Average s.p. model parity in ^{223}Ra as a two-dimensional function in the plane (β_2, β_3) together with the contour $a^{(+)} = a_{\mathrm{qoc}} = 0.12$ from Fig 6.6.

7. Random Phase Approximation for complex deformed nuclei

7.1. Introduction

This theory gives some more insight on the relations to the microscopic degrees of freedom. Following [50], RPA is a theory widely used for the calculation of vibrational excitations, particularly for low-lying quadrupole and octupole vibrations. One major feature of this theory is that the ground state is not considered to be of purely independent particle character. Instead, correlations can occur which lead to an enhancement of some electromagnetic transition rates. Ground state correlations can be thought of as vibrational zero-point motions.

Originating from a theory for the plasma oscillations of an electron gas (Bohm and Pines, 1953), it was later put on a more elegant basis by Gellmann, Brueckner and Hubbard in 1957 by means of a summation of perturbation series. In the same year the first application to nuclear physics was made by Ferrell for the monopole vibrations of the spherical nucleus ^{16}O.

In our approach we take the single-particle energies and wave functions from the calculations presented in chapter 5. The treatment therefore rests on the Woods-Saxon parameterization and is phenomenologically motivated. We also assume a separable residual interaction as shown below.

The systematic study of deformed RPA calculations is relatively new, while spherical nuclei, especially in the spherical tin region (from ^{114}Sn to ^{140}Sn) have been studied by spherical quasiparticle RPA calculations as well as in the Quasiparticle-Phonon Model (QPM) with HFB single-particle input by N. Tsoneva et al. Such calculations allow the prediction of significant multi-phonon contributions to the mean energies and transition strengths in these nuclei in contrast to the pygmy dipole resonance states with their one-phonon character.

7.2. Derivation of the RPA equation

In order to derive the RPA equations, we will first turn to the Tamm-Dancoff Approximation (TDA) which considers the particle-hole interaction based on the uncorrelated Hartree-Fock (HF) groundstate. We use a so-called equation of motion method [45, 50] and follow the argumentation in [15] and [44].

As a starting point we take a set $|\nu\rangle$ of exact eigensolutions of the Hamiltonian H

$$H|\nu\rangle = E|\nu\rangle \tag{7.1}$$

and define creation and destruction operators by means of

$$|\nu\rangle = Q_\nu^\dagger|0\rangle \tag{7.2}$$
$$Q_\nu|0\rangle = 0\,. \tag{7.3}$$

Together with the Schrödinger equation (7.1) we get the equation of motion

$$[H, Q_\nu^\dagger]|0\rangle = (E_\nu - E_0)Q_\nu^\dagger|0\rangle\,. \tag{7.4}$$

Multiplying this equation with an arbitrary state of the form $\langle 0|\delta Q$ gives

$$\langle 0|[\delta Q, [H, Q_\nu^\dagger]]0\rangle = (E_n u - E_0)\langle 0|[\delta Q, Q_\nu^\dagger]|0\rangle\,. \tag{7.5}$$

The use of the commutator is legitimate because of $\langle 0|Q_\nu^\dagger = \langle 0|HQ_\nu^\dagger = 0$. The treatment is exact until now because $\delta Q|0\rangle$ exhausts the whole Hilbert space. If we approximate the exact ground state $|0\rangle$ by the HF ground state and the operator Q_ν by the collective particle-hole operator

$$Q_\nu^\dagger = \sum_{mi} C_{mi}^\nu a_m^\dagger a_i\,, \tag{7.6}$$

we obtain the TDA equation

$$\sum_{nj}\langle HF|[a_i^\dagger a_m, [H, a_n^\dagger a_j]]|HF\rangle C_{nj}^\nu = E_\nu^{TDA} C_{mi}^\nu\,, \tag{7.7}$$

where E_ν^{TDA} is the excitation energy in TDA approximation and C_{mi}^ν is the expansion coefficient for the state $|\nu\rangle$. In order to consider 2p-2h correlations in the ground state, we extend $Q_\nu^\dagger$ as follows,

$$Q_\nu^\dagger = \sum_{mi} X_{mi}^\nu a_m^\dagger a_i - \sum_{mi} Y_{mi}^\nu a_i^\dagger a_m\,, \tag{7.8}$$

where the minus sign has been chosen by convenience. As normalization condition for the RPA states one chooses $\langle 0|QQ^\dagger|0\rangle = \sum(X^2 - Y^2)$. The RPA ground state is defined in such a way that

$$Q_\nu|RPA\rangle = 0\,. \tag{7.9}$$

Instead of C^ν_{mi} we obtain X^ν_{mi} and Y^ν_{mi} and additionally two variations. Therefore we obtain two sets of equations from (7.5):

$$\langle RPA|[a_i^\dagger a_m,[H,Q_\nu^\dagger]]|RPA\rangle = \hbar\Omega_\nu\langle RPA|[a_i^\dagger a_m,Q_\nu^\dagger]|RPA\rangle \tag{7.10}$$
$$\langle RPA|[a_m^\dagger a_i,[H,Q_\nu^\dagger]]|RPA\rangle = \hbar\Omega_\nu\langle RPA|[a_m^\dagger a_i,Q_\nu^\dagger]|RPA\rangle\,, \tag{7.11}$$

where $\hbar\Omega_\nu$ is the excitation energy of the state $|\nu\rangle$.

A further approximation frequently made is the so-called *quasi-boson approximation*. Assuming that the correlated ground state does not differ from the HF ground state very much, all expectation values can be calculated in the HF approximation:

$$\begin{aligned}\langle RPA|[a_i^\dagger a_m,a_n^\dagger a_j]|RPA\rangle &= \delta_{ij}\delta_{mn}-\delta_{mn}\langle RPA|a_j a_i^\dagger|RPA\rangle-\delta_{ij}\langle RPA|a_n^\dagger a_m|RPA\rangle\\ &\approx \langle HF|[a_i^\dagger a_m,a_n^\dagger a_j]|HF\rangle=\delta_{ij}\delta_{mn}\,.\end{aligned} \tag{7.12}$$

The name quasi-boson approximation (QBA) comes from the use of the boson commutator relations for the pair creation and destruction operators, which however violates the Pauli principle. In the QBA it becomes clear that the absolute squares of the amplitudes X^ν_{mi} and Y^ν_{mi} give the probability to find the state $a_m^\dagger a_i|0\rangle$ and $a_i^\dagger a_m|0\rangle$ in the exact system $|\nu\rangle$. For the corresponding components of the transition density $\rho^{(1)}=\langle 0|a_q^\dagger a_p|\nu\rangle$ one gets the relations

$$\rho^{(1)^\nu}_{mi} = \langle 0|a_i^\dagger a_m|\nu\rangle\approx\langle HF|[a_i^\dagger a_m,Q_\nu^\dagger]|HF\rangle = X^\nu_{mi} \tag{7.13}$$
$$\rho^{(1)^\nu}_{im} = \langle 0|a_m^\dagger a_i|\nu\rangle\approx\langle HF|[a_m^\dagger a_i,Q_\nu^\dagger]|HF\rangle = Y^\nu_{mi}\,. \tag{7.14}$$

This allows to write (7.11) in a compact way:

$$\begin{pmatrix}A & B\\ B^* & A^*\end{pmatrix}\begin{pmatrix}X^\nu\\ Y^\nu\end{pmatrix}=\hbar\Omega_\nu\begin{pmatrix}1 & 0\\ 0 & -1\end{pmatrix}\begin{pmatrix}X^\nu\\ Y^\nu\end{pmatrix}\,, \tag{7.15}$$

with a Hermitian matrix A and a symmetric matrix B given by

$$A_{minj} = \langle HF|[a_i^\dagger a_m[H,a_n^\dagger a_j]]|HF\rangle=(\varepsilon_m-\varepsilon_i)\delta_{mn}\delta_{ij}+\bar v_{mjin} \tag{7.16}$$
$$B_{minj} = -\langle HF|[a_i^\dagger a_m[H,a_j^\dagger a_n]]|HF\rangle=\bar v_{mnij}\,, \tag{7.17}$$

with RPA energies $\hbar\Omega_\nu$, single-particle energies ε as well as RPA forward and backward amplitudes X^ν and Y^ν.

7.3. Separable residual interaction

From the single-particle program we obtain as output the single-particle energies ε_ν and wave functions $\psi_\nu=\sum_\alpha c_\alpha\varphi_\alpha$ with basis functions $\psi_\alpha=|\alpha\rangle$ where α is a short notation for all quantum numbers,

$$|\alpha\rangle=|N\,n_z\,\Lambda\,\Omega\rangle\,. \tag{7.18}$$

The states are filled with particles from the bottom of the potential up to the last occupied orbital which defines the Fermi level. We then consider a given amount of states below and above the Fermi surface and construct all possible particle-hole excitation combinations.

We use multipole operators of the form

$$\hat{Q}_{\lambda\mu} = r^{\lambda} Y_{\lambda\mu}(\theta, \phi) \tag{7.19}$$

with a simple power law for the radial part and spherical harmonics. When making calculations for a given multipolarity λ we always make a summation over μ. Therefore we define the summed multipole operators

$$\hat{Q}_{\lambda} = \sum_{\mu=-\lambda}^{\lambda} \hat{Q}_{\lambda\mu} \,. \tag{7.20}$$

The RPA matrices A and B are constructed as

$$A_{minj} = (\varepsilon_m - \varepsilon_i)\delta_{mn}\delta_{ij} + \bar{v}_{mjin} \tag{7.21}$$

$$B_{minj} = \bar{v}_{mnij} \tag{7.22}$$

where A is a Hermitian matrix and B is symmetric. We take the matrix elements of the residual interaction to be separable in the particle-hole indices. This means [15]

$$\bar{v}_{mjin} = \kappa_{\lambda} \cdot D_{mi} D^{*}_{nj} \tag{7.23}$$

where m and n label particles while the notations i and j is reserved for holes. The matrix elements (7.23) are calculated between a particle and a hole state

$$D_{mi} = \langle m|\hat{Q}_{\lambda}|i\rangle = \sum_{\alpha,\beta} c_{\alpha} c_{\beta} \langle \alpha|\hat{Q}_{\lambda}|\beta\rangle \tag{7.24}$$

with expansion coefficients c_{α} and c_{β} taken from the eigenvectors of the single-particle program.

For technical reasons we relabel the particle-hole pair combinations into a single index

$$\{m, i\} \longrightarrow \sigma \tag{7.25}$$

to obtain two-dimensional matrices A and B.

As the reader might notice there are four possible combinations for the product of the D matrix elements in (7.23), depending whether the states are taken from protons or neutrons. Therefore the matrices A and B can be constructed in a block form according to

$$A = \begin{pmatrix} A^{nn} & A^{np} \\ A^{pn} & A^{pp} \end{pmatrix} \qquad B = \begin{pmatrix} B^{nn} & B^{np} \\ B^{pn} & B^{pp} \end{pmatrix} . \tag{7.26}$$

The matrices A and B are the same except for the diagonal matrix elements in our case.

7.4. Simultaneous diagonalization of the RPA matrices

We have to diagonalize the matrix

$$C = \begin{pmatrix} A & B \\ -B^* & -A^* \end{pmatrix} \tag{7.27}$$

to obtain the RPA solution. Usually the dimension of this matrix is quite large so that it would be advantageous to use the special symmetry of C instead of a direct calculation of its eigenvalues and eigenvectors.

This is indeed possible and the procedure is for example given in [71]. In a very short form it can be formulated as follows.

1. Construct the matrices $M = A + B$ and $N = A - B$.

2. Check whether N is positive definite. In case of positive definiteness all eigenvalues are positive. If N is not positive definite M is automatically positive definite. In this latter case switch the notation of M and N, i.e. M becomes N and N becomes M.

3. Diagonalize N and construct the transformation matrix T from the eigenvectors. It is then possible to construct the diagonal matrix $N_d = \tilde{T}NT$ where the tilde denotes the transposed matrix.

4. Construct the matrix $M' = \tilde{T}MT$.

5. Construct the matrix $M'' = N_d^{1/2} M' N_d^{1/2}$.

6. Diagonalize M'' and obtain eigenvalues ω_ν^2 and eigenvectors V_ν'' normalized to 1. Multiply V_ν'' with $\sqrt{|\omega_\nu|}$ to obtain new eigenvectors V_ν'' normalized to $|\omega_\nu|$.

7. The RPA amplitudes can now be constructed as

$$X_\nu = \frac{1}{2} T \left(\frac{1}{\omega_\nu} N_d^{1/2} + N_d^{-1/2} \right) V_\nu'' \tag{7.28}$$

$$Y_\nu = \frac{1}{2} T \left(\frac{1}{\omega_\nu} N_d^{1/2} - N_d^{-1/2} \right) V_\nu'' \tag{7.29}$$

It was checked that indeed this procedure gives the same eigenvalues and eigenvectors as a direct diagonalization of the large matrix C. A computer code according to this algorithm was written.

7.5. Calculation of transition strengths

Once the RPA solution is obtained we can calculate the transition amplitude

$$\langle 0|\hat{F}|\nu\rangle = \sum_{mi} \left(F_{im}X^{\nu}_{mi} + F_{mi}Y^{\nu}_{mi}\right) , \tag{7.30}$$

where $\hat{F}$ is a transition operator, which is defined as follows. We have an isoscalar operator

$$\hat{F}^{IS} = \sum_{i=1}^{A} \sum_{\mu=-\lambda}^{\lambda} r_i^{\lambda} Y_{\lambda\mu} \tag{7.31}$$

and an isovector operator

$$\hat{F}^{IV} = \sum_{i=1}^{A} \sum_{\mu=-\lambda}^{\lambda} \tau_3^{(i)} r_i^{\lambda} Y_{\lambda\mu} \tag{7.32}$$

where τ_3 is the isospin of the isospin operator $\hat{\tau}_3$.

7.6. Test calculations for ^{208}Pb

The program is tested quite thoroughly. The formulas for the analytic matrix elements of the multipole operators are also calculated numerically and are compared to the obtained analytic values. The procedure of the simultaneous diagonalization of the RPA matrices is checked to give the same results as the direct diagonalization of the C matrix.

Furthermore, we check that the amplitudes fulfill the normalization

$$\sum_{mi} \left(|X_{mi}|^2 - |Y_{mi}|^2\right) = 1 \tag{7.33}$$

for all particle-hole indices ν. For separable interactions the eigenvalue problem reduces to a simple dispersion relation [15],

$$\frac{1}{\kappa_\lambda} = \sum_{mi} |D_{mi}|^2 \frac{2\varepsilon_{mi}}{\hbar\omega_\nu^2 - \varepsilon_{mi}^2} . \tag{7.34}$$

We run test calculations for ^{208}Pb for the multipolarities $\lambda = 1, 2$ and 3. Results for such calculations can be found in [15] where early RPA calculations from Ring and Speth are presented. The κ_λ-values were chosen in such a way so as to reproduce the energetically low-lying peaks. Results are shown in Figure 7.1.

7.7. Outlook

7.7.1. Improved treatment of the single-particle continuum

If one takes many particle-hole configurations for the RPA calculation, one has to consider unbound continuum states with $E > 0$, too. The single-particle program delivers such states from the diagonalization procedure, but they are not very closely lying together. In order to obtain a denser continuum, one can take basis states which go to zero at a given boundary. By putting the boundary more outwards, the continuum states come closer to each other as we will see.

Let us for simplicity imagine a spherical potential box with radius a, or, to be more precise let us consider the potential

$$V(r) = \begin{cases} -V_0 & r < a \\ 0 & r > a \end{cases} . \tag{7.35}$$

Then, for continuum states with $E > 0$, one can make the ansatz

$$R_l(r) = \begin{cases} A j_l(qr) & r < a \\ B j_l(kr) + C n_l(kr) & r > a \end{cases} , \tag{7.36}$$

where j_l and n_l are spherical Bessel and spherical Neumann functions, respectively, with wave numbers

$$k = \frac{\sqrt{2mE}}{\hbar} \tag{7.37}$$

$$q = \frac{\sqrt{2m(E+V_0)}}{\hbar} . \tag{7.38}$$

Introducing the notation $C/B = -\tan\delta_l(k)$ for the amplitude ratio, the form of $R_l(r)$ reads asymptotically [46]

$$R_l(r) = \frac{B}{\cos\delta_l(k)} \frac{1}{kr} \sin\left(kr - \frac{l\pi}{2} + \delta_l(k)\right) . \tag{7.39}$$

If we place a boundary at R_b far enough outside ($kr \gg l$), where the wave function has to vanish, $R_l(R_b) = 0$, then we obtain

$$kR_b - \frac{l\pi}{2} + \delta_l = n\pi , \tag{7.40}$$

and solving this for $k = k_n$ gives

$$k_n = (2n + l)\frac{\pi}{2R_b} - \frac{\delta_l}{R_b} . \tag{7.41}$$

This leads to the easy relation

$$\Delta k = k_{n+1} - k_n = \frac{\pi}{R_b}\,, \tag{7.42}$$

from which one can read off that Δk becomes smaller, and thus the spectrum becomes denser, if R_b grows.

7.7.2. Starting from Hartree-Fock Bogolyubov calculations

The RPA program is based on a phenomenological single-particle program. A natural improvement would be to base the RPA program on single-particle energies and wave functions obtained from a self-consistent Hartee-Fock Bogolyubov calculation. Such a code named HFODD is available and published in Computer Physics Communications by J. Dobaczewski et al [68]. It solves the nuclear Skyrme-Hartree-Fock or Skyrme-Hartree-Fock-Bogolyubov problem by using the Cartesian deformed harmonic oscillator basis.

It is possible to run the code for different Skyrme parameter sets and for a given set of multipole deformations $\alpha_{\lambda\mu}$. Then the single-particle wave functions are obtained as expansions in the deformed harmonic oscillator basis. In order to extend the RPA program to use the HFODD wave functions as input, one would have to calculate matrix elements of the type $\langle n'_x\, n'_y\, n'_z|\hat{Q}_{\lambda\mu}|n_x\, n_y\, n_z\rangle$. These matrix elements have been worked out by Martin and Robledo and can be found in [69].

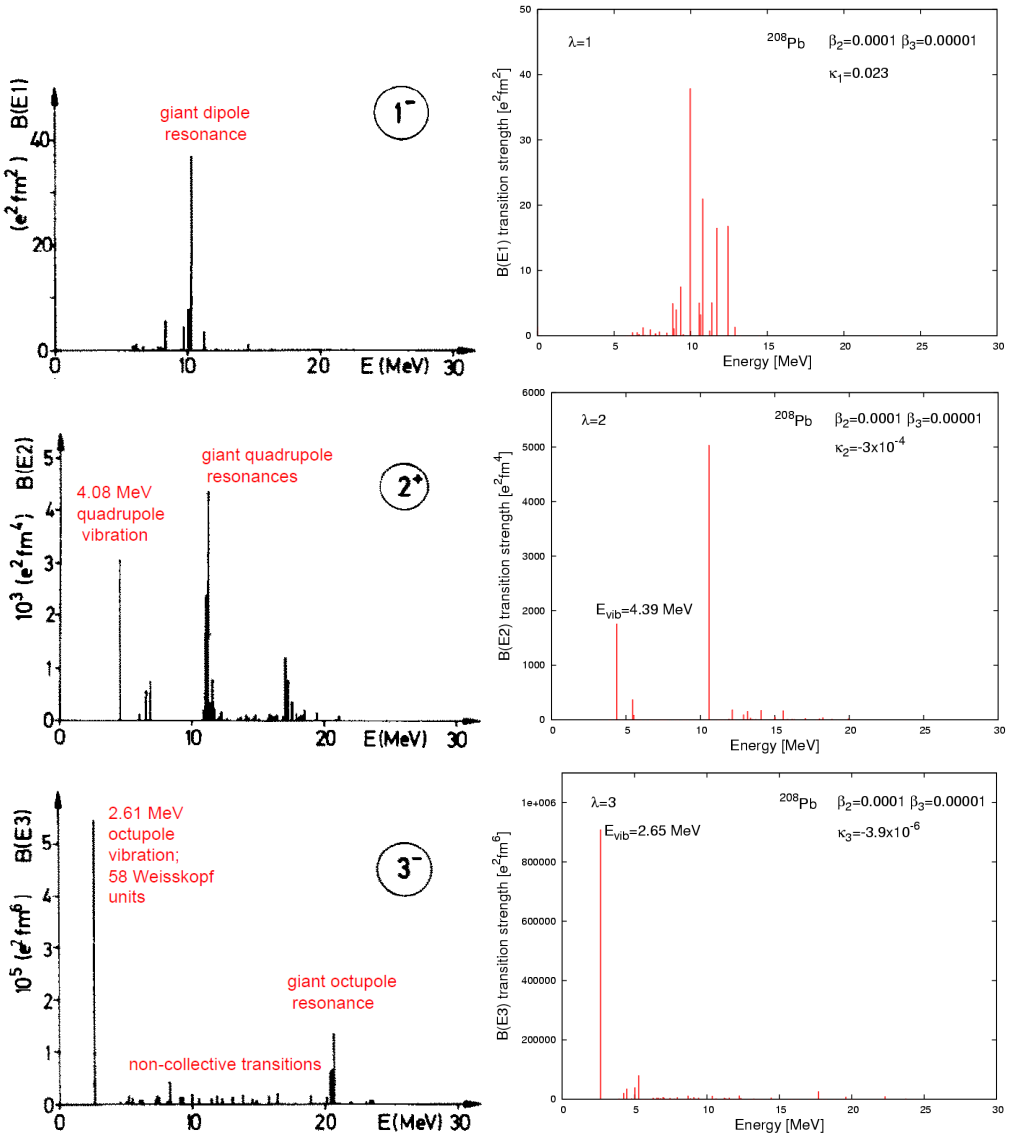

Figure 7.1.: Early RPA calculation for ^{208}Pb from 1974 on the left side and spherical RPA calculations using the deformed RPA program on the right side.

8. Conclusions

In chapter 3 the coherent quadrupole-octupole model is extended to the case of non-yrast bands. Besides the ground state band the model also describes different negative parity level-sequences as well as excited β-bands.

The model predicts possible E(1) and E(3) transitions between states with opposite parity within various alternating-parity bands. It even can be said that the considered scheme can be used for the interpretation of data on excitation energies whose place in the structure of the collective spectrum has not yet been determined.

The approach was applied to a number of selected nuclei for which a relatively large number of data on B(E1), B(E2) and B(E3) transitional probabilities are available. Of course one can easily extend the approach to a wider range of nuclei, especially in the rare-earth and actinide region.

In chapter 4 the quadrupole-octupole model is extended beyond the limit of a coherent interplay. The oscillations in the quadrupole and octupole degree of freedom can have different frequencies ω_2 and ω_3. In the analytically treatable case only a special class of solutions with an ellipse as minimum in the potential is considered. The non-coherent solution allows all parameters to vary freely and independently and the parameters can be adjusted within the full class of solutions of the model.

A very evident result is that the root mean square deviation of the theoretical and experimental data could be improved in this way. The independence of the parameters leaves the fitting algorithm a lot of freedom to finally find a unique shape of the potential. As the parameters for the different nuclei show some individuality and do not vary completely smoothly, also the resulting wave functions are unique in their shapes.

A not so evident result is that the quadrupole deformation expectation values for the different nuclei, obtained from the ground state wave functions at angular momentum $I = 0$, at least roughly follow the experimentally known numbers. This can be seen as a true model prediction since no information about the quadrupole deformation values is used for the adjustment of the parameters.

In chapter 6 the connection of intrinsic and collective motion is investigated. We propose a coupling scheme for a quadrupole-octupole vibrating and rotating nuclear core and a single nucleon with a mixed parity. The considered coupling mechanism imposes a

generalized projected form of the Coriolis decoupling factor for the single-particle states with $K = 1/2$.

As a result, by comparing the deformed shell model values of the decoupling factor with the values obtained from the collective model and by requiring a consistency in the signs of the calculated dominant parity and the experimentally established parity in the ground state, one is able to outline physically reasonable deformation regions in the (β_2, β_3)-plane.

In chapter 7 the deformed shell model output is used as input for deformed RPA calculations. This work is still in an early stage. First test calculations for the case of spherical ^{208}Pb show that the results of the deformed RPA program are in agreement with earlier spherical RPA calculations. Extended checks of the program and its application to deformed nuclei is subject of future work.

A. Appendices

A.1. Equation of motion for the deformation parameters

This appendix treats the idea to perform classical calculations for the time-dependent deformation parameters by applying the Lagrange equations of classical mechanics.

As I have shown [34], the vibrational part of the Hamiltonian leads to Lissajous-trajectories. This is easily seen from the Lagrange function $L = T - V$ in the generalized coordinates β_2, β_3, $\dot{\beta}_2$ and $\dot{\beta}_3$ with a potential (deformation) energy

$$T(\dot{\beta}_2, \dot{\beta}_3) = \frac{1}{2} B_2 \dot{\beta}_2^2 + \frac{1}{2} B_3 \dot{\beta}_3^2 \tag{A.1}$$

and a kinetic (surface movement) energy

$$V(\beta_2, \beta_3) = \frac{1}{2} C_2 \beta_2^2 + \frac{1}{2} C_3 \beta_3^2 \tag{A.2}$$

leading to the differential equations

$$\ddot{\beta}_2(t) + \omega_2^2 \beta_2(t) = 0 \qquad \ddot{\beta}_3(t) + \omega_3^2 \beta_3(t) = 0\,, \tag{A.3}$$

where $\omega_2 = \sqrt{C_2/B_2}$ and $\omega_3 = \sqrt{C_3/B_3}$. The solutions are the well-known Lissajous-curves.

The complete vibrational-rotational Hamiltonian was not solved however. This is where we revisit the problem in the present work.

Some simple algebra shows that adding the coupling term

$$V_{\text{rot-vib}} = \frac{X}{d_2 \beta_2^2 + d_3 \beta_3^2} \tag{A.4}$$

to the potential (A.2) leads to the coupled differential equation system

$$B_2 \ddot{\beta}_2 + C_2 \beta_2 - \frac{2X d_2 \beta_2}{(d_2 \beta_2^2 + d_3 \beta_3^2)^2} = 0 \tag{A.5}$$

$$B_3 \ddot{\beta}_3 + C_3 \beta_3 - \frac{2X d_3 \beta_3}{(d_2 \beta_2^2 + d_3 \beta_3^2)^2} = 0\,. \tag{A.6}$$

It should be noted that the binomial formula in the denominator leads a mixing $\beta_2^2\beta_3^2$-term which makes it very unprobable that an analytic solution exists. Indeed, Mathematica did not find a solution when this system is tried to be solved with the `DSolve` command.

Since there is no analytic solution we need a numeric approach to the problem. The first step is to reduce the system with two equations of second order to a system with four first-order differential equations. This is very advantageous in order to apply a numerical solution method like Euler or Runge-Kutta.

The trick is to introduce new functions

$$z_2(t) = \frac{d\beta_2(t)}{dt} \qquad z_3(t) = \frac{d\beta_3(t)}{dt} \tag{A.7}$$

which are defined as derivatives of β_2 and β_3.

It is a good idea to start with the easier case (A.3) because of reasons of simplicity and because we can check the numerical result with the analytically known Lissajous-curves. With (A.7) we have

$$\frac{d}{dt}z_2(t) = -\omega_2^2\beta_2(t) \tag{A.8}$$

$$\frac{d}{dt}z_3(t) = -\omega_3^2\beta_3(t) \tag{A.9}$$

and therefore the following first order differential equation system:

$$\dot{\beta}_2(t) = z_2(t) \tag{A.10}$$

$$\dot{\beta}_3(t) = z_3(t) \tag{A.11}$$

$$\dot{z}_2(t) = -\omega_2^2\beta_2(t) \tag{A.12}$$

$$\dot{z}_3(t) = -\omega_3^2\beta_3(t)\,. \tag{A.13}$$

We are not interested in a very accurate solution of the differential equation since it is only used to get an idea about the classical movement of the system in the deformation plane. For the purpose of generating some short animations to visualize the surface motion of the nucleus in real 3D position space the Euler method should work just fine.

For this method we need an initial set of coordinates β_2 and β_3 and velocities $\dot{\beta}_2$ and $\dot{\beta}_3$ at a given time t_0 and a certain small step size h. Then for the next time step t_1 one calculates a new set of coordinates and velocities and for the next time step t_2 the calculation relies on the values already known at t_1 and so on. It is clear that small errors tend to add up as time increases.

The most simple example would be a circle. It can be seen from the solution of (A.3),

$$\beta_2(t) = \beta_{2,\max}\sin(\omega_2 t) \qquad \beta_3(t) = \beta_{3,\max}\sin(\omega_3 t + \alpha)\,, \tag{A.14}$$

that we get a unit circle in the deformation plane if we set $\omega_2 = \omega_3 = \beta_{2,\max} = \beta_{3,\max} = 1$, $\alpha = \pi/2$ and let t run in the interval $[0, 2\pi)$. Choosing $t_0 = 0$ this leads to the following initial conditions:

$$\beta_2(0) =: \beta_{2,0} = 0 \tag{A.15}$$
$$\beta_3(0) =: \beta_{3,0} = 1 \tag{A.16}$$
$$z_2(0) =: z_{2,0} = \dot{\beta}_2(0) = 1 \tag{A.17}$$
$$z_3(0) =: z_{3,0} = \dot{\beta}_3(0) = 0 \tag{A.18}$$

Performing one time step in the Euler algorithm we have

$$t_1 = t_0 + h \tag{A.19}$$
$$\beta_{2,1} = \beta_{2,0} + \dot{\beta}_2(t_0)h = \beta_{2,0} + z_2(t_0)h = \beta_{2,0} + z_{2,0}h \tag{A.20}$$
$$\beta_{3,1} = \beta_{3,0} + \dot{\beta}_3(t_0)h = \beta_{3,0} + z_3(t_0)h = \beta_{3,0} + z_{3,0}h \tag{A.21}$$
$$z_{2,1} = z_{2,0} + \dot{z}_2(t_0)h = z_{2,0} + (-\omega_2^2\beta_2(t_0))h = z_{2,0} - \omega_2^2\beta_{2,0}h \tag{A.22}$$
$$z_{3,1} = z_{3,0} + \dot{z}_3(t_0)h = z_{3,0} + (-\omega_3^2\beta_3(t_0))h = z_{3,0} - \omega_3^2\beta_{3,0}h \tag{A.23}$$

and it is clear how to continue.

For the system (A.6) the procedure is completely analoguous. In that case the first order system becomes

$$\dot{\beta}_2(t) = z_2(t) \tag{A.24}$$
$$\dot{\beta}_3(t) = z_3(t) \tag{A.25}$$
$$\dot{z}_2(t) = -\frac{C_2}{B_2}\beta_2(t) + \frac{2Xd_2\beta_2(t)}{B_2\left[d_2\beta_2(t)^2 + d_3\beta_3(t)^2\right]^2} \tag{A.26}$$
$$\dot{z}_3(t) = -\frac{C_3}{B_3}\beta_3(t) + \frac{2Xd_3\beta_3(t)}{B_3\left[d_2\beta_2(t)^2 + d_3\beta_3(t)^2\right]^2}\,. \tag{A.27}$$

This method was implemented in a Fortran program and choosing a not too small value of h, like for example 0.1, it can be seen that the numerical solution curve tends to deviate from the true solution. Adjusting h to a smaller value like 0.01 improves the numerical solution considerably. The true solution is a closed circle and if one lets the time run one never escapes this circle. In case of the numerical solution the circle is almost closed but the curve tends to move slowly more and more in outward direction with each rounding, giving the shape of a spiral.

Choosing Mathematica for the task of the numerical solution gave more precise results. This is due to the fact that Mathematica's command `NDSolve` works with a much more sophisticated algorithm to solve the differential equation system. This has also the advantage that one can directly produce a series of images of the nucleus in an array which can be exported as e.g. a GIF-animation.

In case of the Fortran program the output data was visualized using Gnuplot to produce wire frame images of the nucleus.

There is one open question related to the analysis of this section, namely if there is a possibility to have closed curves for the system (A.6). It was mentioned that the numerical solution goes away from the true solution which simply lies in the nature of the numerical method. So on the basis of numerical investigation it is doubtful if one is able to decide if there are closed curves. We also do not have an analytic solution, so to answer this question one would somehow have to decide it by looking at the differential equation.

A.2. Path Integral Monte Carlo calculations

A somewhat more quantum mechanical approach to the problem of how the nucleus moves is to assume a more random motion instead of given trajectories. This can be achieved with a path integral approach to the problem. From the Metropolis algorithm [52] explained below we get a path in the 2D deformation space, moving from one point to a next neighbouring one in a way very similar to the Brownian motion. This gives a more realistic picture of the surface motion of the nucleus. With this method we are even able to obtain the groundstate energy and wave function which belongs to the potential.

A.2.1. Definition of the path integral

We closely follow the first section of [51]. The path integral is often called the Kernel and is obtained by integration over all possible paths between two fixed points in space and time,

$$K(b,a) = \int_a^b e^{iS[b,a]} \mathcal{D}x(t) \tag{A.28}$$

where S is the classical action for a given path:

$$S = \int_{t_a}^{t_b} L(\dot{x}, x, t) dt \,. \tag{A.29}$$

In order to define integration over a functional space, one introduces a time lattice. The time axis is sliced into $N+1$ points and the coordinates (assuming a one-dimensional motion) of the particle are given by $(x_1, x_2, \ldots, x_N)$ with $-\infty < x_j < \infty$. This leads to the following action on the lattice

$$S_{\text{lat}}[x] = \sum_{j=1}^{N} a \left[\frac{m}{2} \frac{(x_{j+1} - x_j)^2}{a^2} - V(x_j) \right] , \tag{A.30}$$

where $a = T/(N+1)$ with which the path integral becomes

$$K(b,a)_{\text{lat}} = \int_{x_0=x_a}^{x_N=x_b} e^{iS_{\text{lat}}[x]} \prod_{j=1}^{N} \frac{dx_j}{A} \tag{A.31}$$

with a normalization factor A.

A.2.2. The Metropolis algorithm for the Harmonic Oscillator

In order to see how a numerical simulation looks like with the Path Integral Monte Carlo (PIMC) method, we will treat the Harmonic oscillator. This system is analytically treatable with the introduction of a time lattice, giving the result [51]

$$K(b,a) = \sqrt{\frac{m\omega}{2\pi i \sin(\omega T)}} \exp\left\{ \frac{im\omega}{2\sin(\omega T)} [(x_a^2 + x_b^2)\cos(\omega T) - 2x_a x_b] \right\} . \tag{A.32}$$

Since we are more interested in a computer algorithm which works for an arbitrarily given potential, we will now see how one can obtain the oscillator's ground state wave function (or its square to be more precise) as well as the ground state energy with the Metropolis algorithm.

This algorithm was first presented by Metropolis in [52]. We follow the procedure given in [53]. The Metropolis algorithm is a Markov chain updating algorithm. For a given current configuration (path) a new configuration is proposed, the change δS in action is computed and the new configuration is accepted with probability min $\left(1, e^{-\delta S/\hbar}\right)$.

To illustrate this let us take the action of the harmonic oscillator

$$S[x(t)] = \int_{t_a}^{t_b} \left(\frac{1}{2} m\dot{x}^2 + \frac{1}{2} m\omega^2 x^2 \right) dt \tag{A.33}$$

and discretize it for Monte Carlo evaluation

$$\frac{S}{\hbar} = \frac{m\varepsilon}{2\hbar} \sum_{j=0}^{N-1} \left[\left(\frac{x_{j+1} - x_j}{\varepsilon} \right)^2 + \omega^2 \left(\frac{x_{j+1} + x_j}{2} \right)^2 \right] , \tag{A.34}$$

where $N\varepsilon = t_b - t_a$ and ε chosen small enough to have small discretization errors.

Then the Metropolis algorithm to update location x_j works as follows: First one proposes a random shift $-\Delta \leq \delta \leq \Delta$ with uniform probability. Then one calculates the change in action $\delta S/\hbar$ caused by this change. Then the new location $x_j^{\text{new}} = x_j + \delta$ is accepted with probability min $\left(1, e^{-\delta S/\hbar}\right)$. As a rule of thumb one should tune Δ to an acceptance rate of about 50 %. For a lower rate one wastes too much time with rejections and for a higher rate one is moving through phase space too slowly.

This procedure is repeated for each x_j for $j = 1, \ldots, N-1$ which is called a sweep. One should perform such a sweep several times in order to obtain sufficiently small autocorrelations.

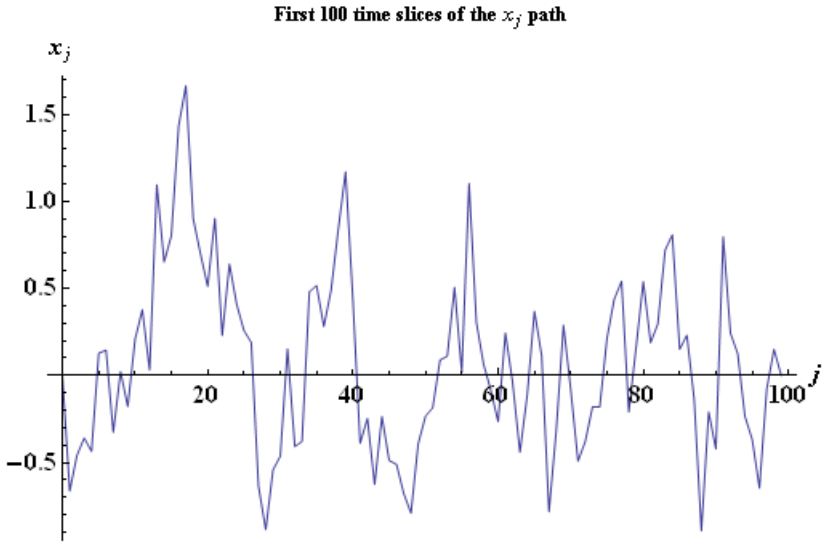

Figure A.1.: A typical path generated by the Metropolis algorithm for the harmonic oscillator after several sweeps.

If one plots all the points belonging to the path in space, then one gets a point cloud picture which gives a good information about the wave function. Indeed the wave function can be obtained from the path by means of a bin count. One defines small intervals for the position and counts how often the particle is in this bin for the given path. This can be done very elegantly in Mathematica using the command `BinCount`. The result can immediately be interpreted as $|\psi_0(x)|^2$ with ψ_0 being the ground state wave function.

In order to obtain the ground state eigenvalue one can square root this function to obtain $\psi_0(x)$. If one applies a rule for second order numerical derivation of a function one gets $\psi_0''(x)$. This makes it possible to calculate $E_0 = \langle\psi_0|\hat{H}|\psi_0\rangle$.

A.3. Matrix elements for the s.p. Hamiltonian for an axially deformed HO basis

These matrix elements are also given in [67] but were rederived in order to have them in a form more suitable for a computer code and in order to eliminate some misprints.

Figure A.2.: Point cloud generated by the Metropolis algorithm for a simple Gaussian wave function (ground state of a 2D harmonic oscillator).

A.3.1. Kinetic energy matrix elements

The operator $\hat{T}$ is diagonal in Λ and Σ and the matrix elements are given by

$$\langle n_\rho, n_z, \Lambda|\hat{T}|n_\rho, n_z, \Lambda\rangle = \frac{1}{2}\hbar\omega_\perp(n_\perp+1) + \frac{1}{2}\hbar\omega_z\left(n_z+\frac{1}{2}\right) \tag{A.35}$$

$$\langle n_\rho, n_z, \Lambda|\hat{T}|n_\rho-1, n_z, \Lambda\rangle = \frac{1}{2}\hbar\omega_\perp\sqrt{n_\rho(n_\rho+|\Lambda|)} \tag{A.36}$$

$$\langle n_\rho, n_z, \Lambda|\hat{T}|n_\rho, n_z-2, \Lambda\rangle = -\frac{1}{4}\hbar\omega_z\sqrt{(n_z-1)n_z} \tag{A.37}$$

A.3.2. Woods-Saxon potential matrix elements

The ϕ-integration is trivial and therefore we are left with two-fold integrals over the variables ξ and η which are related to the cylindrical coordinates by

$$\sqrt{\eta} \equiv \sqrt{\frac{M\omega_\perp}{\hbar}}r \qquad \xi \equiv \sqrt{\frac{M\omega_z}{\hbar}}z\,. \tag{A.38}$$

The integrals are

$$\begin{aligned}\langle n'_\rho, n'_z, \Lambda', \Sigma'|V|n_\rho, n_z, \Lambda, \Sigma\rangle = \delta_{\Lambda',\Lambda}\delta_{\Sigma',\Sigma}N_{n'_z}N_{n_z}N^{\Lambda'}_{n'_\rho}N^{\Lambda}_{n_\rho}\int_0^\infty d\eta\eta^\Lambda e^{-\eta} \\ \times\int_{-\infty}^{+\infty} d\xi e^{-\xi^2}H_{n'_z}(\xi)H_{n_z}(\xi)L^{\Lambda'}_{n'_\rho}(\eta)L^{\Lambda}_{n_\rho}(\eta)V(\xi,\eta)\end{aligned} \tag{A.39}$$

and can be fastly evaluated using Gauss-Hermite and Gauss-Laguerre quadrature rules. In the previous expression we use the normalization factors

$$N_{n_z} \equiv \frac{1}{\sqrt{\sqrt{\pi} 2^{n_z} n_z!}} \qquad N_{n_\rho}^{\Lambda} \equiv \sqrt{\frac{n_\rho!}{(n_\rho + |\Lambda|)!}}\,. \tag{A.40}$$

A.3.3. Spin-orbit potential matrix elements

The matrix elements are in the diagonal case

$$\begin{aligned}\langle n'_\rho n'_z \Lambda\Sigma | V_{\mathrm{so}} | n_\rho n_z \Lambda\Sigma\rangle = {} & \frac{\kappa\Lambda}{\hbar}\langle\Sigma|\sigma_z|\Sigma\rangle N_{n'_z} N_{n'_\rho}^{\Lambda} N_{n_z} N_{n_\rho}^{\Lambda} \frac{M\omega_\perp}{\hbar} \int_0^\infty d\eta \eta^{\Lambda-1} e^{-\eta} \\ \times \int_{-\infty}^{\infty} d\xi e^{-\xi^2} V(\eta,\xi) \Big\{ & \Big[\Lambda - \eta + 2n'_\rho) L_{n_\rho}^{\Lambda}(\eta) L_{n'_\rho}^{\Lambda}(\eta) - 2(n'_\rho + \Lambda) L_{n_\rho}^{\Lambda}(\eta) L_{n'_\rho - 1}^{\Lambda}(\eta)\Big] + \\ & \Big[(\Lambda - \eta + 2n_\rho) L_{n'_\rho}^{\Lambda}(\eta) L_{n_\rho}^{\Lambda}(\eta) - 2(n_\rho + \Lambda) L_{n'_\rho}^{\Lambda}(\eta) L_{n_\rho - 1}^{\Lambda}(\eta)\Big] \Big\} H_{n_z}(\xi) H_{n'_z}(\xi)\end{aligned} \tag{A.41}$$

and

$$\begin{aligned}\langle n'_\rho n'_z \Lambda'\Sigma' | V_{\mathrm{so}} | n_\rho n_z \Lambda\Sigma\rangle = {} & -\frac{\kappa}{2\hbar} N_{n'_z} N_{n_z} N_{n'_\rho}^{\Lambda'} N_{n_\rho}^{\Lambda} \sqrt{\frac{M\omega_\perp}{\hbar}} \sqrt{\frac{M\omega_z}{\hbar}} \langle\Sigma'|\sigma^{\pm}|\Sigma\rangle \\ & \times \int_0^\infty d\eta \eta^{\frac{1}{2}(\Lambda'+\Lambda-1)} e^{-\eta} \int_{-\infty}^{\infty} d\xi e^{-\xi^2} V(\eta,\xi) \Big\{ \Big[\Lambda' \Big(L_{n'_\rho}^{\Lambda'}(\eta) L_{n_\rho}^{\Lambda}(\eta) + \\ & \Big\{(\Lambda' - \eta + 2n'_\rho) L_{n_\rho}^{\Lambda}(\eta) L_{n'_\rho}^{\Lambda'}(\eta) - 2(n'_\rho + \Lambda') L_{n_\rho}^{\Lambda}(\eta) L_{n'_\rho - 1}^{\Lambda'}(\eta)\Big\}\Big) \\ & - \Lambda \Big\{(\Lambda' - \eta + 2n'_\rho) L_{n_\rho}^{\Lambda}(\eta) L_{n'_\rho}^{\Lambda'}(\eta) - 2(n'_\rho + \Lambda') L_{n_\rho}^{\Lambda}(\eta) L_{n'_\rho - 1}^{\Lambda'}(\eta)\Big\}\Big] \\ & \times \big(-\xi H_{n'_z}(\xi) H_{n_z}(\xi) + 2n_z H_{n'_z}(\xi) H_{n_z - 1}(\xi)\big) \\ + \Big[\Lambda \Big(L_{n'_\rho}^{\Lambda'}(\eta) L_{n_\rho}^{\Lambda}(\eta) + \Big\{(\Lambda - \eta + 2n_\rho) L_{n'_\rho}^{\Lambda'}(\eta) L_{n_\rho}^{\Lambda}(\eta) - 2(n_\rho + \Lambda) L_{n'_\rho}^{\Lambda'}(\eta) L_{n_\rho - 1}^{\Lambda}(\eta)\Big\}\Big) \\ & - \Lambda' \Big\{(\Lambda - \eta + 2n_\rho) L_{n'_\rho}^{\Lambda'}(\eta) L_{n_\rho}^{\Lambda}(\eta) - 2(n_\rho + \Lambda) L_{n'_\rho}^{\Lambda'}(\eta) L_{n_\rho - 1}^{\Lambda}(\eta)\Big\}\Big] \\ & \times \big(-\xi H_{n_z}(\xi) H_{n'_z}(\xi) + 2n'_z H_{n_z}(\xi) H_{n'_z - 1}(\xi)\big)\Big\}\end{aligned} \tag{A.42}$$

in the non-diagonal case with the same normalization factors as in the previous paragraph.

A.4. CQOM transition theory: analytic expressions for the integrals

A.4.1. Explicit form of the integrals over η

The integrals over η, (3.19) and (3.20), can be written in the following common form after taking into account the explicit expression for the radial wave functions

$$\begin{aligned} S_l(n_i, I_i; n_f, I_f) &= \int_0^\infty d\eta \psi_{n_f}^{I_f}(\eta) \eta^{l+1} \psi_{n_i}^{I_i}(\eta) \\ &= N \int_0^\infty e^{-c\eta^2} c^{s_f} \eta^{2s_f} L_{n_f}^{2s_f}(c\eta^2) \eta^{l+1} c^{s_i} \eta^{2s_i} L_{n_i}^{2s_i}(c\eta^2) d\eta, \end{aligned} \quad (A.43)$$

where $l = 1, 2$, $s_i = (1/2)\sqrt{k_i^2 + bX(I_i)}$, $s_f = (1/2)\sqrt{k_f^2 + bX(I_f)}$ and

$$N = N_{n_i,n_f}(c, s_i, s_f) = 2c \left[\frac{\Gamma(n_f + 1)\Gamma(n_i + 1)}{\Gamma(n_f + 2s_f + 1)\Gamma(n_i + 2s_i + 1)} \right]^{\frac{1}{2}}. \quad (A.44)$$

To derive an explicit expression for the integral (A.43) one can apply the substitution $c\eta^2 = x$ with $dx = 2c\eta d\eta$, such that

$$\eta^{l+1} d\eta = \frac{1}{2c^{1+l/2}} x^{l/2} dx. \quad (A.45)$$

Then Eq. (A.43) reads as

$$S_l(n_i, I_i; n_f, I_f) = \frac{N_{n_i,n_f}(c, s_i, s_f)}{2c^{1+l/2}} \int_0^\infty e^{-x} x^{s_i + s_f + \frac{l}{2}} L_{n_f}^{2s_f}(x) L_{n_i}^{2s_i}(x) dx. \quad (A.46)$$

By using known formulas for integration of two generalized Laguerre polynomials with different real ranks [75], [76] one obtains (A.46) in the following explicit form

$$\begin{aligned} & S_l(n_i, I_i; n_f, I_f) \\ = \; & \frac{N_{n_i,n_f}(c, s_i, s_f)}{2c^{1+l/2}} \frac{\Gamma(n_f + 2s_f + 1)}{\Gamma(1 + 2s_f)} \frac{\Gamma(n_i + s_i - s_f - \frac{l}{2})}{\Gamma(s_i - s_f - 1)} \frac{\Gamma(s_i + s_f + \frac{l}{2} + 1)}{n_i! n_f!} \\ \times \; & {}_3F_2\left(-n_f, s_i + s_f + \frac{l}{2} + 1, s_f - s_i + \frac{l}{2} + 1; 2s_f + 1, s_f - s_i + \frac{l}{2} + 1 - n_i; 1 \right), \end{aligned} \quad (A.47)$$

where ${}_3F_2$ denotes a generalized hypergeometric function [77]. The generalized hypergeometric function ${}_3F_2$ is calculated numerically through a summation of its series representation for which a Fortran code is available [78]. It can be easily checked that if the first argument of ${}_3F_2$ in (A.47) is zero, $n_f = 0$, one has ${}_3F_2 = 1$. In this case Eq. (A.47) reduces to the following simpler expression

$$S_l(n_i, I_i; 0, I_f) = \frac{1}{c^{l/2}} \frac{\Gamma(s_i + s_f + \frac{l}{2} + 1)\Gamma(n_i + s_i - s_f - \frac{l}{2})}{\sqrt{n_i! \Gamma(2s_f + 1)\Gamma(n_i + 2s_i + 1)}\Gamma(s_i - s_f - \frac{l}{2})}. \quad (A.48)$$

This corresponds to a transition from a non-yrast to an yrast state. The integrals for the yrast intraband transitions, Eqs. (50) and (51) in [16], are directly obtained from Eq. (A.48) when $n_i = 0$. Simple explicit forms of the S_l integrals for interband and intraband transitions in the particular cases up to $n = 2$, which are of practical interest, are given below

$$\begin{aligned} & S_l(1, I_i; 1, I_f) \\ = \; & \frac{1}{c^{l/2}}\Big[(2s_i+1)(2s_f+1) - (s_i+s_f-\frac{l}{2})(s_i+s_f+\frac{l}{2}+1)\Big] \\ \times \; & \frac{\Gamma(s_i+s_f+\frac{l}{2}+1)}{\sqrt{\Gamma(2s_i+2)\Gamma(2s_f+2)}}, \end{aligned} \tag{A.49}$$

$$\begin{aligned} & S_l(2, I_i; 1, I_f) \\ = \; & \frac{\sqrt{2}}{2c^{l/2}}\Big\{2(s_i+1)(2s_i+1)(2s_f+1) - (s_i+s_f+\frac{l}{2}+1) \\ \times \; & \Big[2(s_i+1)(2s_i+4s_f+3) - (s_i+s_f+\frac{l}{2}+2)(3s_i+s_f-\frac{l}{2}+2)\Big]\Big\} \\ \times \; & \frac{\Gamma(s_i+s_f+\frac{l}{2}+1)}{\sqrt{\Gamma(2s_i+3)\Gamma(2s_f+2)}}. \end{aligned} \tag{A.50}$$

$$\begin{aligned} & S_l(2, I_i; 2, I_f) \\ = \; & \frac{1}{2c^{l/2}}\Bigg\{4(s_i+1)(2s_i+1)(s_f+1)(2s_f+1) \\ - \; & (s_i+s_f+\frac{l}{2}+1)\Big[16(s_i+1)(s_f+1)(s_i+s_f+1) \\ - \; & (s_i+s_f+\frac{l}{2}+2)\Big\{2(s_i+1)(2s_i+1) + 2(s_f+1)(2s_f+1) + 16(s_i+1)(s_f+1) \\ - \; & (s_i+s_f+\frac{l}{2}+3)(3s_i+3s_f-\frac{l}{2}+4)\Big\}\Big]\Bigg\} \frac{\Gamma(s_i+s_f+\frac{l}{2}+1)}{\sqrt{\Gamma(2s_i+3)\Gamma(2s_f+3)}}. \end{aligned} \tag{A.51}$$

A.4.2. Explicit form of the integrals over ϕ

The integrals over the angular variable ϕ, (3.21), with the relevant parities π_i and π_f can be obtained in the following explicit forms. For $\lambda = 2$ the integral $I_2^{\pm\pm}$ with $k_1 = k_2 = k =$ odd $(++)$ or even $(--)$ is

$$I_2^{\pm\pm}(k) = \frac{2}{\pi}\mathrm{Cat} + \frac{(-1)^{k+1}}{4k}\left[1 + \frac{4}{\pi}\sum_{m=1}^{2k-1}\frac{\sin(m\pi/2)}{m}\right], \tag{A.52}$$

where Cat $= \sum_{n=0}^{\infty} \frac{(-1)^n}{(2n+1)^2} \approx 0.915965594177...$ is the Catalan constant. In the case of $k_1 \neq k_2$, both odd or even, the integral is

$$\begin{aligned} I_2^{\pm\pm}(k_1,k_2) &= \frac{1}{2|k_2-k_1|}\left[1+\frac{4}{\pi}\sum_{m=1}^{|k_2-k_1|-1}\frac{\sin(m\pi/2)}{m}\right] \\ &+ \frac{(-1)^{k_1+1}}{2(k_2+k_1)}\left[1+\frac{4}{\pi}\sum_{m=1}^{k_2+k_1-1}\frac{\sin(m\pi/2)}{m}\right]. \end{aligned} \tag{A.53}$$

For $\lambda = 3$ one has

$$I_3^{+-}(k_1,k_2) = \frac{2k_2}{k_2^2-k_1^2} - \frac{1}{\pi}\left[\frac{(-1)^{(k_2-k_1-1)/2}}{(k_2-k_1)^2} + \frac{(-1)^{(k_2+k_1-1)/2}}{(k_2+k_1)^2}\right], \tag{A.54}$$

where $k_1 = 1,3,5,\ldots\ ,\quad k_2 = 2,4,6,\ldots$ For $\lambda = 1$ the integral is obtained in the form of an infinite, but reasonably converging series

$$\begin{aligned} I_1^{+-} &= \frac{1}{2\pi}\sum_{m=\pm1}^{\pm\infty}\sum_{n=\pm1}^{\pm\infty}\sum_{\nu=\pm1}\frac{\mathrm{sign}(-n)}{|mn|} \\ &\times \left[(1-\delta_{k_2+\nu k_1,-m-n})\frac{\sin[(k_2+\nu k_1+m+n)\frac{\pi}{2}]}{(k_2+\nu k_1+m+n)} + \frac{\pi}{2}\delta_{k_2+\nu k_1,-m-n}\right], \end{aligned} \tag{A.55}$$

where $k_1 = 1,3,5,\ldots\ ,\quad k_2 = 2,4,6,\ldots$

A.5. Matrix elements of $\hat{j}_+$ in the ADHO basis

An analytic expression for the matrix elements of $\hat{j}_+ = \hat{l}_+ + \hat{s}_+$ ($\hat{l}_+$ and $\hat{s}_+$ are the s.p. orbital momentum and spin operators, respectively) can be derived by using the boson representation of the ADHO basis functions [82] and the "stretched" form of the operator $\hat{l}_+$ in cylindric coordinates [83]. The ADHO basis states are given as [82]

$$|n_z n_\perp \Lambda\Sigma\rangle = (-1)^{(n_\perp-\Lambda)/2}\frac{(a_z^+)^{n_z}}{\sqrt{n_z!}}\frac{(b_1^+)^{(n_\perp+\Lambda)/2}}{\sqrt{[(n_\perp+\Lambda)/2]!}}\frac{(b_2^+)^{(n_\perp-\Lambda)/2}}{\sqrt{[(n_\perp-\Lambda)/2]!}}|000\rangle|\Sigma\rangle, \tag{A.56}$$

with $n_\perp + n_z = N$ (N is the major oscillator quantum number) and $\Lambda + \Sigma = \Omega$. Here the operators

$$\begin{aligned} a_\xi^+ &= \frac{1}{\sqrt{2}}\left(c_\xi\xi - \frac{1}{c_\xi}\partial\xi\right) \\ a_\xi &= \frac{1}{\sqrt{2}}\left(c_\xi\xi + \frac{1}{c_\xi}\partial\xi\right) \qquad \xi = x,y,z\ , \end{aligned} \tag{A.57}$$

with $c_\xi = \sqrt{m\omega_\xi/\hbar}$ are the standard boson operators for the harmonic oscillator quanta in the Cartesian coordinates x, y, z. The operators

$$\begin{aligned} b_1^+ &= \frac{1}{\sqrt{2}}\left(a_x^+ + ia_y^+\right) \\ b_2^+ &= \frac{1}{\sqrt{2}}\left(a_x^+ - ia_y^+\right) \end{aligned} \tag{A.58}$$

are the result of a canonical transformation providing the operators

$$\begin{aligned} N_\perp &= b_1^+ b_1 + b_2^+ b_2 \\ L_z/\hbar &= b_1^+ b_1 - b_2^+ b_2, \end{aligned} \tag{A.59}$$

whose eigenvalues are $n_\perp$ and Λ, respectively, while the quantum number n_z is the eigenvalue of the operator $a_z^+ a_z$.

After reversing the relations (A.57) and (A.58) one obtains

$$\begin{array}{rclrcl} x &=& \frac{1}{2c_\perp}(b_1^+ + b_2^+ + b_1 + b_2) & \partial_x &=& \frac{c_\perp}{2}(-b_1^+ - b_2^+ + b_1 + b_2) \\ y &=& \frac{i}{2c_\perp}(-b_1^+ + b_2^+ + b_1 - b_2) & \partial_y &=& \frac{ic_\perp}{2}(b_1^+ - b_2^+ + b_1 - b_2) \\ z &=& \frac{1}{\sqrt{2}c_z}(a_z^+ + a_z) & \partial_z &=& \frac{c_z}{\sqrt{2}c_z}(-a_z^+ + a_z), \end{array} \tag{A.60}$$

where $c_\perp = \sqrt{m\omega_\perp/\hbar}$ with $\omega_\perp = \omega_x = \omega_y$. By using the above relations in the standard definitions of the angular momentum operators

$$\hat{l}_{\xi_i} = -i\hbar\left(\xi_j\partial_{\xi_k} - \xi_k\partial_{\xi_j}\right), \qquad \xi_{i,j,k} = x, y, z \text{ cyclic}, \tag{A.61}$$

and

$$\hat{l}_\pm = \hat{l}_x \pm i\hat{l}_y, \tag{A.62}$$

one obtains the raising operator of the single-particle orbital momentum $\hat{l}_+$ in terms of the operators a_z^+, a_z and b_1^+, b_2 [83]

$$\begin{aligned} \hat{l}_+ &= \frac{\hbar}{\sqrt{2}}\left[a_z^+ b_1^+(-q^{1/2} + q^{-1/2}) + a_z^+ b_2(q^{1/2} + q^{-1/2})\right. \\ &+ \left. a_z b_1^+(-q^{1/2} - q^{-1/2}) + a_z b_2(q^{1/2} - q^{-1/2})\right], \end{aligned} \tag{A.63}$$

with $q = \omega_\perp/\omega_z = \beta_\perp^2/\beta_z^2$ ($\beta_\perp = (m\omega_\perp/\hbar)^{1/2}$, $\beta_z = (m\omega_z/\hbar)^{1/2}$ [84]).

The matrix element of the operator $\hat{l}_+$, Eq. (A.63), between basis states (A.56) is obtained by using the action of the operators a_z^+, a_z and b_1^+, b_2 on the respective parts of the basis vector (A.56). The raising operators a_z^+ and b_1^+ increase the power factors of the terms $(a_z^+)^{n_z}$ and $(b_1^+)^{(n_\perp+\Lambda)/2}$ by 1, and after rearranging respectively the denominators one obtains the shifted vector parts $|n_z + 1\rangle$ and $|n_\perp + 1\rangle$. The lowering operators a_z and b_2 act after the use of the relation $b(b^+)^n = n(b^+)^{n-1} + (b^+)^n b$ (with the second term

giving zero) and lower the powers of the corresponding terms in the vector (A.56). As a result the quantum numbers n_z and $n_\perp$ are shifted by -1. Thus one has

$$\begin{aligned}
&\langle n_z' n_\perp' \Lambda' \Sigma' | \hat{l}_+ | n_z n_\perp \Lambda \Sigma \rangle = -\frac{\hbar}{2} \delta_{\Lambda' \Lambda+1} \delta_{\Sigma' \Sigma} \\
\times\ & \Big[(q^{1/2} - q^{-1/2}) \left(\sqrt{(n_z+1)(n_\perp + \Lambda + 2)}\, \delta_{n_\perp' \, n_\perp + 1} \delta_{n_z' \, n_z + 1} \right. \\
+\ & \left. \sqrt{n_z (n_\perp - \Lambda)}\, \delta_{n_\perp' \, n_\perp - 1} \delta_{n_z' \, n_z - 1} \right) \\
+\ & (q^{1/2} + q^{-1/2}) \left(\sqrt{(n_z+1)(n_\perp - \Lambda)}\, \delta_{n_\perp' \, n_\perp - 1} \delta_{n_z' \, n_z + 1} \right. \\
+\ & \left. \sqrt{n_z (n_\perp + \Lambda + 2)}\, \delta_{n_\perp' \, n_\perp + 1} \delta_{n_z' \, n_z - 1} \right) \Big] .
\end{aligned} \tag{A.64}$$

By using the relation $N = n_\perp + n_z$, one can write the matrix element $\hat{l}_+$ between basis states $|N n_z \Lambda \Sigma\rangle$

$$\begin{aligned}
&\langle N' n_z' \Lambda' \Sigma' | \hat{l}_+ | N n_z \Lambda \Sigma \rangle = -\frac{\hbar}{2} \delta_{\Lambda' \Lambda+1} \delta_{\Sigma' \Sigma} \\
\times\ & \Big[(q^{1/2} - q^{-1/2}) \left(\sqrt{(n_z+1)(N - n_z + \Lambda + 2)}\, \delta_{N' \, N+2} \delta_{n_z' \, n_z + 1} \right. \\
+\ & \left. \sqrt{n_z (N - n_z - \Lambda)}\, \delta_{N' \, N-2} \delta_{n_z' \, n_z - 1} \right) \\
+\ & (q^{1/2} + q^{-1/2}) \delta_{N' \, N} \left(\sqrt{(n_z+1)(N - n_z - \Lambda)}\, \delta_{n_z' \, n_z + 1} \right. \\
+\ & \left. \sqrt{n_z (N - n_z + \Lambda + 2)}\, \delta_{n_z' \, n_z - 1} \right) \Big] .
\end{aligned} \tag{A.65}$$

The spin operator $\hat{s}_+$ is given by

$$\hat{s}_+ | n_z n_\perp \Lambda \Sigma \rangle = \sqrt{\frac{3}{4} - \Sigma(\Sigma+1)}\, | n_z n_\perp \Lambda \Sigma + 1 \rangle, \quad \Sigma = \pm \frac{1}{2}, \tag{A.66}$$

and its matrix element is

$$\langle n_z' n_\perp' \Lambda' \Sigma' | \hat{s}_+ | n_z n_\perp \Lambda \Sigma \rangle = \delta_{n_z' \, n_z} \delta_{n_\perp' \, n_\perp} \delta_{\Lambda' \, \Lambda} \delta_{\Sigma' \, \frac{1}{2}} \delta_{\Sigma \, -\frac{1}{2}} . \tag{A.67}$$

For the basis states $|N n_z \Lambda \Sigma\rangle$ the expressions (A.66) and (A.67) are the same with only $n_\perp$ being replaced by N. When the basis is denoted by $|N n_z \Lambda \Omega\rangle$ the factors $\delta_{\Sigma' \Sigma}$ and $\delta_{\Sigma' \, \frac{1}{2}} \delta_{\Sigma \, -\frac{1}{2}}$ in (A.65) and (A.67) are replaced by $\delta_{\Omega' \Omega + 1}$. The above matrix elements were originally tabulated as selection rules for the ADHO basis quantum numbers in Ref. [85], while here they are given in a closed form. The expression (A.65) is given in [86] without derivation.

Bibliography

[1] G. Musiol, J. Ranft, R. Reif and D. Seeliger, *Kern- und Elementarteilchenphysik*, Verlag Harri Deutsch, Frankfurt am Main, 1995

[2] M.G. Mayer, Phys. Rev. **75** (1949) 1969; **78** (1950) 16

[3] O. Haxel, J.H.D. Jensen and H.E. Suess, Phys. Rev. **75** (1949) 1769

[4] A. Bohr, Kgl. Danske Videnskab Selskab Mat. Fys. Medd. **26** No. 14 (1953)

[5] A. Bohr and B. Mottelson, Kgl. Danske Videnskab Selskab Mat. Fys. Medd. **27** (16) (1953)

[6] A. Bohr, *Rotational States in Atomic Nuclei* (Thesis, Copenhagen 1954)

[7] A. Faessler and W. Greiner, Z. Physik **168** (1962) 425

[8] A. Faessler and W. Greiner, Z. Physik **170** (1962) 105

[9] A. Faessler and W. Greiner, Z. Physik **177** (1964) 190

[10] A. Faessler and W. Greiner, Nucl. Phys. **59** (1964) 177

[11] A. Faessler , W. Greiner and R.K. Sheline, Nucl. Phys. **62** (1965) 241

[12] A. Faessler , W. Greiner and R.K. Sheline, Nucl. Phys. **70** (1965) 33

[13] A. Faessler , W. Greiner and R.K. Sheline, Nucl. Phys. **80** (1965) 417

[14] A.M. Lane, *Nuclear Theory*, W.A. Benjamin, New York, 1964

[15] P. Ring and P. Schuck, *The Nuclear Many-Body Problem*, Springer, Heidelberg, 1980

[16] N. Minkov, P. Yotov, S. Drenska, W. Scheid, D. Bonatsos, D. Lenin and D. Petrellis, Phys. Rev. C **73**, 044315 (2006)

[17] N. Minkov, S. Drenska, M. Strecker, W. Scheid and H. Lenske, Phys. Rev. C **85**, 034306 (2012)

[18] P.G. Bizzeti and A.M. Bizzeti-Sona, arXiv:nucl-th/0409031v2 19 oct 2004

[19] P.G. Bizzeti and A.M. Bizzeti-Sona, Description of nuclear octupole and quadrupole deformation close to the axial symmetry: Octupole vibrations in the X(5) nuclei ^{150}Nd and ^{152}Sm

[20] S. Frauendorf, Phys. Rev. C **77**, 021304(R) (2008)

[21] N. Minkov, M. Strecker and W. Scheid, Transactions of the Bulgarian Nuclear Society **13**, 121 (2009)

[22] N. Minkov, S. Drenska, M. Strecker and W. Scheid, J. Phys. G: Nucl. Part. Phys. **36**, 025108 (2009)

[23] N. Minkov, S. Drenska, M. Strecker and W. Scheid, J. Phys.: Conf. Series **205**, p. 012009 (2010)

[24] N. Minkov, S. Drenska, M. Strecker and W. Scheid, J. Phys. G: Nucl. Part. Phys. **37**, 025103 (14pp) (2010)

[25] N. Minkov, S. Drenska, M. Strecker and W. Scheid, Int. J. Mod. Phys. E **20**, 228-234 (2011)

[26] S. Cwiok, J. Dudek, W. Nazarewicz, J. Skalski and T. Werner, Comput. Phys. Commun. **46** (1987) 379-399

[27] K. Yoshida, Pair correlation and continuum coupling effects on low-frequency modes of excitation in deformed neutron-rich nuclei, thesis, 2007

[28] A. Bohr and B.R. Mottelson, *Nuclear Structure*, vol. II (New York: Benjamin, 1975)

[29] W. Greiner, J.M. Eisenberg, *Nuclear Models*, Volume I, North-Holland Publishing Company, Amsterdam, 1970

[30] http://www.wasserklangbilder.de/

[31] E. Chladni, *Entdeckungen über die Theorie des Klanges*, Leipzig, 1787

[32] F. Tuncer, thesis, Middle East Technical University (http://etd.lib.metu.edu.tr/upload/12609917/index.pdf)

[33] W. Pauli, *Handbuch der Physik*, Vol. XXIV, Springer-Verlag, Berlin, 1933

[34] M. Strecker, diploma thesis, University Giessen

[35] M.A. Preston, *Physics of the Nucleus*, Addison-Wesley Publishing Company inc.,

USA, 1963

[36] S.G. Nilsson and I. Ragnarsson, *Shapes and Shells in Nuclear Structure*, Cambridge University Press, 1995

[37] W. Greiner and J. Maruhn, *Kernmodelle*, Verlag Harri Deutsch, Frankfurt a.M., 1995

[38] J.P. Davidson, *Collective Models of the Nucleus*, Academic Press, New York, 1968

[39] D. Griffiths, *Einführung in die Elementarteilchenphysik*, Akademie Verlag, Berlin 1996

[40] D.L. Hill and J.A. Wheeler, Phys. Rev. **89** (1953) 1102

[41] N. Tsoneva, private communication

[42] S. Raman, C. W. Nestor, Jr., and P. Tikkanen, At. Data Nucl. Data Tables **78**, 1-128 (2001)

[43] T. Kibedi and R. H. Spear, At. Data Nucl. Data Tables **80**, 35-82 (2002)

[44] A. Ataie, diploma thesis, University Giessen

[45] D.J. Rowe, Rev. Mod. Phys. **40** (1968) 153

[46] F. Schwabl, *Quantenmechanik*, Springer-Verlag, Berlin Heidelberg, 2002

[47] D.A. Varshalovich, A.N. Moskalev and V.K. Khersonskii, *Quantum Theory of Angular Momentum*, World Scientific, Singapore, 1988

[48] T. Mayer-Kuckuk, *Kernphysik*, Teubner Verlag, Stuttgart/Leipzig/Wiesbaden, 2002

[49] J.M. Eisenberg and W. Greiner, *Nuclear Models*, North-Holland Physics Publishing, New York, 1987

[50] D.J. Rowe, *Nuclear Collective Motion*, World Scientific Publishing, 2010

[51] M. Minuth and T. Fernández Caramés: Lattice theory and Metropolis simulation, http://www-zeuthen.desy.de/students/2003/doc/minuth+theresa-report.pdf

[52] N. Metropolis, A. Rosenbluth, M. Rosenbluth, A. Teller and E. Teller, Journal of Chemical Physics **21** (1953) 1087-1092

[53] C. Morningstar: The Monte Carlo Method in Quantum Mechanics, http://www.andrew.cmu.edu/user/cmorning/QM_- MonteCarlo.pdf

[54] P.A. Butler and W. Nazarewicz, Rev. Mod. Phys. **68**, 349 (1996)

[55] H.J. Krappe and U. Wille, Nucl. Phys. A **124**, 641 (1969)

[56] G.A. Leander and R.K. Sheline, Nucl. Phys. A **413**, 357 (1984)

[57] G.A. Leander, Y.S. Chen, Phys. Rev. C **35**, 1145 (1987)

[58] N. Minkov, S. Drenska, P. Yotov, S. Lalkovski, D. Bonatsos and W. Scheid, Phys. Rev. C **76**, 034324 (2007)

[59] A.A. Raduta, C.M. Raduta and Amand Faessler, Phys. Rev. C **80**, 044327 (2009)

[60] N. Minkov, S. Drenska, M. Strecker and W. Scheid, Int. J. Mod. Phys. E **21**, 1250021 (2012)

[61] G.A. Leander, Y.S. Chen, Phys. Rev. C **37**, 2744 (1988)

[62] W.D. Myers and W.J. Swiatecki, Ann. of Phys. **84**, 186 (1974)

[63] W.D. Myers: Droplet model of atomic nuclei (IFI/Plenum Data, New York, 1977)

[64] C.O. Dorso, W.D. Myers and W.J. Swiatecki, Nucl. Phys. A **451**, 189 (1986)

[65] V.Yu. Denisov and A.Ya. Dzyublik, Nucl. Phys. A **589**, 17 (1995)

[66] P.A. Butler and W. Nazarewicz, Nucl. Phys. A **533**, 249 (1991)

[67] J. Damgaard, H.C. Pauli, V.V. Pashkevich and V.M. Strutinsky, Nucl. Phys. A **135**, 432-444 (1969)

[68] J. Dobaczewski and J. Dudek, Computer Physics Communications, Volume **102**, Issues 1-3, 2 May 1997, Pages 166-182

[69] V. Martin and L.M. Robledo, Comput. Phys. Commun. **99** (1996) 113-127.

[70] U. Götz, H.C. Pauli and K. Alder, Nucl. Phys. A **175** (1975) 481-494

[71] N. Ullah and D.J. Rowe, Nucl. Phys. A **163** (1971) 257-264

[72] http://www.nndc.bnl.gov/ensdf/

[73] J.P. Elliott, J.A. Evans and P. Park, Phys. Lett. B **169**, 309 (1986)

[74] D.J. Rowe and C. Bahri, J. Phys. A **31**, 4947 (1998)

[75] A. P. Prudnikov, Yu. A. Brichkov and O. I. Marichev, *Integrals and Series of Special*

Functions (Nauka, Moskow, 1985) (in Russian)

[76] http://functions.wolfram.com/Polynomials/LaguerreL3/21/ShowAll.html

[77] L. J. Slater, *Generalized Hypergeometric Functions* (Cambridge University Press, Cambridge, 1987); http://mathworld.wolfram.com/GeneralizedHypergeometric-Function.html

[78] W. F. Perger, A. Bhalla and M. Nardin, Comp. Phys. Comm. **77**, 249 (1993)

[79] http://www.nndc.bnl.gov/nudat2/indx_adopted.jsp. Data as of August 2011

[80] Reference Input Parameter Library, www-nds.iaea.org/ripl2/

[81] M. Strecker, N. Minkov and H. Lenske, Nuclear Theory, vol. 30, Proceedings of the 30-th International Workshop on Nuclear Theory (Rila, Bulgaria 2011), ed. A. I. Georgieva and N. Minkov, (Heron Press, Sofia), p. 53 (2011)

[82] P. Quentin and R. Babinet, Nucl. Phys. A **156**, 365 (1970)

[83] P. Quentin, PhD Thesis, Universite de Paris-Sud, Centre d'Orsay (1975)

[84] D. Vautherin, Phys. Rev. C **7**, 296 (1973)

[85] J. P. Boisson and R. Piepenbring, Nucl. Phys. A **168**, 385 (1971)

[86] L. Bonneau, "Eléments de matrice de $\hat{j}_+$ dans la base asymptotique", Preprint, CENBG/Univ. Bordeaux I (2008)